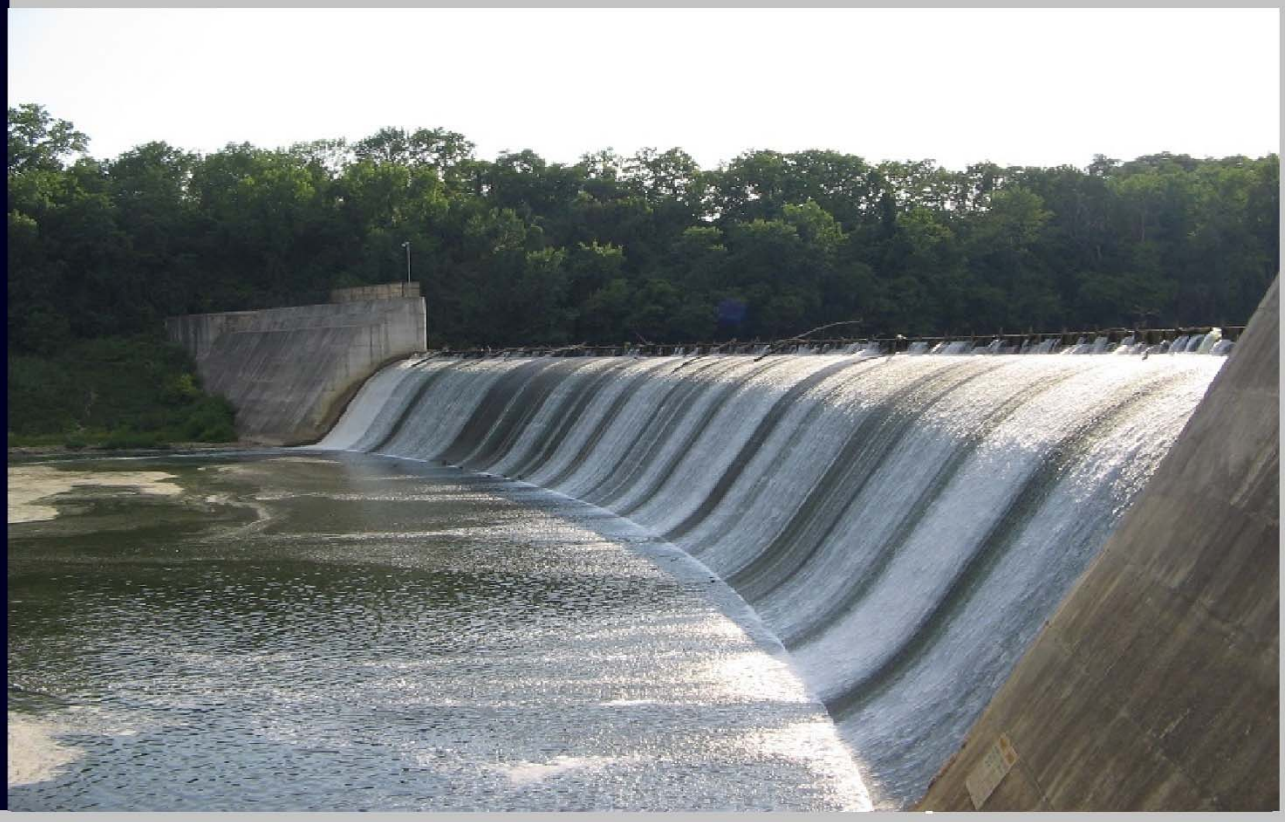
Shahid Chamran University of Ahvaz

Journal of Hydraulic Structures

Scientific Professional Journal

Summer 2017
Volume 3, No 1



نشریه علمی پژوهشی

انجمن هیدرولیک ایران
Iranian Hydraulic Association

In the name of GOD

Journal of Hydraulic Structures
Department of Civil Engineering
Faculty of Engineering
Shahid Chamran University of Ahvaz

JORNAL OF
HYDRAULIC STRUCTURES
SHAHID CHAMRAN UNIVERSITY OF AHVAZ

Manager: *Prof. Hamid R. Ghafouri*
Editor-in-chief: *Dr. Ali Haghighi*
Editorial coordinator: *Dr. Seyed Mohammad Ashrafi*
Department of Civil Engineering, Engineering Faculty, Shahid Chamran University of Ahvaz, Ahvaz, Iran.

Members
Prof. Hossein M. V.Samani
Civil Engineering Department, Shahid Chamran University of Ahvaz, Ahvaz, Iran
Prof. Hamid R. Ghafouri
Civil Engineering Department, Shahid Chamran University of Ahvaz, Ahvaz, Iran
Dr. Ali Haghighi
Civil Engineering Department, Shahid Chamran University of Ahvaz, Ahvaz, Iran
Prof. Mahmood S. Bajestan
Hydraulic Structures Department, Shahid Chamran University of Ahvaz, Ahvaz, Iran
Prof. Saeed R. S. Yazdi
Civil Engineering Department, K.N.Toosi University of Technology, Tehran, Iran
Dr. Mohammad S. Pakbaz
Civil Engineering Department, Shahid Chamran University of Ahvaz, Ahvaz, Iran
Dr. Arash Adib
Civil Engeering Department, Shahid Chamran University of Ahvaz, Ahvaz, Iran
Dr. Mojtaba Labibzadeh
Civil Engineering Department, Shahid Chamran University of Ahvaz, Ahvaz, Iran
Prof. Helena M. Ramos
Instituto Superior Técnico (IST), University of Lisbon
Dr. S. Mohammad Ashrafi
Civil Engineering Department, Shahid Chamran University of Ahvaz, Ahvaz, Iran
Dr. S. Abbas Haghshenas
Institute of Geophysics, University of Tehran | UT, Tehran, Iran
Dr. Mohammad Zounemat-Kermani
Department of Water Engineering, Shahid Bahonar University of Kerman, Kerman, Iran
Dr. Taher Rajaee
Civil Engineering Department, University of Qom, Qom, Iran
Dr. Mohammad Vaghefi
Civil Engineering Department, Faculty of Engineering, Persian Gulf University, Bushehr, Iran
Dr. A. A. Telvari
Soil Conservation and Watershed Management Research Institute; Department of Civil Engineering, Islamic Azad University, Ahvaz branch, Ahvaz, Iran

Shahid Chamran Univeristy of Ahvaz

انجمن هیدرولیک ایران

CONTENTS

VOL 3, NO I, Summer 2017

II ***Aims and Scope***

01 An Overview of Fabrication Methods and Applications of Carbon Nanotube Membrane in Environmental Engineering as Hydraulic Microstructures
A. Abedin Maghanaki

14 Estimation of Fracture path in the Structures and the Influences of Non-singular term on crack propagation
A.G. Khademalrasoul; R. Maghsoudi

35 Developing Self-adaptive Melody Search Algorithm for Optimal Operation of Multi-reservoir Systems
S. M. Ashrafi; S. F. Ashrafi; S. Moazami

49 Multiobjective design of sewer networks
A. Ebrahim Bakhshipour; Y. Makaremi; Ulrich Dittmer

57 Proposing a Discharge Coefficient Equation for Triangular Labyrinth Spillways Based on Laboratory Studies
M. Heydari; A. Mohammadiha; S. Abolfathi

71 The Optimization of Energy Supply Systems by Sequential Streamflow Routing Method and Invasive Weed Optimization Algorithm; Case Study: Karun II Hydroelectric Power Plant
H. Goharnejad; M. Mohamadi Naser; M. Zakeri Niri

Aims and Scope

Hydraulic Structure Journal is an interdisciplinary journal which publishes high-quality peer-reviewed articles addressing the latest developments and applied methods **in construction, maintenance, management, and operation policy of Hydraulic Structures.**
The Journal aims at providing an efficient route to fast-track publication, **within 10-12 weeks after manuscript submission**. Manuscripts will be considered for publication in the following categories: **research articles**, **technical notes**, **case reports** and **discussions**.

The general areas covered by the Journal include:

- Technical and methodological advances in application, design/selection, production, modification of construction materials
- Advances in numerical and analytical methods
- Hydro informatics and soft computing
- Hydraulic aspects of hydraulic structures
- Applied surface and subsurface hydrology and hydrometeorology
- Forecasting approaches in water resources engineering
- Economic and social aspects of hydraulic structures
- Uncertainty analysis and risk management in hydraulics and water resources engineering
- Application of Nanotechnology in Hydraulic Structures
- Geotechnics of Hydraulic Structures
- Damage detection techniques

The following might be considered as hydraulic structures:

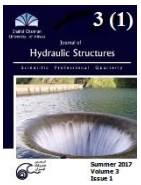
- Dams and associated structures
- River and Watershed Structures
- Offshore and Onshore Structures
- Irrigation and Drainage Channel Networks
- Bridges
- Water Storage and Conveyance Structures
- Pipelines and Pump Stations
- Sewerage Systems
- Water and Wastewater Treatment Plants
- Historical Water Structures

General Information

Title: Journal of Hydraulic Structures
Subject: Hydraulics and water resources engineering
Coverage area: International
Journal Type: Scientific and technical
License Holder: Shahid Chamran University
Editor-in-Chief: Dr. Ali Haghighi
Manager: Prof. Hamid R. Ghafouri
Editorial coordinator: Dr. Seyed Mohammad Ashrafi

Language Editors:
Majid SadollahKhani
Soroosh Kamali
Address: Engineering Faculty, Shahid Chamran University of Ahvaz
Phone #: +986113330010-20 (5610 & 5603)
Fax #: +986113337010
Language: English
Email: jhs@scu.ac.ir
Website: jhs.scu.ac.ir

Journal of Hydraulic Structures
***J. Hydraul. Struct.*, 2017; 3(1):1-13**
DOI: 10.22055/jhs.2017.13280



An Overview of Fabrication Methods and Applications of Carbon Nanotube Membrane in Environmental Engineering as Hydraulic Microstructures

Amir Abedin Maghanaki[1]

Abstract

The main purpose of this article is to study fabrication methods and applications of aligned carbon nanotube (CNT) membranes as a hydraulic microstructure in treatment processes. This paper emphasizes the use of CNTs as membrane in separation processes like water and wastewater treatment because of their exclusive advantages. Their most important characteristics are high mechanical strength against pressure, thermal stability and fast fluid transport with a very low pressure gradient inside CNTs. It is predictable to expand using CNT membranes in separation processes and environmental engineering because of their suitable mechanical properties.

Keywords: Membrane, Carbon Nanotubes, Treatment Processes, Environmental Engineering, Hydraulic Microstructures

Received: 03 March 2017; Accept: 14 June 2017

1. Introduction

Membrane technology is used for the separation of various compounds by thin film layer with controlled pore size. The discovery of membranes properties goes back many years. The Osmosis phenomenon was recognized for the first time, by Nollet in 1748 and first synthetic membrane -apparently from Nitrocellulose- Constructed and completed by Fick in 1855 [1-3]. Simultaneously with the discovery of cellulosic membranes, the natural membranes were used in the filtration experiments. In the last decades of the 19th century researchers who studied on the diffusion phenomenon, using from the membranes of animals (bladder of pig and fish, skin of frog and bovine's heart) and plant origin (onion) for dialysis experiments and studies of ultrafiltration [4-8].

Inorganic membranes were developed before 1945. The earlier application of porous inorganic membranes was used for the separation of uranium isotopes; therefore, they were

[1] Department of Civil Engineering, Faculty of Engineering, Islamic Azad University, Roudehen Branch, Tehran, Iran, Phone: +98.912.305.8178, amir.abedin@gmail.com (**Corresponding author**)

mainly used for military purposes or nuclear applications [9, 10]. Non-nuclear applications of inorganic membranes started at the beginning of 1980 [10, 11]. The potential of inorganic membranes was not widely recognized until high quality porous ceramic membranes were produced for industrial usage on a large scale [10, 12]. Nowadays these membranes are widely used in water treatment, dairy industries and gas separation [13-15].

After the discovery of carbon nanotubes (CNTs) in 1991 by Iijima [16], great attraction and scientific interest subsequently followed due to their special physical properties [17-20]. There are different methods for the synthesis of CNTs, such as: laser-ablation, arc discharge and chemical vapor deposition (CVD) [10, 21-23]. CVD is preferred over other methods, because it produces higher quality CNTs [24, 25]. Currently the most useful method is CVD and its changed techniques (such as floating catalyst CVD (FCCVD), plasma enhanced CVD (PECVD), water-assisted CVD) [26-30]. This method is based on the thermal decomposition of carbon sources (carbon feedstock) in the presence of catalyst on a suitable substrate. The ultimate goal of CNT research is driven by the ability to design functional macroscopic structures that can fully integrate the single nanotube properties [31].

2. Membrane Fabrication from CNTs

There are two methods for the preparation membrane from CNTs.

In the first method; CNTs are deposited regularly together -without adhesive materials- on ceramic or metal or any suitable substrate and called self-assembly membranes. In another method, the space between the nanotubes is filled by regularly arranged polymeric materials, as a cohesive.

For the first time, Ajayan et al. (1994) were used the "Aligned Carbon Nanotube" phrase in their article [32]. They formed the aligned carbon nanotube array by cutting a polymer resin-nanotube composite. This composite had been built as strong material and had not applied as membrane. This work represents an important step, but the rather low tube density, incomplete alignment, and the presence of the resin matrix importantly affect the properties as compared with a pure, aligned material [33].

After them, de Heer et al. (1995) reported the production of macroscopic aligned multiwalled carbon nanotube (MWCNT) films, using the arc evaporation process [33]. They studied its optical and electronic properties and diagnosed them unsuitable for flow-through applications.

Until 1999 there was no imagination for growth mechanism of carbon nanotubes; Sinnott et al. (1999) presented several theories for growth mechanism of carbon nanotubes [35]. One theory was based on the assumption that the metal catalyst particles are floating or fixed on the graphite or other substrate. It is likely that the form of catalyst particles will appear spherical or pear-shaped and deposition will only occur on half of the surface (due to the fact that the pear-shaped particles are done in lower curvature).

One theory postulates that metal catalyst particles are floating or are supported on graphite or another substrate. It presumes that the catalyst particles are spherical or pear-shaped, in which case the deposition will take place on only one half of the surface (this is the lower curvature side for the pear shaped particles). The carbon diffuses along the concentration gradient and precipitates on the opposite half, around and below the bisecting diameter. However, it does not precipitate from the apex of the hemisphere, which accounts for the hollow core that is characteristic of these filaments. For supported metals, filaments can form either by "extrusion" or "root-growth" in which the nanotube grows upwards from the metal particles that remain attached to the substrate, or the particles detach and move at the head of the growing nanotube, labeled "tip-growth". These mechanisms are illustrated graphically in Fig. 1 [35-37].

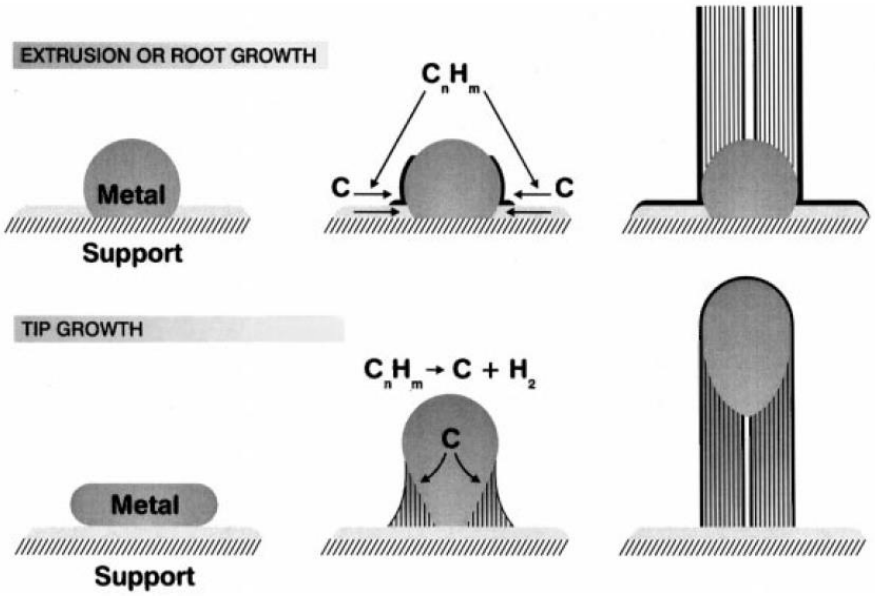


Figure 1. Schematics of root-growth and tip-growth mechanisms for carbon filament growth (Sinnott et al., 1999).

Chengwei et al. (2000) at Lanzhou University of China prepared a well-aligned CNT array membrane on a porous alumina template by CVD [34]. They fed acetylene (as a carbon source) in the presence of an iron catalyst with hydrogen used at temperature 700°C. They stated that the growth property of CNTs was closely related to the structure of the template, particle size of catalyst, process temperature, flow ratio and deposition time.

Then, Casavant and colleagues reported that they have produced the first macroscopic membranes of magnetically aligned single-wall carbon nanotubes (SWNT) in a magnetic field in 2001 and 2003 [38-39]. These membranes were prepared by producing a suspension of SWNT segments, introducing the suspension membrane of SWNT. They exhibited natural cleavage planes parallel to the magnetic field. However, the microstructure specification of the membrane was not presented to determine that the passing flow takes place within the CNTs or from the space between them.

Shimoda et al. (2000) reported that they have produced the self-assembly carbon nanotube membrane in macroscopic scale [40]. They synthesized SWNTs by laser ablation method. The SWNT bundle and individual nanotube diameters were reported in the range of 10–50 and 1.3–1.5 nm, respectively. SWNTs purified by reflux and filtration were chemically etched to short bundles by ultrasonic-assisted oxidation. After removing the acid by filtration, the processed SWNTs were dispersed in de-ionized water. Thin film appeared on the surface of a soaked glass substrate in the SWNTs/water dispersion with natural vaporization of water. The fabricated membrane had a smooth surface and Transmission electron microscopy (TEM) measurements showed that the SWNT bundles were uniaxially aligned. Since the physical properties of the membrane (such as mechanical specification, thermal stability and flow rate) were not offered, we cannot comment on it properly.

Then, Hinds et al. (2003) succeeded in producing a multi-wall carbon nanotubes (MWNT) membrane [41]. An array of aligned carbon nanotubes was incorporated across a polymer film to

form a well-ordered nanoporous membrane structure (Figure 2). Although the outer diameter of MWNTs had significant variation (20-40 nm), the hollow inner core diameter was well controlled at 2-6.6 nm. This inner core diameter is in the size range of many proteins and other important biological macromolecules. They announced that the idealized membrane structure would occur if the space between the CNTs was filled with a continuous polymer film, and the normally closed ends of CNTs were etched open. To accomplish this, the as-deposited CNTs were grown for 30 min (aligned CNT film thickness of 5–10 μm) on quartz substrate in a chemical vapor deposition process using a ferrocene/xylene/Ar/H_2 feed at 700°C. At a high temperature, ferrocene decomposes to iron particles which then act as a catalyst for the nanotube growth while the xylene acts as carbon feedstock [42]. Moreover, they used a 50wt% solution of polystyrene (PS) and toluene to spin coating over the surface. Then, the film was dried in vacuum at 70°C for four days. Hydrofluoric acid was then used to remove the CNT/PS composite from the quartz substrate to produce a free-standing composite film of 5–10 μm thickness. H_2O plasma-enhanced oxidation process was used to remove a thin layer of excess polymer from the top surface and open the CNT tips to form a membrane structure. Scanning electron microscopy (SEM) analysis of this surface has given an estimated areal density of 6 (±3) × 10^{10} CNT-tips/cm^2. TEM of dissolved membranes demonstrated that about 70% of the CNT tips had been opened by the plasma oxidation process under our conditions. The mean pore diameter of 7.5 (±2.5) nm has been calculated using the observed estimate of CNT areal density.

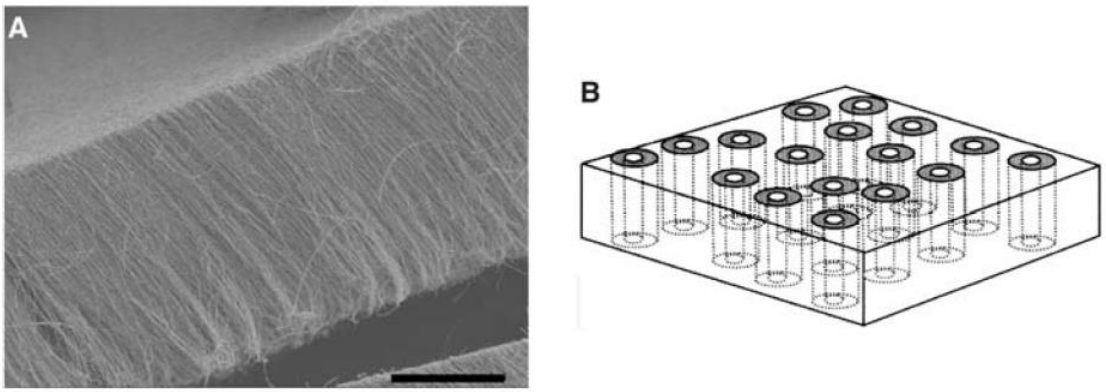


Figure 2. (A) As grown dense multiwalled CNT array from Fe-catalyzed chemical vapor deposition process (Scale bar 50 μm). (B) Schematic of target membrane structure, with a polymer impregnation between CNTs (Hinds et al., 2003).

Srivastava et al. (2004) developed the production of filters using carbon nanotubes [43]. They used continues spray pyrolysis method for growing aligned MWNTs on a quartz tube using ferrocene/benzene solution at 900°C (Figure 3).

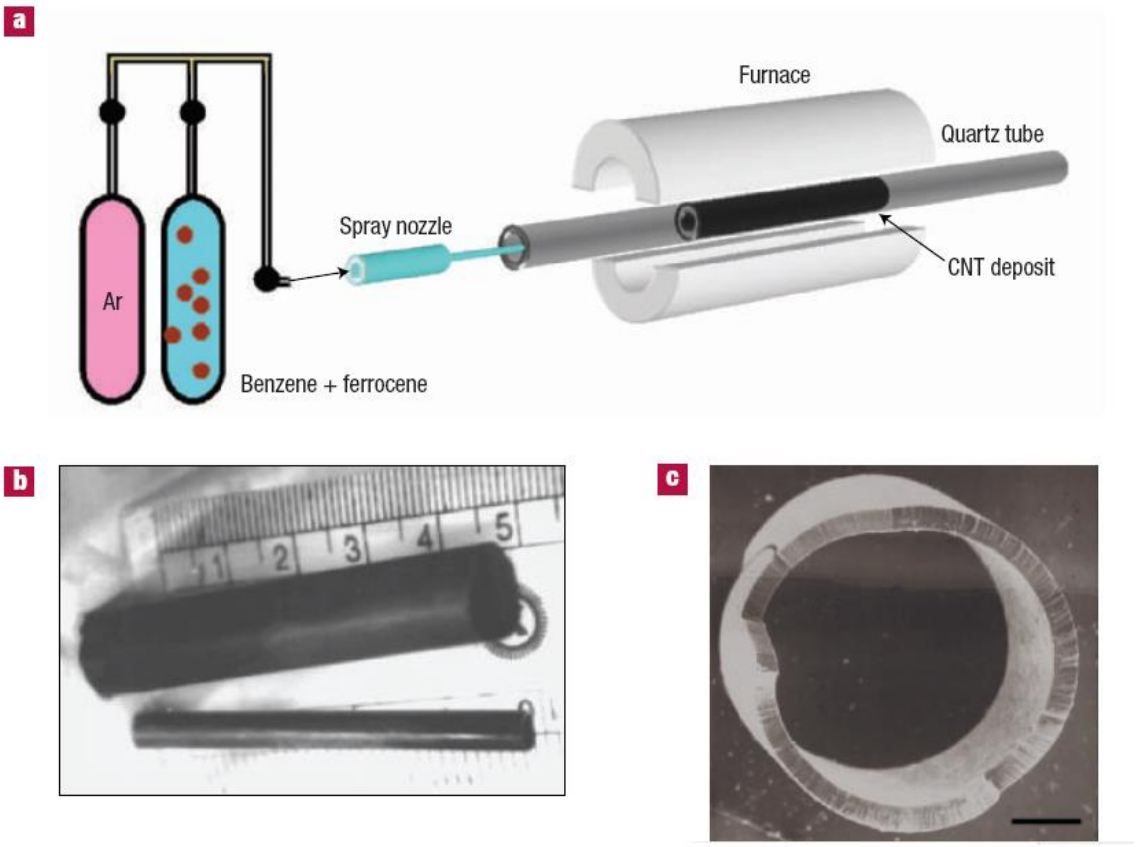


Figure 3 – Production of the macro architecture of aligned nanotubes for use in filtration applications. (a) Schematic of the spray pyrolysis set for growing aligned MWNTs. (b) Photograph of the bulk tube. (c) SEM image of the aligned tubes with radial symmetry resulting in hollow cylindrical structure (scale bar 1 mm) (Srivastava et al., 2004).

This method can be used for fabricating such nanofilters comprising an array of carbon nanotubes (CNTs) containing nanopores between the nanotubes on the surface. This method includes: (a) providing a carbon source gas and a catalyst gas through a nozzle onto a heated surface; (b) forming a carbon nanotube filter; and (c) removing the carbon nanotube filter from the surface. A strong advantage of this method is that CNT bundles are produced in one step, without any prior substrate preparation [43-44].

The range of inner and outer diameters of these nanotubes has been estimated to be ~10–12 nm and ~20–40 nm, respectively from TEM analysis. The value for the tensile strength of filter measured ~2.2 MPa and the Young's modulus obtained from the true stress versus the true strain curves was ~50 MPa. They expressed that this filter is able to eliminate nanoscale pollutants from water and multiple components of heavy hydrocarbons from crude oil, effectively. These filters have very suitable accuracy in different applications, for example they could remove bacterial contaminants such as nanoscale poliovirus and larger pathogens such as Escherichia coli (E. coli) and Staphylococcus bacteria from water. The filtration process itself was driven by gravity as no additional pressure was applied. As many of the nanotube's internal spaces possibly have plugs of metal particles, they believe that most of the filtering occurs in the

interstitial spaces. Holt et al. (2004, 2006) reported synthesis of free-standing and silicon-chip supported vertically aligned CNT membranes by CVD method [45-46]. They entered ethylene/argon/hydrogen feed solution in reaction zone while the temperature is ramped up to the growth temperature of 850°C. Nanotube growth occurs typically for 20 minutes and results in a dense array of multiwalled nanotubes of ~5 μm length and 20-50 nm diameter.

Gu et al. (2006) performed direct tensile tests of double walled carbon nanotube (DWCNT) membranes with thickness of 40–80 nm using a micro-stress-strain puller [47]. The tensile strength and Young's modulus were measured 480–840 MPa and 4.4–8.8 GPa, respectively. It should be mentioned that they used an aluminum foil substrate to prepare the samples used for the tensile test. 12 samples broke between the platforms, and there was no slippage or extension between the membrane and the foil which was selected from more than 30 measured samples. Since the membrane was so thin, they could estimate the free volume only by its plane density which is assumed to be 75% by SEM images. So the percentage of effective cross-sectional area was determined 25%. Therefore, the real tensile strength and Young's modulus was increased four times.

Mi et al. (2007) prepared the CNT layer consisting of fairly straight carbon nanotubes of 6.3 nm in pore diameter running parallel to each other [48]. They used the α-Al_2O_3 disks substrate on one surface, which was polished with sandpaper and cleaned in an ultrasonic acetone bath for 30 min, in CVD method. About 0.1 g of ferrocene vapor was decomposed (at 800°C) and iron nanoparticles were formed and deposited on the surface of the alumina substrate. Mixture of acetylene and nitrogen in 1:10 ratio was later introduced to the CVD reactor at a flow rate of 10 cm^3/min for about 10 min. Then the inter-tube gaps of the CNT array on the alumina support were filled with a 30 wt% solution of polystyrene (PS) in toluene by spin-coating. After coating, the CNT membrane was dried at 60°C for 3 days. The surface of the coated CNT appeared white, indicating that the black CNT was completely covered by the white PS over-layer.

Unlike Hinds et al., these researchers used a simple mechanical polishing method (with soft sand) to remove PS over-layer and to open the closed tips of CNTs. The sanding process continued until black CNTs appeared on the surface. The composite membrane complete removal of encapsulated catalyst particles on the bottom of CNT tips. From SEM micrograph, CNT membranes areal density on the porous alumina was estimated about 1.87×10^9 CNT/cm^2, lower than the CNT membranes on dense silicon and quartz support which is reported in the literature. They show that the gas permeance through the porous alumina-supported CNT membranes is inversely proportional to the squared root of the gas molecules suggesting a Knudsen diffusion mechanism because of minimum mass transfer resistance of CNTs.

Mostafavi et al. (2008) to complete the researches of Hinds and Srivastava, used hexane feed instead of toxic gases -hexane is more environmentally benign than benzene and xylene- and prepared a nanostructure filter to remove viruses from water [44]. Their work's results showed that at pressures of 8-11 bar, the MS2 viruses were removed with a high efficiency by using the fabricated nanofilter. Janowska et al. (2008) was synthesized an aligned carbon nanotube carpet by catalytic chemical vapor deposition (CCVD) process at 800°C with a mixture of ferrocene and toluene, using a removable quartz substrate as macroscopic pre-form and self-supported aligned nanotubes could be obtained (Figure 4) [31]. The aligned nanotube array was efficiently used as removable precursor template in the design of ceramic nanoporous membranes with a mean diameter in the 40–60 nm range. The ferrocene concentration in the toluene solution was 20 g/l which was carried out into the reaction zone by a 1.5 l/min argon flow. The thickness of the carbon nanotube pattern could be accurately controlled by adjusting the synthesis duration, i.e. 1200 μm thickness for 2 h of synthesis and 250 μm for 0.5 h of synthesis.

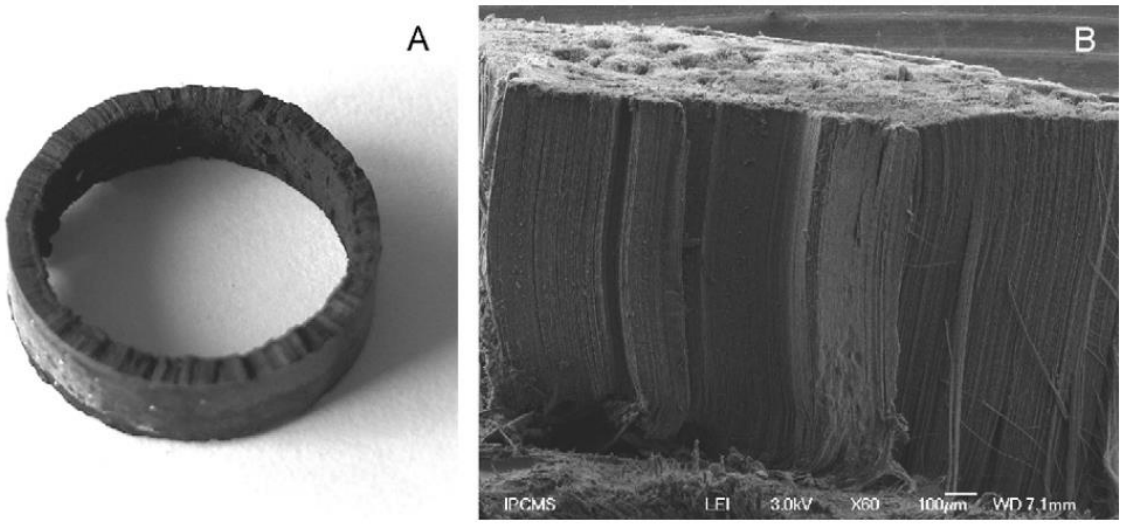


Figure 4. Macrostructures of self-supported aligned carbon nanotubes obtained after dissolving the quartz growth substrate in a HF solution: (A) ring and (B) plate (Janowska et al., 2008)

The CNT array was relatively dense with a spacing of about 100 nm between neighboring CNTs. Since careful SEM observation of the top of the CNT forest didn't show any iron particles attached at the tube tip, it seems the growth mechanism of CNTs has been root-growth in which the iron catalyst remained attached to the substrate surface and the nanotubes were slowly lift-off with aligned morphology.

They treated the aligned CNT carpet in an acidic solution, HNO_3 30 vol.%, at 80°C for overnight in order to remove from the sample the remaining iron-based catalyst. The sample was washed several times with distilled water until the pH reached a neutral value. Scholars believe that wetting and drying processes would induce the tube gathering by the van der Waals forces and would lead to high mechanical strength of structure. According to their statements this membrane can be used for filtration of fine particulate matter such as viruses from water or in airborne conditions.

Prehn et al. (2008) developed catalytically active CNT-polymer-membrane assemblies [42]. The process included the nanotube synthesis, sputter deposition of platinum as a catalyst and the membrane casting. They inserted ferrocene as a catalyst and toluene as carbon source in the process to form iron containing CNTs on a silicon substrate. In the CVD process toluene was used as the solvent and carbon source to which 2 or 8 wt% ferrocene was added. These ferrocene–toluene solutions were inserted into the preheated zone (200°C) of a two-stage oven via a syringe pump. Both materials typically vaporise under these conditions (given vaporization temperatures of 175°C for ferrocene and 110°C for toluene). A mixture of argon and 10 vol.% hydrogen was used as carrier gas with a total flow rate of 750 ml/min while the injection rate of ferrocene–toluene was set to 5 ml/h. Final temperature of the reaction zone reached 760°C. In the first step a polystyrene (PS) foil was hot pressed on the CNT tips that previously were covered with platinum. Specification of CNTs was different based on toluene wt% and synthesis time (Table 1). After producing the CNTs, they were strengthened with polystyrene and platinum. It was the first report of producing a catalytically active CNT membrane.

Table 1. Comparison of CNTs Specification based on toluene wt% and synthesis time

toluene wt%	synthesis time (min)	Mean Length of CNTs (nm)	Mean Diameter of CNTs (nm)
8	60	300	65
2	60	150	45
2	45	65	30

Yu et al. (2008) prepared high-density, vertically aligned carbon nanotube (VA-CNT) membranes [49]. Vertically aligned CNT forests were grown by water-assisted CVD synthesis at 750°C and reached approximately 2 mm in length in 120 min. Then, the free-standing arrays were soaked in n-hexane solvent, and the layers were dried at room temperature. After shrinkage by n-hexane evaporation, the interstitial pores reduced to an average size from 28 nm to 6 nm. As indicated in Figure 5, the as-grown VA-CNT forest shrank to approximately 5% of its original area after n-hexane evaporation and became dense. Also the CNTs were still aligned and no cracks were seen. Their dense membranes had two advantages: their CNT density was 8 to 270 times more than previous CNT membranes, and they did not need any polymeric binder.

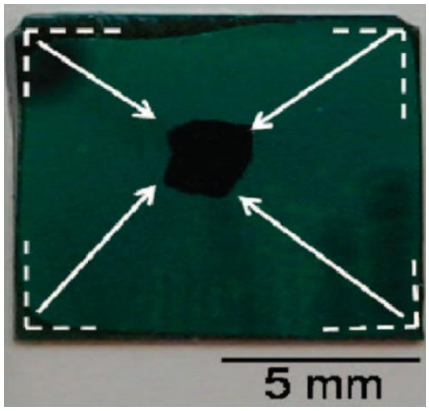


Figure 5. Photograph of a dense CNT membrane after n-hexane evaporation, white dotted lines indicate the original size of as-grown CNT forest (Yu et al., 2009)

Mirbagheri et al. (2012) report an efficient process to grow well-aligned carbon nanotube (CNT) arrays with a good area distribution density [30]. Vertically aligned carbon nanotubes (VA-CNTs) have been produced by controlling flow rate, temperature and catalyst nanoparticles using a floating catalyst CVD technique. They were synthesized on quartz substrates at 800°C from toluene as a carbon source. The Samples were characterized by SEM and TEM, and their surface area and pore size were determined by nitrogen adsorption analysis. The synthesized CNTs have a length of 500 μm and diameters ranging 120±40 nm. As the CNT filaments form a strength structure and exhibit a good vertical alignment, they propose CNT Membranes for separation applications, especially for water and wastewater treatment as hydraulic microstructures.

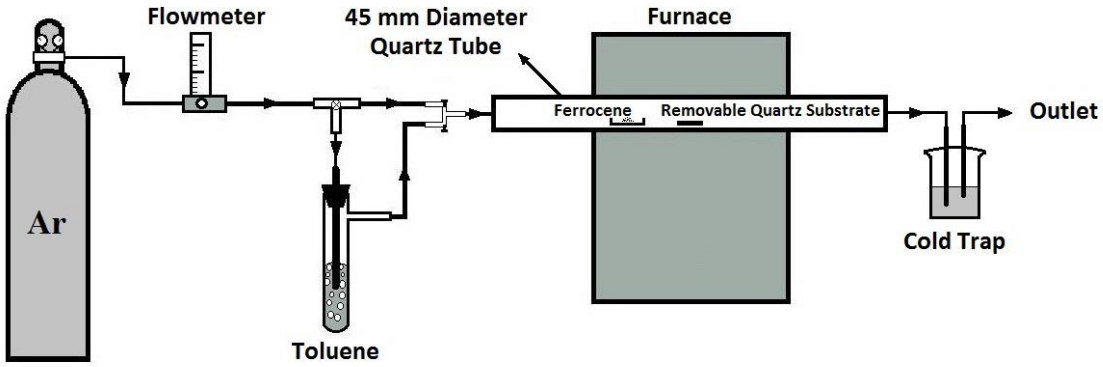
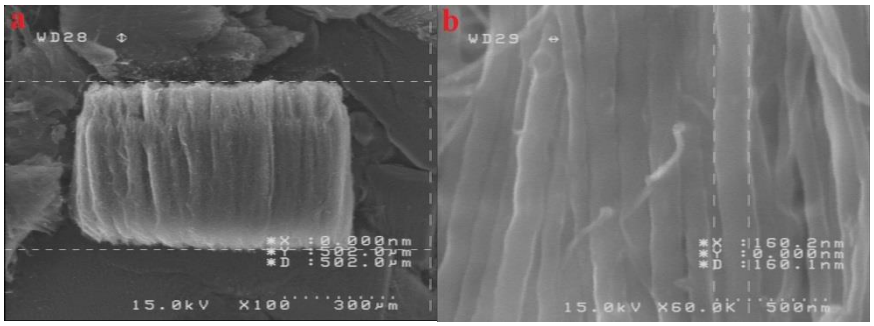


Figure 6. Schematic diagram of FC-CVD method for growing VA-CNTs (Mirbagheri et al., 2012)



mi

Figure 7. SEM image shows align microstructure of samples and (a) length and (b) formation of VA-CNTs (Mirbagheri et al., 2012)

3. Advantages and disadvantages of CNT membranes

CNT is one of the strongest and stiffest materials discovered yet, because of its tensile strength and elastic modulus (Young's modulus). This strength results from the covalent sp^2 bonds formed between the individual carbon atoms [50]. This bonding structure, which is stronger than the sp^3 bonds found in diamonds, provides the molecules with their unique strength. Young's modulus along the CNT's axial direction is enormous [51]. CNTs have remarkable flexibility due to their high length [52]. As a result, they are very suitable for use in compounds that need heterogeneous properties.

In 2000, the tensile strength of a MWNT was measured about 63 GPa [53]. In comparison, high-carbon steel has a tensile strength of approximately 1.2 GPa. Also, an individual tube has an elastic modulus of about 1 TPa [54]. Since CNTs have a low density for a solid of 1.3-1.4 g/cm^3, its specific strength of up to 48000 kN·m/kg is the best of known materials, compared to steel's 254 kN·m/kg [27, 55-566].

CNT chemical reactivity is directly related to the pi-orbital mismatch caused by an increased curvature [36]. This is why these materials are more resistant to chemical reactions than polymeric materials in hydraulic microstructures (membranes) [3657].

Using CNTs in the membranes caused high speed fluid transport [31, 41, 46], easy cleaning [42, 44], increased mechanical strength, reusability and thermal resistance (about 400°C) [43, 57]. Although the mineral membranes are expensive in comparison to organic membranes, some benefits such as mechanical and thermal strength, align and strong structure of pores and the

chemical resistance still keep them competitive with each other. Since the researchers in recent years are brought to build laboratory membranes, certainly solving the problems and completing their researches will appropriate the industrialization method of fabricating these membranes as hydraulic microstructures.

4. Summary and conclusion

Although membrane technology is used in different industrial parts, due to the prosperous future ahead, extensive research is still being carried out. Regarding CNT membranes, most researchers' attention will be focused on the composition and regularly structure of nanotubes and various compounds will be tested to achieve the best separation properties with long-term and improved resistance in future. Table 2 shows the summary of the information on CNT membranes taken from the literature.

Table 2. Summary of CNT membranes information fabricated by pervious researchers

Group, Year	Carbon Source	Catalytic Source	Substrate	Carrier Gases			Reaction Temperature (°C)	Reaction Time (min)	Mean Diameter of CNTs (nm)	Mentioned Application
				Hydrogen	Argon	Nitrogen				
Chengwei, 2000 [34]	Acetylene	Iron	Alumina	Yes	No	No	700	120-360	60-72	Gas Separation
Hinds, 2003 [41]	Xylene	Ferrocene	Quartz	Yes	Yes	No	700	30	2-6.6	Separation Processes
Srivastava, 2004 [43]	Benzene	Ferrocene	Quartz	No	Yes	No	900	-	10-12	Heavy Hydrocarbons Separation from Crude Oil/ Virus Removal from Water
Holt, 2006 [46]	Ethylene	Iron	Silicone	Yes	Yes	No	850	20	20-50	Separation Processes
Mi, 2007 [48]	Acetylene	Ferrocene	Alumina	No	No	Yes	800	10	6.5	Gas Separation
Mostafavi, 2008 [44]	Hexane	Ferrocene	Quartz	Yes	No	No	900	95	30	Virus Removal from Water
Janowska, 2008 [31]	Toluene	Ferrocene	Quartz	No	Yes	No	800	30-120	40-60	Virus Removal from Water
Prehn, 2008 [42]	Toluene	Ferrocene	Silicone	Yes	Yes	No	760	45-60	30-65	Separation Processes
Mirbagheri, 2012 [30]	Toluene	Ferrocene	Quartz	No	Yes	No	800	60	80-160	Water and Wastewater Treatment

Considering the unique properties of carbon nanotubes, such as high flow rate, easy cleaning, excellent strength, chemical and thermal stability, they could be used as membranes in

separation processes of chemical industries and treatment of nano-scale suspended pollutants of water in environmental engineering.

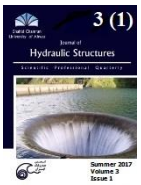
5. References

1. Van Rijn, C.J.M., "Nano & Micro Engineered Membrane Technology: Vol. 10 (Membrane Science and Technology)", 2004, Elsevier, Netherlands
2. Hubbard, T., "Encyclopedia of Surface & Colloid Science", Vol. 3, 2002
3. Mulder, M., "Basic principles of membrane technology", 1996, kluwer academic publisher, Netherlands
4. Wenten, I.G., "Recent Development in Membrane Science & its Industrial Applications", Songklanakarin Journal Science & Technology, Vol. 24, 2002, Malaysia
5. Baker, R.W., "Membrane Technology & Applications", 2nd Ed., 2004, John Wiley & Sons
6. Strathmann, H., Giorno, L., Drioli, E., "An Introduction to Membrane Science & Technology", Institute on Membrane Technology, 2006, CNR-ITM, Italy
7. Nunes, S.P., and Peinemann, K., "Membrane Technology in the Chemical Industries", 2001, Wiley-VCH
8. Mason, E.A., "from pig bladders and cracked jars to polysulfones: an historical perspective on membrane transport", Journal of Membrane Science, 60, 1991
9. Keizer, K., and Verweij, H., "Progress in inorganic membranes", Chemical Technology, 1996
10. Ismail, A.F., David, L.I.B., "A review on the latest development of carbon membranes for gas separation", Journal of Membrane Science, 193, 2001
11. Soria, R., "Overview on industrial membranes", Catalyst Today, 1995
12. Hsieh, H.P., "Inorganic membranes", Membrane Material Process, 1990
13. Mirbagheri, S.A., Mousavi Rad, S.A., Mohammadi, T., "Treatment of Electroplating Wastewater by Reverse Osmosis Membrane", Proceedings of First International Conference on Advances in Wastewater Treatment and Reuse, 2009, Iran
14. Mousavi Rad, S.A., Mirbagheri, S.A., Mohammadi, T., "Using Reverse Osmosis Membrane for Chromium Removal from Aqueous Solution", Proceedings of World Academy of Science, Engineering and Technology, 57, 2009, Netherlands
15. Kim, S., Jinschek, J.R., Chen, H., Sholl, D.S., Marand, E., "Scalable Fabrication of Carbon Nanotube/Polymer Nanocomposite Membranes for High Flux Gas Transport", Nano Letters, 9, 2007
16. Iijima, S., "Helical microtubules of graphitic carbon", Nature, 354, 1991
17. Ajayan, P.M., "Nanotubes from Carbon", Chemical Reviews, 1999
18. Qian, D., Wagner, G.J., Liu, W.K., Yu, M.F., Ruoff, R.S., "Mechanics of carbon nanotubes", Applied Mechanics Reviews, 55(6), 2002
19. Koohsorkhi, J., Abdi, Y., Mohajerzadeh, S., Hosseinzadegan, H., Komijani, Y., Soleimani, E.A., "Fabrication of self-defined gated field emission devices on silicon substrates using PECVD-grown carbon nano-tubes", Carbon (44), 2006
20. Hosseini, A.A., Taleshi, F., Tajbakhsh, M., Farhang, M., "Synthesis and characterization of sol-gel derived MgO/CNTs nanocomposite", Journal of Chemistry and Chemical Engineering, USA, in press
21. Upadhyayula, V.K.K., Deng, S., Mitchell, M.C., Smith, G.B., "Application of carbon nanotube technology for removal of contaminants in drinking water: A review", Science of the Total Environment, 408, 2009

22. Zhang, W.D., Wen, Y., Liu, S.M., Tjiu, W.C., Xu, G.Q., Gan, L.M., “Synthesis of vertically aligned carbon nanotubes on metal deposited quartz plates”, Carbon, 40, 2002
23. Li, X., Zhu, G., Dordick, J.S., Ajayan, P.M., “Compression-Modulated Tunable-Pore Carbon Nanotube Membrane Filters”, Small, 3, 2007
24. Noy, A., Park, H.G., Fornasiero, F., Holt, J.K., Grigoropoulos, C.P., Bakajin, O., “Nanofluidics in carbon nanotubes”, Nanotoday, 6, 2007
25. Liu, H., Zhang, Y., Arato, D., Li, R., Mérel, P., Sun, X., “Aligned multi-walled carbon nanotubes on different substrates by floating catalyst chemical vapor deposition: Critical effects of buffer layer”, Surface & Coatings Technology, 202, 2008
26. Dai, H., “Nanotube Growth and Characterization”, Topics in Applied Physics, 2001, Springer
27. Miri, S.A.M., "Carbon Nanotubes and Their Fabrication Method", Imam Hossein University Publication, (in Persian), 2006
28. Manafi, S.A., Amin, M.H., Rahimipour, M.R., Salahi, E., Kazemzadeh, A., "Carbon nanotubes synthesized by mechanothermal Method", New Carbon Materials, 24(1), 2009
29. Manafi, S.A., Amin, M.H., Rahimipour, M.R., Salahi, E., Kazemzadeh, A., "High-yield Synthesis of Multiwalled Carbon Nanotube by Mechanothermal Method", Nanoscale Research Letters, 4, 2009
30. Mirbagheri, S.A., Kazemzadeh, A., Maghanaki, A. A., "Macroscopic Synthesis of Vertically Aligned Carbon Nanotubes Using Floating Catalyst Chemical Vapor Deposition Method", Japanese Journal of Applied Physics, 2012
31. Janowska, I., Hajiesmaili, S., Begin, D., Keller, V., Keller, N., Ledoux, M.J., Pham-Huu, C., “Macronized aligned carbon nanotubes for use as catalyst support and ceramic nanoporous membrane template”, Catalysis Today, 2008
32. Ajayan, P.M., Stephan, O., Colliex, C., Trauth, D., “Aligned Carbon Nanotube Arrays Formed by Cutting a Polymer Resin-Nanotube Composite”, Science, 1994
33. de Heer, W.A., Bacsa, W.S., ChAtelain, A., Gerfin, T., Humphrey-Baker, R., Forro, L., Ugarte, D., "Aligned Carbon Nanotube Films: Production and Optical and Electronic Properties", Science, 1995
34. Chengwei, W., Menke, L., Shanlin P., Hulin, L., “Well-aligned carbon nanotube array membrane synthesized in porous alumina template by chemical vapor deposition”, Chinese Science Bulletin, 2000
35. Sinnott, S.B., Andrews, R., Qian, D., Rao, A.M., Mao, Z., Dickey, E.C., Derbyshire, F., "Model of Carbon Nanotube Growth Through Chemical Vapor Deposition", Chemical Physics Letters, 315, 1999
36. Daenen, M., De Fouw, R.D., Hamers, B., Janssen, P.G.A., Schouteden, K., Veld, M.A.J., "The Wondrous World of Carbon Nanotubes", internal report, Eindhoven University of Technology, 2003
37. Hosseini, A.A.,Taleshi, F., “Large diameter MWNTs growth on iron-sprayed catalyst by CCVD method under atmospheric pressure”, Indian Journal of Physics, Springer, 2010
38. Casavant, M. J., Walters, D. A., Schmidt, J. J., Smalley, R. E., “Neat macroscopic membranes of aligned carbon nanotubes”, Journal of Applied Physics, 2003
39. Walters, D.A., Casavant, M.J., Qin, X.C., Huffman, C. B., Smalley, R.E., “In-plane-aligned membranes of carbon nanotubes”, Chemical Physics Letters, 2001
40. Shimoda, H., Fleming, L., Horton, K., Zhou, O., “Formation of macroscopically ordered carbon nanotube membranes by self-assembly”, Physica B, 2002

41. Hinds, B. J., Chopra, N., Rantell, T., Andrews, R., Gavalas, V., Bacha, L. G., "Aligned Multiwalled Carbon Nanotube Membranes", sciencexpress, 2003
42. Prehn, K., Adelung, R., Heinen, M., Nunes, S.P., Schulte, K., "Catalytically active CNT-polymer-membrane assemblies: From synthesis to application", Journal of Membrane Science, 2008
43. Srivastava, A., Srivastava, O. N., Talapatra, S., Vajtai, R., Ajayan, P. M., "Carbon Nanotube Filters", Science: Nature Materials, 2004
44. Mostafavi, S.T., Mehrnia, M.R., Rashidi, A.M., "Preparation of nanofilter from carbon nanotubes for application in virus removal from water", Desalination, 2009
45. Holt, J.K., Park, H.G., Noy, A., Huser, T., Eaglesham, D., Bakajin, O., "Carbon nanotube-based membranes: a platform for studying nanofluidics", 4th IEEE conference on nanotechnology, 2004, Munich, Germany
46. Holt, J.K., Park, H.G., Wang, Y., Stadermann, M., Artyukhin, A.B., Grigoropoulos, C.P., Noy, A., Bakajin, O., "Fast Mass Transport Through Sub–2-Nanometer Carbon Nanotubes", Science, 2006
47. Gu, Z., Wang, K., Wei, J., Li, C., Jia, Y., Wang, Z., "Tensile properties of ultrathin double-walled carbon nanotube membranes", Carbon, 2006
48. Mi, W., Lin, Y.S., Li, Y., "Vertically aligned carbon nanotube membranes on macroporous alumina supports", Journal of Membrane Science, 2007
49. Yu, M., Funke, H.H., Falconer, J.L., and Noble, R.D., "High Density, Vertically-Aligned Carbon Nanotube Membranes", Nano Letters., 2009
50. Pierson, H.O., "Handbook of carbon, graphite, diamond, and fullerenes: properties, processing and applications", Noyes Publications, 1993
51. Garcia, E.J., John Hart, A., Wardle, B.L., Slocum, A.H., "Fabrication and Nanocompression Testing of Aligned Carbon-Nanotube–Polymer Nanocomposites", Advanced Materials, 2007
52. Iijima, S., Brabec, C., Maiti, A., Bernholc, J., "Structural flexibility of carbon nanotubes", Chemical Physics, 1996
53. Yu, M.F., Lourie, O., Dyer, M.J., Moloni, K., Kelly, T.F., "Strength and Breaking Mechanism of Multiwalled Carbon Nanotubes Under Tensile Load", Science, 2000
54. Forro, L., Salvetat, J.P., Bonard, J. M., Basca, R., Thomson, N. H., Garaj, S., Thien-Nga, L., Gaal, R., Kulik, A., Ruzicka, B., Degiorgi, L., Bachtold, A., Schonenberger, C., Pekker, S., Hernadi, K., "Electronic and Mechanical Properties of Carbon Nanotubes", Technical Report
55. Mori, K., Akita, K., Abe, Y., "Springback behaviour in bending of ultra-high-strength steel sheets using CNC servo press", Machine Tools & Manufacture, 2007
56. Li, Y., Wang, K., Wei, J., Gu, Z., Wang, Z., Luo, J., Wu, D., "Tensile properties of long aligned double-walled carbon nanotube strands", Carbon, 2005
57. Majumder, M. and Ajayan, P.M., "Carbon Nanotube Membranes: A New Frontier in Membrane Science", in: Drioli E., and Giorno, L., "Comprehensive Membrane Science and Engineering", Oxford Academic Press, 2010

Journal of Hydraulic Structures
***J. Hydraul. Struct.*, 2017; 3(1):14-34**
DOI: 10.22055/jhs.2017.13281



Estimation of Fracture path in the Structures and the Influences of Non-singular term on crack propagation

A.G. Khademalrasoul[*1]
R. Maghsoudi[2]

Abstract

In the present research, a fully Automatic crack propagation as one of the most complicated issues in fracture mechanics is studied whether there is an inclusion or no inclusion in the structures. In this study The Extended Finite Element Method (XFEM) is utilized because of several drawbacks in standard finite element method in crack propagation modeling. Estimated Crack paths are obtained by using Level Set Method (LSM) in coupling with XFEM for 2D mixed mode crack propagation problems. Also, stress intensity factors for mixed mode crack problems are numerically calculated by using interaction integral method completely based on familiar path independent J-integral approach. However, the influence of the first non-singular term (T-stress) of Williams' stress distribution series in a cracked body is considered. Different crack growth paths are calculated for different domains with predefined notches such as edge and center cracks. In addition, predefined cracks and inclusions are implicitly defined using enrichment procedure in the XFEM framework and the effects of soft or hard inclusions are studied on crack propagation schemes. Finally, estimated crack paths under assumed conditions by using XFEM, are compared with the experimental results.

Keywords: Extended Finite Element Method, Level Set Method, Interaction integral, Soft and Hard inclusions, T-stress.

Received: 08 March 2017; Accepted: 20 June 2017

1. Introduction

Hydraulic structures are in a danger of cracking and the analysis of cracked hydraulic structure is very crucial for engineers. Dams and levees are some critical examples which propagating cracks can cause them to failure. Transverse and longitudinal cracking of embankment structures are common types of discontinuities in crown and the upstream\downstream slopes [1]. Also various types of cracks with random inclination angles in

[1] Faculty of Engineering, Department of Civil Engineering, Shahid Chamran University of Ahvaz, Ahvaz, Iran. (**Corresponding author**)
[2] Department of Civil Engineering, Esfarayen University of Technology, Esfarayen, North Khorasan, Iran.

concrete dams are possible. These strong discontinuities can arise from the date of construction or induced by fatigue phenomenon. When the structure has a strong discontinuity as long as subjected to loading, the crack will propagate. Therefore, large stress concentrations are avoided and a reasonable margin of security is taken to ensure that values close to the maximum admissible stress are never attained. Previous studies have demonstrated that structural failure might be happened in a lower applied loads; when there is a crack in the structure [11-13].

In such a case, the traditional finite element method cannot easily establish to simulate the propagating crack. Since in the finite element framework the domain of interest is defined by the mesh, therefore, the discontinuities have to be conformed onto the mesh [2, 3]. Consequently, at least for each increment of the crack growth, the domain surrounding the crack tip must be remeshed such that the updated crack geometry is accurately represented [4, 5]. However, In spite of progress of mesh generators, initial creation of the mesh with a crack and in the case of propagating crack, the modification of the initial mesh remains extremely heavy and difficult.

However, Extended finite element method (XFEM) is one of the capable numerical approaches in fracture mechanics [4, 18].The combination of the XFEM by the Level Set Method (LSM) has been utilized to eliminate the cumbersome task of discontinuity modeling and the evolution of the internal discontinuous boundaries [19, 20]. The mathematical vision of the XFEM is based on the concept of discontinuous and asymptotic partition of unity enrichment (PUM) of the standard finite element approximation spaces. In the XFEM the discontinuities are conformed implicitly on the finite element domain [21]. In fact by using the additional degrees of freedom every kind of discontinuities are imposed on the solution field [22-25].

The first non-singular term of stress distribution series is called *T*-stress. The value of *T*-stress can be zero, positive or negative. *T*-stress significantly affects the shape and size of the plastic zone which develop at the vicinity of the crack tip. This term is a constant stress value and is independent of the distance to the crack tip. The *T*-stress is parallel to the crack surface. By considering the small-scale yielding condition, the effects of *T*-stress has been investigated on crack propagation problems [6-10].

Also, the concept of stress intensity factor (SIF) plays a central role in fracture mechanics. SIF depend on the geometry, crack length and loading conditions. Among several ways for evaluating the SIFs, the approaches which based on the concept of the energy are the most applicable methods [14-17]. According to the SIFs in mixed mode condition of loading, the crack propagation angle is calculated. Hence, the crack path would be predicted. The critical situation for an embankment is when the crack propagates and reaches to the dam's core. So, the estimation of the crack path is a crucial importance of dam safety monitoring.

Strong discontinuities (edge and center cracks), inclusions (soft or hard internal boundaries) and voids are created implicitly using enrichment procedure and any evolutions are taken into account by the level set definitions. In this research work the crack propagation in the presence of both soft and hard inclusions is studied in complicate conditions. To fulfillment of this objective a numerical computer program is prepared. In this computer code modeling of all types of internal heterogeneous boundaries are possible by using the level set approach. Therefore, without any internal excessive meshing or remeshing, internal boundaries are created in the finite element framework. Also, by using level set method any form of the conflict of internal boundaries are possible. Differences between maximum tangential stress (MTS) criterion and generalized MTS (GMTS) criterion are demonstrated.

The paper is outlined as follows; Section 2 presents the principle of linear elastic fracture mechanics and states the numerical calculation method of mixed-mode stress intensity factors. Section 3 is performed to introduce the principle of the enriched finite element method. Section

4 introduces the principles of the level set method. Numerical examples are listed in Section 5. Section 6 dedicates to conclude remarks.

2. Stress Intensity Factors

Behavior of a body with a discontinuity such as crack is generally characterized by a parameter such as stress intensity factors (SIFs) or path independent *J*-integral in linear elastic fracture mechanics. Also, during last decades much effort has been done on SIFs calculation. Theoretical, numerical and experimental methods have been employed for determination of the SIFs in the vicinity of the crack tips. According to two independent kinematic movements of upper and lower crack surfaces in 2D analysis, there are opening and sliding modes [15, 16, 26, 27]. Williams' asymptotic solution for crack-tip stress fields in any linear elastic body is given by a series of the form [28]:

$$\sigma_{ij}(r,\theta) = A_1 r^{-1/2} f_{ij}^{(1)}(\theta) + A_2 f_{ij}^{(2)}(\theta) + A_3 r^{1/2} f_{ij}^{(3)}(\theta) + \text{higher order terms}, \tag{1}$$

where σ_{ij} is the stress tensor, r and θ are polar coordinates with the origin at the crack tip (as shown in Figure 1). $f_{ij}^{(1)}, f_{ij}^{(2)}, f_{ij}^{(3)}$ are universal functions of θ, and A_1, A_2, A_3 are parameters proportional to remotely applied loads. In the vicinity of the crack tips, the leading term which exhibits a square-root singularity dominates. The amplitude of the singular stress fields is characterized by the SIFs, i.e. [28]

$$\sigma_{ij} = \frac{K_I}{\sqrt{2\pi r}} f_{ij}^{I}(\theta) + \frac{K_{II}}{\sqrt{2\pi r}} f_{ij}^{II}(\theta), \tag{2}$$

where K_I, K_{II} are the stress intensity factors for the opening (mode I) and shearing (mode II) modes respectively. However, the *K* field is not the exact solution to the stress field in a cracked body. It is the solution to the stress field as the crack tip is approached, where the approximations used in the derivation of the *K* field apply. The second term in the Williams' series solution (Eq. (1)) is a non-singular term, which is defined as the elastic *T*-stress. Thus the above expression (Eq. (2)) can be expanded to include this term as follows

$$\sigma_{ij} = \frac{K_I}{\sqrt{2\pi r}} f_{ij}^{I}(\theta) + \frac{K_{II}}{\sqrt{2\pi r}} f_{ij}^{II}(\theta) + T\,\delta_{1i}\delta_{1j}. \tag{3}$$

The *T*-stress varies with different crack geometries and loadings. It plays a dominant role on the shape and size of the plastic zone, the degree of local crack tip yielding, and also in quantifying fracture toughness. For mixed-mode problems, the *T*-stress contributes to the tangential stress and, as a result, it affects the crack growth criteria. By normalizing the *T*-stress with applied load $\sigma_0 \left(= K_I / \sqrt{\pi a}\right)$, a is the crack length, a non-dimensional parameter B_T can be defined by [10, 29]

$$B_T = T\sqrt{\pi a}/K_I. \tag{4}$$

The dependence on geometrical configurations can be best indicated by the biaxiality parameter B_T.

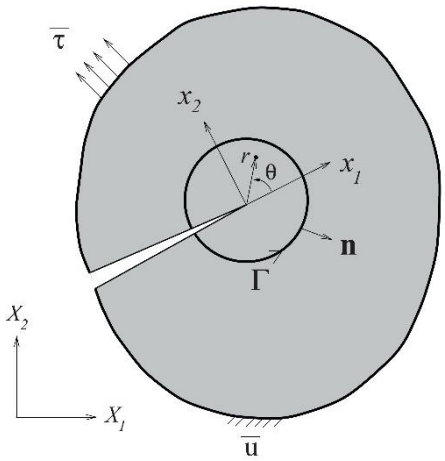


Figure 1. ***Coordinate system and integration path, $\bar{u}$ denotes prescribed displacement and $\bar{\tau}$ denotes prescribed tractions[30].***

2.1. *M*-integral

The *M*-integral is based on well-known path independent *J*-integral. The *J*-integral as a path independent integral, originally introduced by J.R. Rice to evaluate strain concentration by notches and cracks in a linear elastic or non-linear elastic and deformation-type elastic-plastic materials [31]. The *J*-integral is based on an energy balance and is equivalent to the energy release rate during crack extension in a homogeneous elastic body as follows[15]

$$\Pi_p\left(u_i\right)=\int_{\Omega} W\left(u_i\right)d\Omega-\int_{S_\sigma}\bar{T}_i\,u_i\,ds \tag{5}$$

$$J=-\frac{d\,\Pi_p}{da} \tag{6}$$

Consider a 2-D homogeneous crack body of linear or non-linear material free of body forces and tractions on the crack surfaces; the *J*-integral in numerical methods is usually defined as

$$J=\int_{\Gamma}\left[W\left(u_i\right)dx_2-\sigma_{ij}\,n_j\,\frac{\partial u_i}{\partial x_1}ds\right], \tag{7}$$

where $W(u_i)$ is the strain energy density with the following preconditions

$$\begin{aligned}
&W\left(u_i\right)=W\left(x,y\right)=W\left(\varepsilon\right)=\int_0^{\varepsilon}\sigma_{ij}\,d\,\varepsilon_{ij}\\
&\sigma_{ij}=\frac{\partial W}{\partial\varepsilon_{ij}}\quad(\text{Constitutive law})\\
&\varepsilon_{ij}=\frac{1}{2}(u_{i,j}+u_{j,i})\quad(\text{Compatibility})\\
&\sigma_{ij,j}=0\ \ and\ \ \sigma_{ij}=\sigma_{ji}\quad(\text{Equilibrium})
\end{aligned} \tag{8}$$

A path-independent integral technique known as interaction integral method is used for evaluating mixed-mode stress intensity factors (SIFs). The M-integral is the dual form of the *J*-integral. The *M*-integral is based on the principle of complementary energy, while the *J*-integral is based on the principle of potential energy or strain energy density [15]. Also, due to simplification of the numerical calculations, the *M*-integral is formulated on an equivalent

domain area of integration as follows;

$$\begin{aligned} & W\left(u_i\right)+B\left(\sigma_{ij}\right)=\sigma_{ij}\ \varepsilon_{ij} \\ & M=\frac{d\,\Pi_c}{da} \\ & \Pi_c\left(\sigma_{ij}\right)=\int_{\Omega} B\left(\sigma_{ij}\right)d\Omega-\int_{S_u}\bar{u}_i\ \sigma_{ij}\ n_j\ ds \\ & \varepsilon_{ij}=\frac{\partial B}{\partial \sigma_{ij}} \end{aligned} \tag{9}$$

For general mixed mode problems in 2D analysis we have the following relationship between the values of *J*-integral and the stress intensity factors.

$$J=\frac{K_I^2+K_{II}^2}{E_{eff}}, \tag{10}$$

E_{eff} is defined in terms of material parameters E (Young's modulus) and ν (Poisson's ratio) as;

$$E_{eff}=\begin{cases} E, & \text{Plane Stress} \\ \dfrac{E}{1-\nu^2}, & \text{Plane Strain} \end{cases} \tag{11}$$

For defining the *M*-integral two states of a cracked body are considered. State 1 ($\sigma_{ij}^{(1)}$, $\varepsilon_{ij}^{(1)}$, $u_i^{(1)}$) corresponds to the actual state and state 2 ($\sigma_{ij}^{(2)}$, $\varepsilon_{ij}^{(2)}$, $u_i^{(2)}$) is an auxiliary state which will be chosen as the asymptotic fields for modes I and II. There are two sets of auxiliary fields for stress and displacements; (1) SIfs auxiliary fields and (2) auxiliary fields for the *T*-stress calculation [30, 32, 33]. The J integral for the sum of the two states is

$$J^{(1+2)}=\int_{\Gamma}\left[\frac{1}{2}(\sigma_{ij}^{(1)}+\sigma_{ij}^{(2)})(\varepsilon_{ij}^{(1)}+\varepsilon_{ij}^{(2)})\delta_{1j}-(\sigma_{ij}^{(1)}+\sigma_{ij}^{(2)})\frac{\partial(u_i^1+u_i^2)}{\partial x_1}\right]n_j\,d\Gamma \tag{12}$$

Expanding and rearranging terms gives

$$J^{(1+2)}=J^{(1)}+J^{(2)}+M^{(1,2)}, \tag{13}$$

where $M^{(1,2)}$ is called the interaction integral for states 1 and 2

$$M^{(1,2)}=\int_{\Gamma}\left[W^{(1,2)}\delta_{1j}-\sigma_{ij}^{(1)}\frac{\partial u_i^2}{\partial x_1}-\sigma_{ij}^{(2)}\frac{\partial u_i^1}{\partial x_1}\right]n_j\,d\Gamma, \tag{14}$$

and $W^{(1,2)}$ is the interaction strain energy

$$W^{(1,2)}=\sigma_{ij}^{(1)}\ \varepsilon_{ij}^{(2)}=\sigma_{ij}^{(2)}\ \varepsilon_{ij}^{(1)}, \tag{15}$$

Writing Eq (12) for 2D problems for the combined states gives after rearranging terms

$$J^{(1+2)}=J^{(1)}+J^{(2)}+\frac{2}{E_{eff}}(K_I^{(1)}K_I^{(2)}+K_{II}^{(1)}K_{II}^{(2)}) \tag{16}$$

Then from the Eq (16) and (13) we have the following relationship

$$M^{(1,2)}=\frac{2}{E_{eff}}(K_I^{(1)}K_I^{(2)}+K_{II}^{(1)}K_{II}^{(2)}) \tag{17}$$

Finally the stress intensity factors for the current state can be found by separating the two modes of fracture in 2-D problems. By selecting $K_I^{(2)}=1$ and $K_{II}^{(2)}=0$, we are able to solve for $K_I^{(1)}$ such that

$$K_I^{(1)} = \frac{I^{(1,\,Mode\ I)} E_{eff}}{2} \tag{18}$$

Then a similar procedure can be followed to calculate the $K_{II}^{(1)}$ from the interaction integral method for a mixed mode fracture problems. Also the contour integral defining $M^{(1,2)}$ is converted into an area integral by multiplying the integrand by a bounded smoothing function $q(\mathbf{x})$ that is 1 on an open set containing the crack tip and vanishes on an outer prescribed contour Γ_0 then for each contour Γ (as shown in Figure 2) in this open set where $q(\mathbf{x}) = 1$ and assuming the crack faces are stress free and straight in the interior of the region A bounded by the prescribed contour Γ_0, the interaction integral may be written as

$$M^{(1,2)} = \int_C \left[W^{(1,2)} \delta_{1j} - \sigma_{ij}^{(1)} \frac{\partial u_i^2}{\partial x_1} - \sigma_{ij}^{(2)} \frac{\partial u_i^1}{\partial x_1} \right] q m_j \, d\Gamma , \tag{19}$$

where $C = \Gamma + C_+ + C_- + \Gamma_0$ and $\mathbf{m}$ is the outward unit normal to the contour C. Now using divergence theorem and passing to the limit as the contour Γ is shrunk to the crack tip, which is justified by the dominated convergence theorem, gives the following equation for the interaction integral in domain form as[4]

$$M^{(1,2)} = \int_A \left[\sigma_{ij}^{(1)} \frac{\partial u_i^2}{\partial x_1} - \sigma_{ij}^{(2)} \frac{\partial u_i^1}{\partial x_1} - W^{(1,2)} \delta_{1j} \right] \frac{\partial q}{\partial x_j} \, dA \tag{20}$$

The condition that the smoothing function is 1 on an open set containing the crack tip is easily relaxed to be just equal 1 at the tip. The interaction integral is calculated using stresses and strains of the Gaussian integration points in the finite element framework.

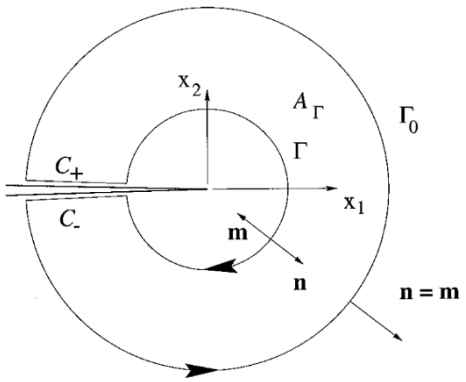


Figure 2. Equivalent domain for M-integral

2.2. Crack propagation angle

There are several approaches to predict the crack initiation angle for mixed mode fracture problems. The maximum tangential stress (MTS) criterion [34], the maximum energy release rate criterion[35], the minimum strain energy density criterion [36]. Based on the MTS criterion, a mixed mode crack propagates from the crack tip along the direction of maximum tangential stress, θ_c .According to this criterion, the direction of fracture initiation is determined from the following equation [37]:

$$\theta_c = 2\arctan\frac{1}{4}\left(\frac{K_I}{K_{II}} - sign\,(K_{II})\sqrt{\left(\frac{K_I}{K_{II}}\right)^2 + 8}\right), \tag{21}$$

where θ_c is given in the crack tip coordinate system, K_I and K_{II} are the mixed-mode stress intensity factors. The sign convention is such that $\theta_c < 0$ when $K_{II} > 0$ and vice versa.

In comparison with the conventional MTS criterion the generalized criterion makes use of a more accurate description for the crack tip stresses. It has been shown that [38] the tangential stress around the crack tip can be written as an infinite series expansion:

$$\sigma_{\theta\theta} = \frac{1}{\sqrt{2\pi r}}\cos\frac{\theta}{2}\left[K_I\cos^2\frac{\theta}{2} - \frac{3}{2}K_{II}\sin\theta\right] + T\sin^2\theta + O\left(r^{1/2}\right) \tag{21}$$

Where *T*-stress is the first non-singular term of series expansion. The higher order terms $O\left(r^{1/2}\right)$ are assumed to be negligible near the crack tip. Unlike the MTS criterion in the generalized MTS (GMTS) the influences of the *T*-stress is considered on the fracture initiation direction. Therefore, according to the MTS criterion the direction of fracture initiation angle θ_c is determined from [29]:

$$\left.\frac{\partial\sigma_{\theta\theta}(r,\,\theta)}{\partial\theta}\right|_{\theta=\theta_c} = 0, \qquad \frac{\partial^2\sigma_{\theta\theta}(r,\,\theta)}{\partial\theta^2} < 0 \tag{22}$$

So

$$\left[K_{\mathrm{I}}\sin\theta_c + K_{\mathrm{II}}\left(3\cos\theta_c - 1\right)\right] - \frac{16T}{3}\sqrt{2\pi r_c}\cos\theta_0\sin\frac{\theta_c}{2} = 0 \tag{23}$$

where r_c is the critical distance from the crack tip and is often considered as a constant material property. By normalizing *T*-stress and r_c as; $B = T\sqrt{\pi a/(K_I^2 + K_{II}^2)}$ and $\alpha = \sqrt{2r_c/a}$ the Eq. (23) can be written as follow

$$\left[K_{\mathrm{I}}\sin\theta_c + K_{\mathrm{II}}\left(3\cos\theta_c - 1\right)\right] - \frac{16B\alpha\sqrt{K_{\mathrm{I}}^2 + K_{\mathrm{II}}^2}}{3}\cos\theta_c\sin\frac{\theta_c}{2} = 0 \tag{24}$$

2.3. *T*-stress calculation

Since *T*-stress is a constant stress that is parallel to the crack, the auxiliary stress and displacement fields are chosen to a point force f in the locally x_1 direction, applied to the tip of a semi-infinite crack in an infinite homogeneous plate, as shown in Figure 3. The auxiliary displacements are[39]

$$\begin{aligned} u_1^{aux} &= -\frac{f\,(1+\kappa)}{8\pi\mu}\ln\frac{r}{d} - \frac{f}{4\pi\mu}\sin^2\theta \\ u_2^{aux} &= -\frac{f\,(\kappa-1)}{8\pi\mu}\theta + \frac{f}{4\pi\mu}\sin\theta\cos\theta \end{aligned} \tag{25}$$

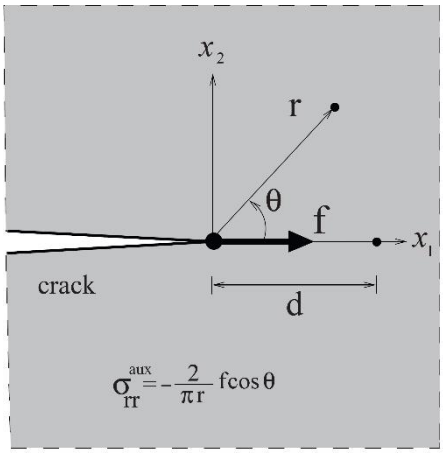


Figure 3. Local coordinates and point force f for T-stress calculation[30].

By considering the aforementioned auxiliary field, a simple expression for the *T*-stress in terms of the interaction integral (*M*-integral), the point force (f), and the material properties (E, ν) can be obtained.

$$T = \frac{E_{\text{eff}}}{f} M \tag{26}$$

where

$$f = -\lim_{\Gamma \to 0} \int_{\Gamma} \sigma_{ij}^{aux} n_j \, d\Gamma \tag{27}$$

3. Principles of Extended Finite Element Method

In the finite element method, the presence of flaws or inhomogeneities such as cracks, voids and inclusions must be taken into account in the mesh generation process. In the other hand the edges of the element must conform to these geometric entities. The XFEM aims to alleviate much of the burden associated with mesh generation for problems with any types of voids and interfaces by not requiring the finite element mesh to conform to the internal boundaries. The essence of the XFEM lies in sub-dividing a model into two parts: mesh generation for the domain which includes internal boundaries; and enriching the finite element approximation by additional functions that model the internal boundaries.

Extended finite element method has some special features in fracture mechanics. These special features of the extended finite element are due to partition of unity finite element (PUFEM) property of XFEM. The most prominent features of PUFEM are (1) the ability to include the local behavior of the solution in the finite element space, and (2) the ability to construct finite element spaces of any desired regularity. The XFEM can be assumed to be a classical FEM capable of handling arbitrary discontinuities. In fact, in The XFEM any types of discontinuities are modeled implicitly onto the domain of interest[40].The XFEM allows representing strong (cracks) and weak (holes, material interfaces) discontinuities. Arbitrarily oriented discontinuities can be modeled by enriching all elements cut by a discontinuity using standard enrichment functions. The enrichment functions should satisfy the discontinuous behavior and additional nodal degrees of freedom.

In the extended finite element method, first, the usual finite element mesh is produced, then, by considering the location of discontinuities, a few degrees of freedom are added to the classical finite element model in selected nodes near to the discontinuities .In the extended finite element method, the following approximation is utilized to calculate the displacement for the

point $\mathbf{x}$ locating within the domain[41]

$$\mathbf{u}^{\mathrm{h}}(\mathbf{x}_i) = \mathbf{u}^{\mathrm{FE}} + \mathbf{u}^{\mathrm{enr}} = \sum_{j=1}^{n} N_j(\mathbf{x})\mathbf{u}_j + \left(\sum_{k=1}^{m} N_k(\mathbf{x}) v(\mathbf{x}) \mathbf{a}_k \right) \tag{28}$$

where n is the number of the nodes in the finite element mesh, $N_j(\mathbf{x})$ is the shape function of node j, $\mathbf{u}_j$ are the classical degrees of freedom of node i and $v(\mathbf{x})$ is the enrichment function which is utilized to enrich the affected nodes by a discontinuity. Note that when there is no discontinuity in a domain the enrichment functions vanish. Since approximation in Eq. (28), does not satisfy the interpolation property; i.e., $\mathbf{u}_i \neq \mathbf{u}^h(\mathbf{x}_i)$ due to enriched degrees of freedom, the shifted enrichment function is employed to satisfy interpolation property[21].

3.1. Crack enrichment

In general, two different enrichment schemes are used for modeling a crack in homogeneous materials. Crack tip and Heaviside enrichment functions are implemented in the classical finite element method to the nodes of elements that influenced by the crack tip and body of the crack, respectively. It must be noted that there are different kinds of enrichment functions for strong and weak discontinuities in the XFEM. Figure 4, shows how classical FEM nodes are enriched to have an implicit crack on the domain of interest. For the elements which are completely cut by a crack body the Heaviside enrichment functions are employed as follows;

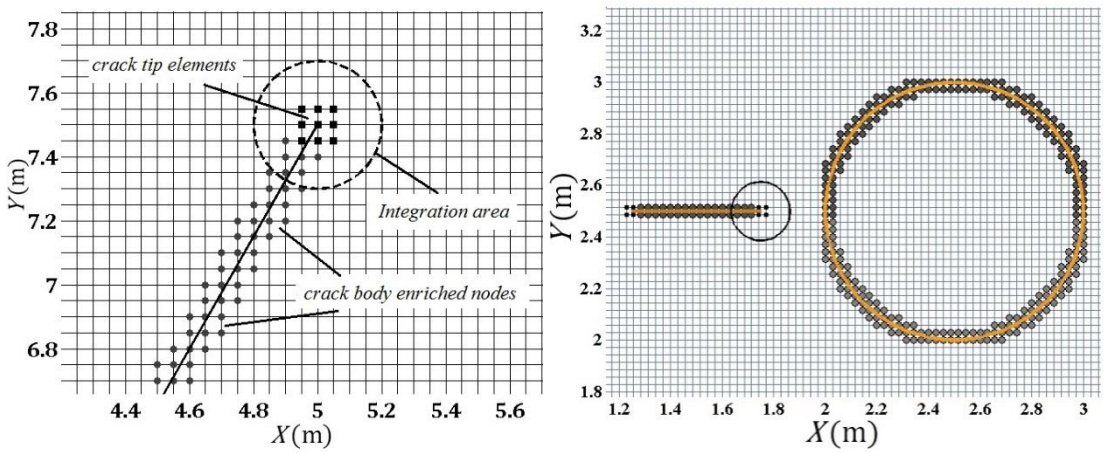


Figure 4. Crack tip and crack body enrichments with integration domain area (left), crack and inclusion enrichments (right).

$$H(x) = \begin{cases} +1 & \text{Above Crack} \\ -1 & \text{Below Crack} \end{cases} \tag{29}$$

For the case of an element containing the crack tip, the following four functions for the near tip displacement field are used. These asymptotic functions, originally introduced by Fleming for the representing crack tip displacement fields and repeated by Belytschko [18, 32, 42].The crack tip enrichment functions are as follows

$$\{F_\alpha(x)\}_{\alpha=1-4} = \left\{ \sqrt{r}\sin\frac{\theta}{2},\ \sqrt{r}\cos\frac{\theta}{2},\ \sqrt{r}\sin\theta\cos\frac{\theta}{2},\ \sqrt{r}\sin\theta\cos\frac{\theta}{2} \right\}, \tag{30}$$

where r and θ are the polar coordinates in the local crack tip coordinate system. When a

node would be enriched by both Eqs. (29) and (30) only Eq. (30) is used. In this research work the XFEM and Level Set Method (LSM) are coupled to model the discontinuities and subsequently find the trajectory of a crack due to different types of loading and boundary conditions.

3.2. Inclusion enrichment

Inclusions are inhomogeneities in a matrix with differing material properties. The modeling of inclusions requires the satisfaction of Hadamard condition, namely

$$\mathbf{F}^{+} - \mathbf{F}^{-} = \mathbf{a} \otimes \mathbf{n}^{+}, \tag{31}$$

where **F** is the deformation gradient, $\mathbf{n}^{+}$ is the outward normal to the material interface, and **a** is an arbitrary vector in the plane. Sukumar was the first to try and represent a material interface using enrichment in XFEM[19]. This enrichment took the form as follow

$$\psi(x) = \left| \sum_{I} N_I(x)\zeta_I \right|, \tag{32}$$

where ζ_I are the nodal level set values for the material interface level set function. This solution however, leads to issues with blending between the enriched and unenriched elements. To improve the convergence rate a minimization problem was formulated which improved the convergence. Moes then addressed the problem using a modified absolute value enrichment where [43]

$$\psi(x) = \sum_{I} N_I(x)|\zeta_I| - \left| \sum_{I} N_I(x)\zeta_I \right|, \tag{33}$$

This enrichment was shown to have optimal convergence. In addition, note that the enrichment function goes to zero at all nodes such that it does not need to be shifted like many other enrichment functions.

4. Principles of Level Set Method

One of the major issues in problems with moving boundaries is how to track growth or moving of those boundaries [20, 44, 45]. Level set functions and fast marching methods are two capable approaches in tracking moving internal boundaries. Level set approach is based upon the idea of representing the interface as a level set curve of a higher-dimensional function $\phi(\mathbf{x},t)$. A moving interface $\Gamma(t) \subset R^2$ can be formulated as the level set curve of a function $\phi: R^2 \times R \to R$, where

$$\Gamma(t) = \left\{ \mathbf{x} \in R^2 : \ \varphi(\mathbf{x},t) = 0 \right\}. \tag{34}$$

The Level Set Method (LSM) defines the surface of discontinuity by a signed distance function and models the evolution of the surface by a suitable evolution equation. The signed distance function is defined by a set of nodal values as Eq. (35), so no explicit representation of the crack is needed.

$$\varphi(\mathbf{x},t) = \pm \min_{\mathbf{x}_\Gamma \in \Gamma(t)} \left\| \mathbf{x} - \mathbf{x}_\Gamma \right\|, \tag{35}$$

where the sign is positive (negative) if **x** is outside (inside) the contour defined by $\Gamma(t)$ (we assume that the interface $\Gamma(t)$ is such that one can define an interior and exterior to it).the evolution of the interface is then embedded in the evolution equation for ϕ, which is given by [44]

$$\begin{aligned} &\varphi_t + F\|\nabla\varphi\| = 0, \\ &\varphi(\mathbf{x},0) \quad \text{given}, \end{aligned} \tag{36}$$

where $F(\mathbf{x},t)$ is the speed of the interface at $\Gamma(t)$ in the direction of the outward normal to the interface. The key advantages of this method are that it is computed on a fixed Eulerian mesh, handles topological changes in the interface naturally, and can easily be formulated in higher dimensions[20, 45, 46]. A schematic evolution of a given internal boundary is shown in Figure 5.

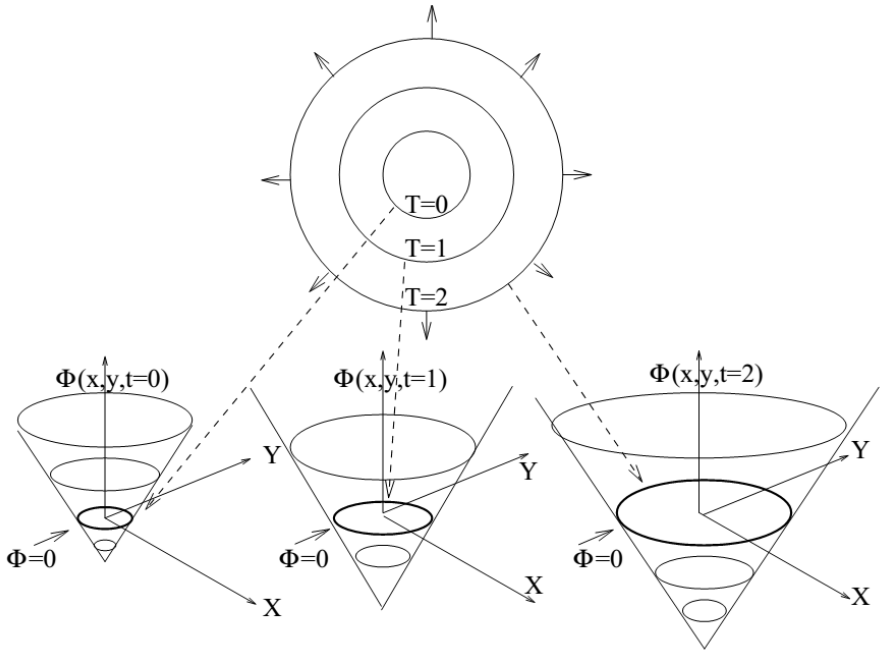


Figure 5. Transformation of front motion into initial value problem

In this study the initial crack geometry is represented by the Level Set functions in the XFEM framework, and subsequently signed distance functions are used to compute the enrichment functions that appear in the displacement-based finite element approximation. Rather than follow the interface itself, the Level Set approach instead takes the original interface and adds an extra dimension to the problem as shown in Figure 5. In fact, in the Level Set approach the height of the surface $\phi(x, y, t)$ which is defined as the z coordinate of the surface, is calculated to match the evolution of the interface in any time t. Thus to find out where the interface is at any time, cut the surface at zero height, in other words, plot the zero contour [19, 44, 47-49].

In this study by exploiting two level set functions $\phi(\mathbf{x}(t),t)$, $\psi(\mathbf{x}(t),t)$ in the XFEM framework for the crack tip and crack body respectively, the crack path is tracked. In this approach, the crack path is revealed by the zero level set of $\psi(\mathbf{x}(t),t)$. The zero level set function $\psi(\mathbf{x}(t),t)$ orientation passes from the crack tip position and oriented along the velocity function of the crack tip [50, 51].

Also it is noticeable that to speed up in the level set computations the "narrow band level set method" is used. For more information the reader can see [46]. Generally in this computational method, instead of performing calculations over the entire computational domain, an efficient modification is manipulated to perform work only in a neighborhood of the zero level set.

5. Numerical examples

In this section several models which contain crack (edge or center), inclusions and voids are studied. In the following examples different conditions of edge and center crack propagation will be evaluated. It should be noted that all examples are solved under the assumption of linear elastic behavior with small scale yielding condition. First of all, in order to establish the accuracy of calculations for stress intensity factors in mixed-mode of fracture, a comparison is done between numerical SIFs and theoretical values of counterpart.

Table **1** represents the accuracy of numerically calculated amounts of SIFs by using interaction integral in contrast with the theoretical values. It must be noted that the maximum error in obtained results according to Table 1 is 3%.

Table 1. Numerical and theoritical values of stress intensity factors in different conditions

Domain configuaration	*Crack length*	*Domain width*	K_I, *Theoritical*	K_I, *Numerical*	K_{II}, *Theoritical*	K_{II}, *Numerical*
Center crack	*1.0*	*6.0*	*1.2789*	*1.2536*	*0.0*	*-0.00008*
Center crack	*2.0*	*6.0*	*1.8915*	*1.8802*	*0.0*	*-0.0002*
Center crack	*0.25*	*20*	*0.7946*	*0.7698*	*0.0*	*-0.0002*
Center crack	*0.125*	*20*	*1.1263*	*1.1104*	*0.0*	*-0.0001*
Center crack	*0.1*	*20*	*1.2607*	*1.2475*	*0.0*	*-0.0001*
Edge crack	*0.5*	*3.0*	*1.6266*	*1.5986*	*0.0*	*-0.0005*
Edge crack	*1.0*	*3.0*	*3.1674*	*3.1687*	*0.0*	*0.0011*

5.1. Domains with a Center-crack (CC)

In these examples a plate with a center crack are considered. In order to investigate the influences of loading conditions on the crack path, different types of loading are exerted on the boundary. Uniaxial tension, shear and mixed mode of loading are studied. In the first example a predefined horizontal center crack with the length of 0.5 in a 3×6 plate under uniaxial tension is modeled. In the second example a plate with a center crack under uniform shear is considered, and in the third example the mixed mode of loading is modeled. The constitutive material behavior is chosen as linear elastic with $E=210E^9$ (Pa) and $\nu = 0.3$. The models are discretized by using 91408 degrees of freedom. In addition to increase the integration accuracy around the crack tips a subtriangularization routine is used into the finite element code to refine the 4-nodequadrature's elements in the vicinity of the crack tips. The problems are solved under plane strain condition since SIFs are independent of the state of analysis.

In the first problem which is solved under given assumptions, the propagation of a horizontal center crack is simulated. As shown in Figure 6-left in the uniaxial tension the assumed crack, propagates horizontally due to the mode I predominance. However, according to the Figure 6-right which is considered under uniform shear (in positive direction) the crack path is completely different. This is arise from the facts of differences in the modes of fracture. In fact in the second example the mode II of fracture in predominance. And in the third example which is assumed under mixed-mode of loading (tension and shear) the center crack is propagating in a situation between two previous conditions. In fact the third example is the common type of hydraulic structures' failure. Because remote forces are applied on the structure due to the directional deformations (As shown in Figure 7).

It should be noted that in order to reduce the computational effort during the crack propagation only the affected part of the global stiffness matrix is updated. It is worthy to say that in all steps the candidates' elements and nodes to enriching have been chosen by the level

set functions.

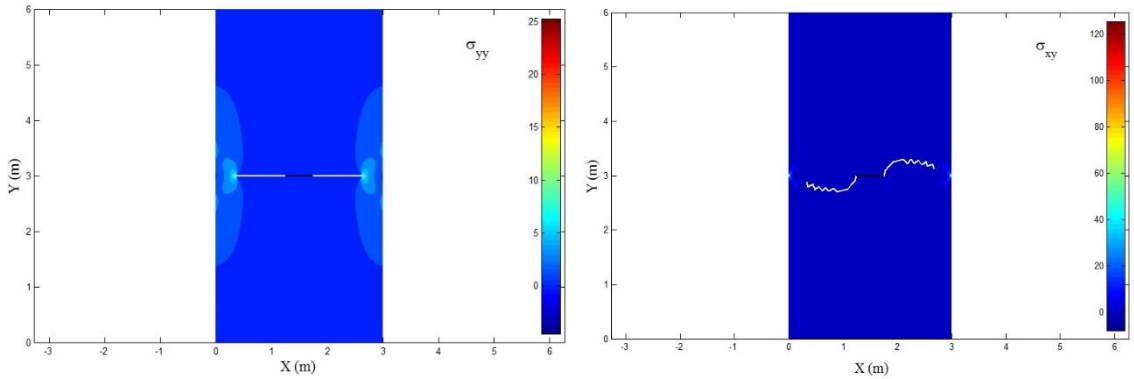


Figure 6. Center crack propagation: (left) under uniaxial tension, (right) uniform shear

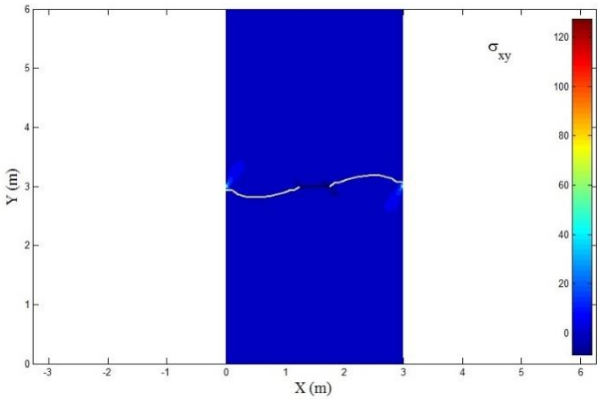


Figure 7. Mixed mode center crack propagation.

In the fourth and fifth examples of center crack propagation a 45 degrees oriented center crack under uniaxial tension and compression are modeled. Obviously these types of cracked domain is upon mixed-mode of fracture. In this problem the predicted crack growth paths are qualified by a laboratory Chalk specimen which was under simultaneous conditions. The results are shown in Figure 8. As depicted in Figure 8 both estimated and experimental crack growth paths are in the same situation. The main point in this problem is that both crack paths are going ahead perpendicular to the far faces. However, the numerical results are in the best accordance with the experimental result. In addition this minor mismatch could be due to the numerical errors. Different directions of crack propagations for an identical crack configuration in tension and compression is shown in Figure 9.

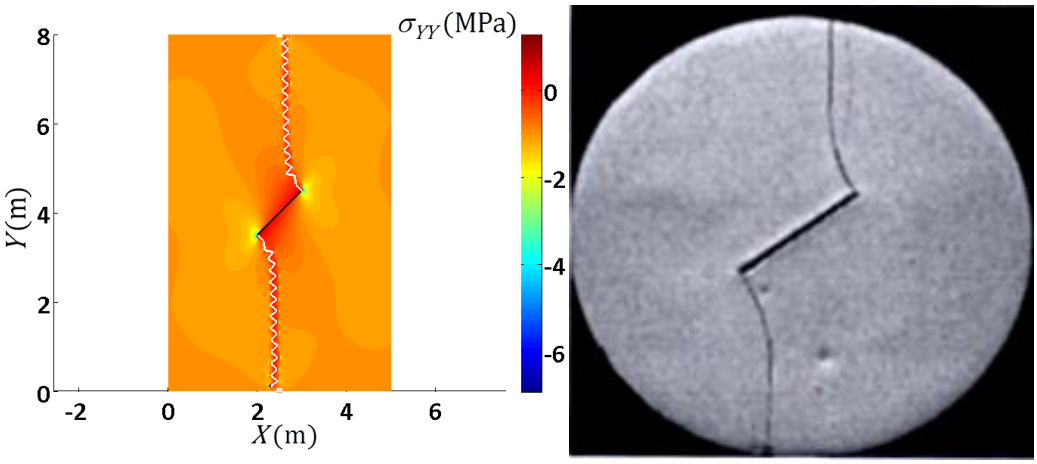


Figure 8. 45 degrees slanted center crack propagation. Numerical (left) and experimental results (right)

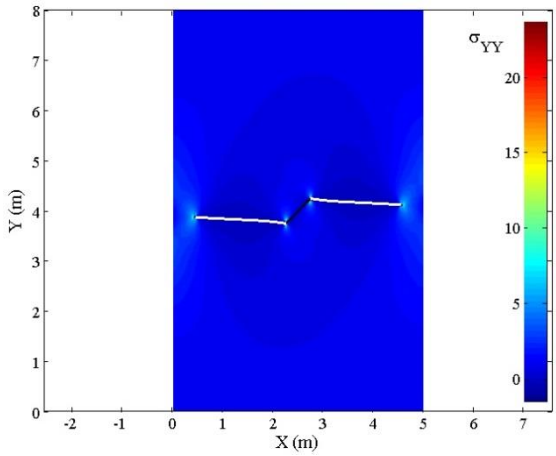


Figure 9. 45 degrees slanted center crack under tension.

Accordingly, crack propagation in dependent on the boundary conditions. As depicted in aforementioned examples, the loading condition mainly affects the stress intensity factors and finally the crack will propagate in opposite directions.

5.2. *T*-stress effects on crack propagation

In this section, the influences of considering the first non-singular term in the series expansion are studied. As if mentioned before this term participates in the shape and size of the plastic zone and finally affects the fracture initiation angle. In the following examples the crack initiation angles for the center crack with different orientations are shown. Based on the calculations for the horizontal and 45-degrees center cracks in tension, no different is achieved. In fact the crack paths for both are equal. The simulations are performed for tension and compression conditions. Figure 10 depicts the differences between fracture initiations for a 30-degrees oriented center crack for tension and compression. In other words there is a significant different in whether considering the *T*-stress effects in crack propagation or not.

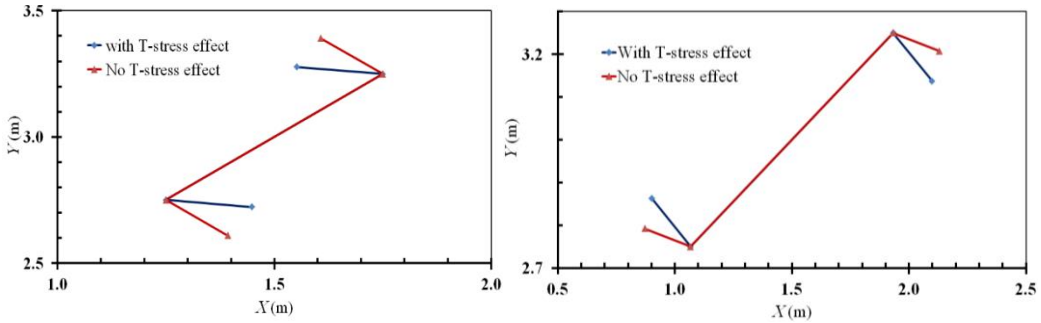


Figure 10. 30-degrees slanted center crack: under compression (left), under tension (right)

Figure 11 illustrates a 45-degrees slanted center crack propagations in tension and compression conditions. The *T*-stress effects are shown. As Figure 11 depicts, when the 45-degrees oriented center crack is under tension, no different evidence between both conditions.

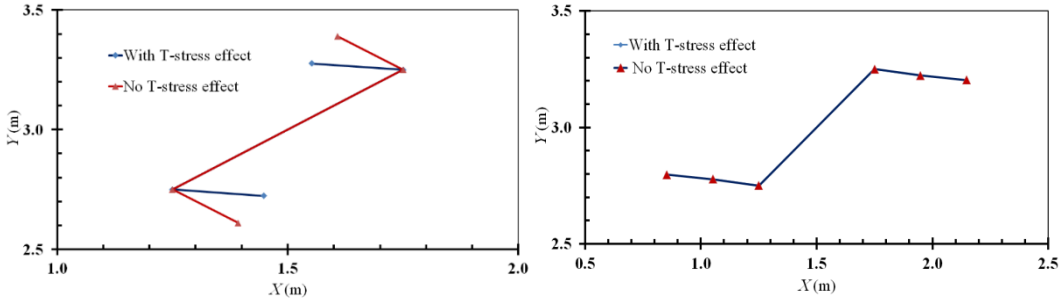


Figure 11. 45-degrees slanted center crack: under compression (left), under tension (right)

Figure 12 illustrates a 60-degrees slanted center crack propagations in tension and compression conditions. The *T*-stress effects are shown. As Figure 12 depicts, when the 60-degrees oriented center crack is under tension, the aforementioned different decreases slightly. In fact, the crack configuration changes to a horizontal condition.

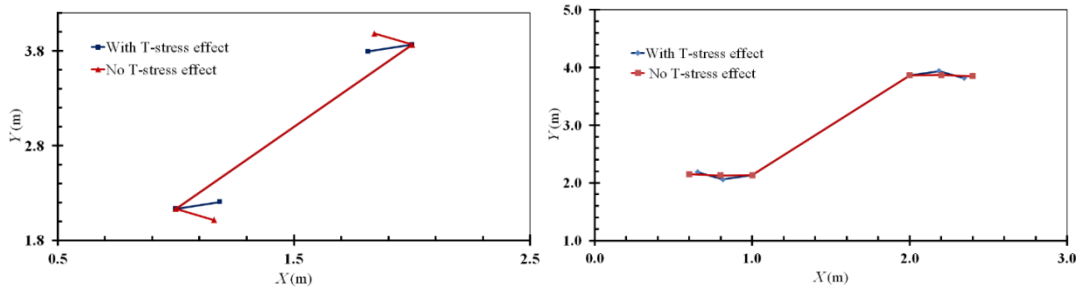


Figure 12. 60-degrees slanted center crack: under compression (left), under tension (right)

5.3. Domains with an Edge-crack (EC)

In these examples a plate with an edge crack are considered. In order to investigate the influences of loading conditions on the crack path, different types of loading are exerted on the external boundary. Uniaxial tension, shear and mixed mode of loading are studied. In the first example a predefined horizontal centered edge crack with the length of 0.5 in a 3×6 plate under uniaxial tension is modeled. In the second example a plate with an off-centered edge crack under uniaxial tension is considered. The constitutive material behavior is chosen as linear elastic with

E=210E^9 (Pa) and $\nu = 0.3$. The models are discretized by using 91022 degrees of freedom. In fact a very fine quadratic mesh is used to accurately simulate the crack propagation. In addition to increase the integration accuracy around the crack tips a subtriangularization routine is used into the finite element code to refine the 4-node quadrature's elements in the vicinity of the crack tips. The problems are solved under plane strain condition since SIFs are independent of the state of analysis. Figure 13 illustrates the stress variations in a cracked body. In fact existence a discontinuity will change the stress distribution in the domain. In addition, the stress singularity because of the crack is well shown.

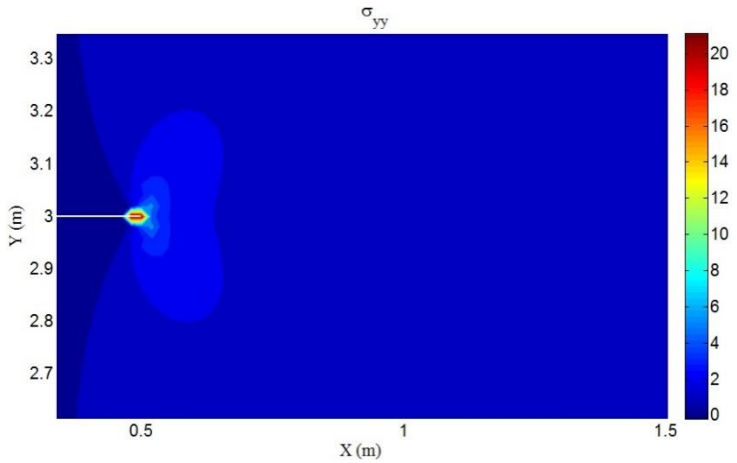


Figure 13. Stress distribution for a plate with a centered edge crack.

In the following examples the edge crack propagations under tension are simulated. First examples demonstrates the centered edge crack propagation under uniaxial tension, Figure 14-left depicts the crack path. Since uniaxial tension is applied, the crack extends horizontally in throughout the domain. However, in the second example in which an off-centered edge crack under uniaxial tension is considered. The crack propagates in a curvature path, that approaches the nearer geometrical boundary. Figure 14-right illustrates the curvature path for an off-centered edge crack.

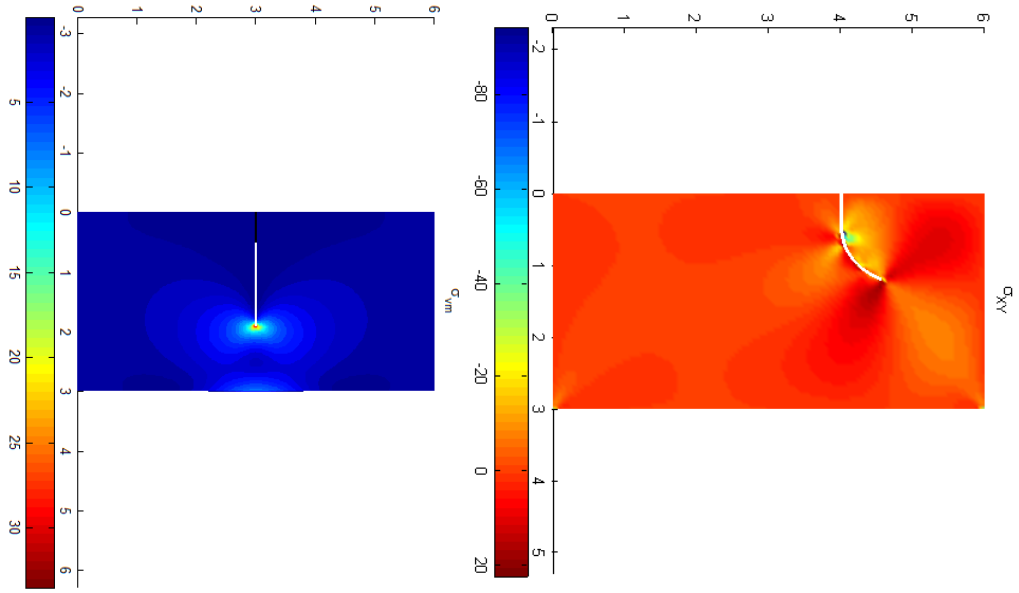


Figure 14. Edge crack propagation, centered edge crack (left), off-centered edge crack (right)

5.4. Edge-crack inclusion interaction

In this subsection the interaction between of an edge crack and both soft and hard inclusions are studied. One of the major aspects of the present study is the feasibility of modeling the different types of discontinuities simultaneously. Since presence of other discontinuities may affect the crack propagation path, therefore, the SIFs might varied due to the interactive behavior of the crack and inclusion. In fact in the crack-inclusion interaction problem there is an interface with a particular Young's modulus. When the Young's modulus of the interface is more than the Young's modulus of the material of the matrix, hard inclusion is exist and vice versa.

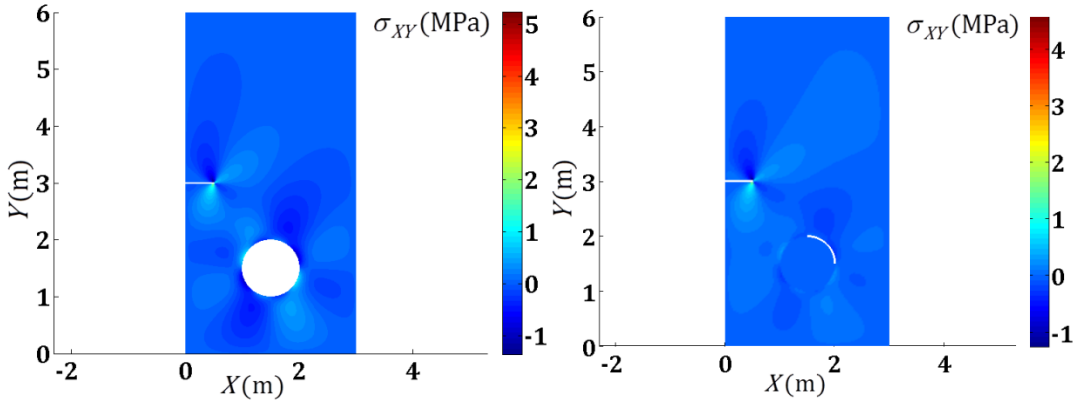


Figure 15 demonstrates the influences of the void\inclusion-crack interactions. As it shown and in the comparison with the Figure 13 the values of stresses due to the different discontinuities are affected. Table 2 shows the interactive stress intensity factors with different inclusions. In fact, the existence of the softer inclusions may change the SIFs to be greater than stiffer inclusions. Because the stresses magnify in the vicinity of the crack tips. Results are shown for a 0.5 edge crack length under uniaxial tension. Furthermore, the inclusion's diameter is chosen as 1.0. According to the numerical results, the horizontal edge crack propagation in the

interaction with the internal inclusions, is changed into the mixed-mode conditions. Since, crack-inclusion interaction mainly affects the mode II stress intensity factors. Therefore, the fracture initiations are not in the horizontal directions.

Table 2. The comparison between SIFs in the interaction with internal inclusions.

Domain configuaration	*Crack length*	K_I	K_{II}
No inclusion	*0.5*	*1.6239*	*-4.53E-8*
Crack with soft inclusion	*0.5*	*1.7483*	*0.0335*
Crack with hard inclusion	*0.5*	*1.5443*	*-0.0212*
Crack with void	*0.5*	*1.9839*	*0.1009*

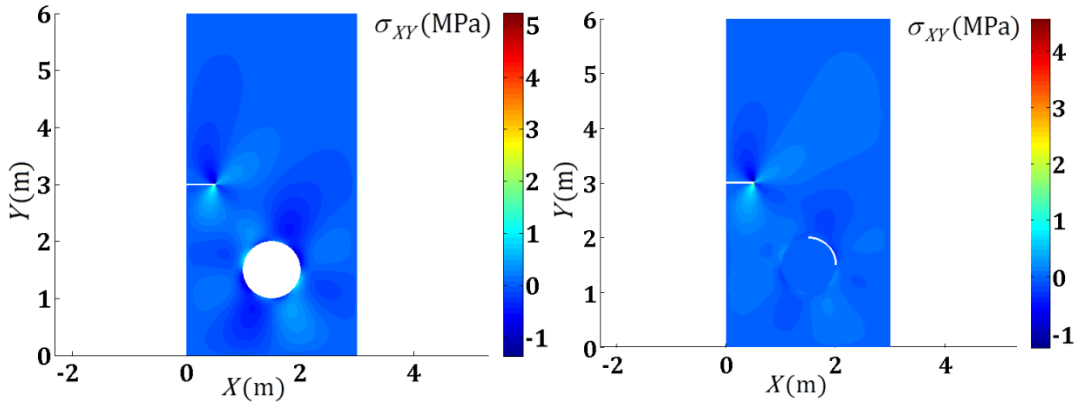


Figure 15. Crack-inclusion interaction problem: void-crack (left figure), and crack-inclusion (right figure)

One observes that, in the case of predefined cracked body with an interface as a hard inclusion the crack propagation path is moving away from the inclusion. This result may be very important in engineering design and crack propagation prediction in structural elements. In contrast, when there is a soft inclusion in the interaction with the crack, the soft inclusion attract the crack and the crack moves toward the soft inclusion.

6. Conclusion

The combination of the extended finite element method by the level set approach was performed to discontinuity modeling and evolutions of internal discontinuous boundaries. In the extended finite element framework all types of discontinuities were conformed implicitly on the finite element domain, therefore the interactions between different discontinuities were calculated. Edge and center cracks, inclusions (soft or hard internal boundaries) and voids were created implicitly and any evolutions were taken into account by the level set definitions. All procedures were numerically implemented in the finite element computer code to perform all calculations automatically. Subtriangularization was utilized to increase the accuracy of the numerical integration in the vicinity of the crack tips. The effects of soft or hard inclusions on the stress intensity factors and subsequently on the fracture initiation were demonstrated. Differences between maximum tangential stress (MTS) criterion and generalized MTS (GMTS) criterion were explained. In fact there were appreciable differences between crack initiations

with considering the effects of the first non-singular term of series expansion. It was shown that no different has occurred in the fracture initiation for a horizontal and 45-degrees slanted cracks under uniaxial tension.The computational values of the mixed-mode stress intensity factors are numerically calculated using dual form of *J*-integral and the values were in good accordance with the theoretical counterparts.

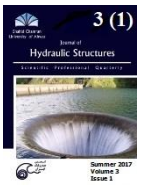
7. References

1. Sharma H D (1991) Embankment dams. New Delhi, Oxford & IBH Pub.
2. Giner E, Sukumar N, Tarancón J E, Fuenmayor F J. (2009). An Abaqus implementation of the extended finite element method. Engineering Fracture Mechanics, 76(3), 347-368.
3. Sukumar N, Prévost J H. (2003). Modeling quasi-static crack growth with the extended finite element method Part I: Computer implementation. International Journal of Solids and Structures, 40(26), 7513-7537.
4. Belytschko T, Black T. (1999). Elastic crack growth in finite elements with minimal remeshing. International Journal for Numerical Methods in Engineering, 45(5), 601-620.
5. Portela A, Aliabadi M H, Rooke D P. (1993). Dual boundary element incremental analysis of crack propagation. Computers & Structures, 46(2), 237-247.
6. Matvienko Y G, Pochinkov R A. (2013). Effect of nonsingular T-stress components on the plastic-deformation zones near the tip of a mode I crack. Russian Metallurgy (Metally), 2013(4), 262-271.
7. Sobotka J C, Dodds Jr R H. (2011). T-stress effects on steady crack growth in a thin, ductile plate under small-scale yielding conditions: Three-dimensional modeling. Engineering Fracture Mechanics, 78(6), 1182-1200.
8. Sutradhar A, Paulino G H. (2004). Symmetric Galerkin boundary element computation of T-stress and stress intensity factors for mixed-mode cracks by the interaction integral method. Engineering Analysis with Boundary Elements, 28(11), 1335-1350.
9. Kim J-H, Paulino G H. (2003). T-stress, mixed-mode stress intensity factors, and crack initiation angles in functionally graded materials: a unified approach using the interaction integral method. Computer Methods in Applied Mechanics and Engineering, 192(11–12), 1463-1494.
10. Smith D J, Ayatollahi M R, Pavier M J. (2001). The role of T-stress in brittle fracture for linear elastic materials under mixed-mode loading. Fatigue and Fracture of Engineering Materials and Structures, 24(2), 137-150.
11. Zhuang Z, Liu Z, Cheng B, Liao J, (2014) Chapter 2 - Fundamental Linear Elastic Fracture Mechanics.In: Zhuang Z, Liu Z, Cheng B, Liao J, editors. Extended Finite Element Method. Oxford: Academic Press, pp. 13-31.
12. Zehnder A T (2012) Fracture Mechanics. Springer.
13. Gdoutos E E (2005) Fracture Mechanics: An Introduction. Springer.
14. Liang R Z, Rui Z C, Liang Z Y, Hong Z, *M-integral for Stress Intensity Factor Base on XFEM*, Third International Symposium on Electronic Commerce and Security Workshops, Guangzhou, China226-230, 2010.
15. De Klerk A, Visser A G, Groenwold A A. (2008). Lower and upper bound estimation of isotropic and orthotropic fracture mechanics problems using elements with rotational degrees of freedom. Communications in Numerical Methods in Engineering, 24(5), 335-353.
16. Salvadori A, Gray L J. (2007). Analytical integrations and SIFs computation in 2D fracture mechanics. International Journal for Numerical Methods in Engineering, 70(4), 445-495.
17. Tur M, Giner E, Fuenmayor F J. (2006). A contour integral method to compute the generalized stress intensity factor in complete contacts under sliding conditions. Tribology International,

39(10), 1074-1083.
18. Fleming M, Chu Y A, Moran B, Belytschko T. (1997). Enriched element-free Galerkin Methods for Crack Tip Fields. International Journal for Numerical Methods in Engineering, 40(8), 1483-1504.
19. Sukumar N, Chopp D L, Moës N, Belytschko T. (2001). Modeling holes and inclusions by level sets in the extended finite-element method. Computer Methods in Applied Mechanics and Engineering, 190(46–47), 6183-6200.
20. Daru V. (2000). Level Set Methods and Fast Marching Methods – Evolving Interfaces in Computational Geometry, Fluid Mechanics, Computer Vision, and Materials Science by J.A. Sethian (Cambridge University Press, Cambridge, UK, 1999, 2nd edition, 378 pp.) £18.95 paperback ISBN 0 521 64557 3. European Journal of Mechanics - B/Fluids, 19(4), 531-532.
21. Naderi R, Khademalrasoul A. (2015). Fully Automatic Crack Propagation Modeling in Interaction with Void and Inclusion without Remeshing Modares Mechanical Engineering, 15(7), 261-273.
22. Bordas S, Nguyen P V, Dunant C, Guidoum A, Nguyen-Dang H. (2007). An extended finite element library. International Journal for Numerical Methods in Engineering, 71(6), 703-732.
23. Sukumar N, Huang Z Y, Prévost J H, Suo Z. (2004). Partition of unity enrichment for bimaterial interface cracks. International Journal for Numerical Methods in Engineering, 59(8), 1075-1102.
24. Moës N, Belytschko T. (2002). Extended finite element method for cohesive crack growth. Engineering Fracture Mechanics, 69(7), 813-833.
25. Dolbow J, Moës N, Belytschko T. (2001). An extended finite element method for modeling crack growth with frictional contact. Computer Methods in Applied Mechanics and Engineering, 190(51–52), 6825-6846.
26. Wu C-C, Xiao Q-Z, Yagawa G. (1998). Finite element methodology for path integrals in fracture mechanics. International Journal for Numerical Methods in Engineering, 43(1), 69-91.
27. Yarema S Y. (1996). On the contribution of G. R. Irwin to fracture mechanics. Materials Science, 31(5), 617-623.
28. Sutradhar A, Paulino G, Gray L J (2008) Symmetric Galerkin Boundary Element Method. Springer Berlin Heidelberg.
29. Aliha M R M, Ayatollahi M R. (2012). Analysis of fracture initiation angle in some cracked ceramics using the generalized maximum tangential stress criterion. International Journal of Solids and Structures, 49(13), 1877-1883.
30. Sutradhar A, Paulino G H, Gray L J (2008) Symmetric Galerkin Boundary Element Method. Springer-Verlag Berlin Heidelberg.
31. Rice J R. (1968). A Path Independent Integral and the Approximate Analysis of Strain Concentration by Notches and Cracks. Journal of Applied Mechanics, 35(2), 379-386.
32. Belytschko T, Fleming M. (1999). Smoothing, enrichment and contact in the element-free Galerkin method. Computers and Structures, 71(2), 173-195.
33. Krongauz Y, Belytschko T. (1998). EFG approximation with discontinuous derivatives. International Journal for Numerical Methods in Engineering, 41(7), 1215-1233.
34. Erdogan F, Sih G C. (1963). On the Crack Extension in Plates Under Plane Loading and Transverse Shear. Journal of Basic Engineering, 85(4), 519-525.
35. Hussain M A, Pu S L, Underwood J. (1974). Strain energy release rate for a crack under combined mode I and Mode II. Fracture Analysis. ASTM STP 560).
36. Sih G C, Kipp M E. (1974). Discussion on "fracture under complex stress—The angled crack problem". International Journal of Fracture, 10(2), 261-265.
37. Shih C F, Asaro R J. (1988). Elastic-Plastic Analysis of Cracks on Bimaterial Interfaces: Part

I—Small Scale Yielding. Journal of Applied Mechanics, 55(2), 299-316.
38. Williams M L. (1957). On the stress distribution at the base of a stationary crack. ASME Journal of Applied Mechanics, 24(1), 109–114.
39. Timoshenko S, Goodier J N (1982) Theory of elasticity. 3rd edn. Auckland, McGraw-Hill.
40. Melenk J M, Babuška I. (1996). The partition of unity finite element method: Basic theory and applications. Computer Methods in Applied Mechanics and Engineering, 139(1–4), 289-314.
41. Giner E, Sukumar N, Denia F D, Fuenmayor F J. (2008). Extended finite element method for fretting fatigue crack propagation. International Journal of Solids and Structures, 45(22–23), 5675-5687.
42. Belytschko T, Krongauz Y, Organ D, Fleming M, Krysl P. (1996). Meshless methods: An overview and recent developments. Computer Methods in Applied Mechanics and Engineering, 139(1–4), 3-47.
43. Moës N, Cloirec M, Cartraud P, Remacle J F. (2003). A computational approach to handle complex microstructure geometries. Computer Methods in Applied Mechanics and Engineering, 192(28–30), 3163-3177.
44. Osher S, Sethian J A. (1988). Fronts propagating with curvature-dependent speed: algorithms based on Hamilton-Jacobi formulations. Journal of Computational Physics, 79(1), 12-49.
45. Sethian J A. (1996). A fast marching level set method for monotonically advancing fronts. Proceedings of the National Academy of Sciences, 93(4), 1591-1595.
46. Adalsteinsson D, Sethian J A. (1995). A Fast Level Set Method for Propagating Interfaces. Journal of Computational Physics, 118(2), 269-277.
47. Shi J, Chopp D, Lua J, Sukumar N, Belytschko T. (2010). Abaqus implementation of extended finite element method using a level set representation for three-dimensional fatigue crack growth and life predictions. Engineering Fracture Mechanics, 77(14), 2840-2863.
48. Sukumar N, Chopp D L, Moran B. (2003). Extended finite element method and fast marching method for three-dimensional fatigue crack propagation. Engineering Fracture Mechanics, 70(1), 29-48.
49. Chopp D L, Sukumar N. (2003). Fatigue crack propagation of multiple coplanar cracks with the coupled extended finite element/fast marching method. International Journal of Engineering Science, 41(8), 845-869.
50. Stolarska M, Chopp D L. (2003). Modeling thermal fatigue cracking in integrated circuits by level sets and the extended finite element method. International Journal of Engineering Science, 41(20), 2381-2410.
51. Stolarska M, Chopp D L, Moës N, Belytschko T. (2001). Modelling crack growth by level sets in the extended finite element method. International Journal for Numerical Methods in Engineering, 51(8), 943-960.

Journal of Hydraulic Structures
***J. Hydraul. Struct.*, 2017; 3(1):35-48**
DOI: 10.22055/jhs.2017.13282



Developing Self-adaptive Melody Search Algorithm for Optimal Operation of Multi-reservoir Systems

Seyed Mohammad Ashrafi[*1]
Seyedeh Fatemeh Ashrafi[2]
Saber Moazami[3]

Abstract

Operation of multi-reservoir systems is known as complicated and often large-scale optimization problems. The problems, because of broad search space, nonlinear relationships, correlation of several variables, as well as problem uncertainty, are difficult requiring powerful algorithms with specific capabilities to be solved. In the present study a Self-adaptive version of Melody Search algorithm is presented and applied to obtain Operating Rule Curves for multi-reservoir systems. The self-adaptive mechanism is implemented to satisfy problems constraints and perform algorithm parameters evolution going through different iterations. The research initially evaluates capability of extended algorithm using eight benchmark problems comparing other well-known metaheuristic algorithms, and verifies its effectiveness. Then, the algorithm is adopted for optimal operation of a four-reservoir system located in Karkheh river basin to properly meet agricultural requirements and to decrease the probability of major failures; and finally, the results are provided.

Keywords: Multi-reservoir operation; Melody Search Algorithm; Self-adaptive method; Operating rule curve; Demand deficit.

Received: 05 January 2017; Accepted: 22 June 2017

1. Introduction

Due to large number of decision variables, several multiple purposes, and uncertainty and risk ruling over multi-reservoir systems, these problems are considered as complex difficult problems of planning and decision-making area [1]. Since problems' coordinated operation policies are hardly found due to the problem high dimensions, they are often termed as large

[1] Department of Civil Engineering, Faculty of Engineering, Shahid Chamran University of Ahvaz, Ahvaz, Iran. **(*Corresponding author, ashrafi@scu.ac.ir)**
[2] Master graduated, Department of Irrigation and Drainage, Faculty of Water Sciences Engineering, Shahid Chamran University of Ahvaz, Ahvaz, Iran.
[3] Environmental Sciences Research Center, Department of Civil Engineering, Islamshahr Branch, Islamic Azad University, Islamshahr, Tehran, Iran.

scale problems [2]. Effective coordinated management of operating such systems implies a policy implementation leading to maximum benefits and or minimum costs for the whole system through controlling storage values and reservoir releases [3]. To attain the purpose, system operators and managers often prefer using operation rule curves based on system extant conditions. The operating rule curves are often hybrid simulation-optimization model outputs utilizing efficient search algorithms. In this case, the simulator model simulates system reaction using a particular operating rule curve; while, optimization algorithm tries to find optimal operation policy from all existing alternatives.

According to complex nature of multi-reservoir systems and regarding technical difficulties of the system management, search algorithms used in the models must be highly capable so that system simplicity assumptions are less used as much as possible and the considered system can be analyzed in much real conditions. Therefore, researchers have been always trying to find more capable efficient optimization approaches. In recent decades, different artificial intelligence-based approaches including evolutionary computation, metaheuristic algorithms, artificial neural networks, as well as fuzzy theory computation have substituted classic methods such as linear programing and dynamic programing in solving multi-reservoir management problems [4]. However, despite high-speed solution and great coordination of linear and dynamic programing approaches, respectively, in multi-reservoir operation problems; applying these approaches, due to functional constraints and computational difficulties, is neither possible nor cost-effective for any problem.

Although, using metaheuristic algorithms may never ensure attaining global optimal solutions; in practice, the algorithms have largely been succeeded in finding optimal solutions to unsolved problems through classic methods [5]. Of various metaheuristic algorithms, in the past years, genetic algorithms were widely used for reservoir optimization problem solving. Oliveira and Loucks, [1], presented an approach using a real-coded genetic algorithm to define reservoirs' optimal operation curves. Wardlaw and Sharif, [6], employed and recommended genetic algorithm for definitive optimization of reservoir system operation as an effective approach. Sharif and Wardlaw [7], also, developed GA model for multi-reservoir system optimal operation and compared the results with policies of various DP-based models. Moreover, genetic algorithm was also used in a simulation-optimization model to determine a single-reservoir minimum and maximum operating optimal curves [8]. Dariane and Momtahen, [9], benefited a typical genetic algorithm model to specify operating rule curve parameters from a single purpose multi-reservoir system. The results were compared to the results obtained from popular optimization models such as SDP and DPR.

Wang et al., [2], introduced MIGA model for optimization of Shihmen reservoir operating problem in Taiwan. Jalali et al., [10], planned monthly operation of a single purpose reservoir through using three different Ant-based algorithm formulations. Then, Kumar and Reddy [11], provided an ACO model for operation problem of a multi-purpose reservoir and investigated its capability. The model objective was to maximize hydropower generation in addition to meeting regional agricultural demands considering flood control and environmental requirements as system constraints. Besides, they proposed the so-called EMPSO modified algorithm to identify reservoirs' operation curves, too. The proposed algorithm was utilized in a single reservoir operation system in India and the obtained results were compared with results of PSO and GA standard algorithms [12]. To acquire optimal operation policy leading to maximum energy production in successive reservoirs, Fu et al., [13], introduced a hybrid metaheuristic algorithm called IA-PSO and applied it for Qingjiang River basin system planning. Ostadrahimi et al., [14], presented a hybrid method determining optimal operation system parameters for a three-

reservoir system through using a multi-swarm optimization algorithm, MSPSO, and the popular simulator model HEC-ResPRM.

Fang et al., [15], proposed joint operating rules including; water diversion rule, hedging rule, and storage allocation rule to optimal operate of a multi-reservoir system. The predefined rules determined the amount of diverted water in a current period, the total release from the system, and the reservoirs' releases, respectively. A modified version of Particle Swarm Optimization (PSO) algorithm implemented within a simulation-optimization approach to optimize the key points of the water diversion curves, the hedging rule curves, and the target storage curves. Ashrafi, [16], applied an Efficient Adaptive version of Melody Search (EAMS) algorithm to find optimal operation policy of multi-reservoir systems. EAMS was adopted within a simulation-optimization framework to derive optimal operating rule curves for a multi-reservoir system in Iran. The obtained results showed the superiority of the developed approach in comparison with other conventional methods. A combined water and hydropower operating rule was introduced by Zhou et al., [17], to enhance the efficiency of multi-reservoir system operation. Three modules formed the main framework. A deterministic module derived the optimal reservoir storage policy a fitting module determined the optimal releases of the reservoirs and finally, a testing module was utilized to test the derived operating rules with observed inflows. Ashrafi and Dariane, [18], proposed Coupled Operating Rules (COR) to optimally operate multi-reservoir systems with distributed local demands. They defined some decision points within the considered system and suggested application of two types of linear rules to determine total releases and local water allocations in decision points. The main objective of the study was reducing the intensity of the local demand shortages throughout the system. The proposed algorithm was more effective in achieving precise solutions over a long-term period, compared to other conventional algorithms. Ak et al., [19], developed a non-linear programming model to obtain optimal operating policies for hydropower plants in single-reservoir systems. Maximization of the average annual energy generation was assumed as the main objective of the study where the short term electricity price variations were considered and be incorporated into the long-term plan.

Bozorg-Haddad et al., [20], applied conflict resolution methods to extract compromise solutions for water resources management problems. The Genetic Programing approach was utilized to calculate monthly, real-time, water allocation rule curves regarding the urban-industrial, agricultural, and environmental water uses downstream of the Zarrineh-roud River basin. Despite many studies conducted on the area of multi-reservoir systems operation optimization, scholars are still determined to come across algorithms and solutions leading to better solutions with cost-effective computational expenses. The present paper has attempted to extract an optimal operation policy from a four-reservoir system with scattered requirements through establishing a new powerful Self-adaptive Melody Search (SaMeS) optimization algorithm. The problem purpose is to properly supply agricultural demands in the whole system and to enhance reliability and decrease system failures.

Melody Search (MeS) algorithm was initially introduced by Ashrafi and Dariane, [21], and applied as a modified version of Harmony Search (HS) algorithm for a multipurpose single reservoir system operation optimization [22], where its efficiency was verified comparing other conventional methods. The proposed metaheuristic algorithm was expanded more effectively to solve continuous numerical and real-word optimization problems [23]. Although the MeS algorithm was proposed as a novel effective version of HS, the computational structure of the algorithms differed substantially. The basic HS performs weakly in exploitation process, especially in broad solution space [24] while, MeS algorithm could improve the weakness.

Generally, MeS is more powerful in solving continuous problems with broad search space and high dimensions than other variants of HS. The algorithm was later explained in more details by scholars and more extensive experiments were carried out through introducing an adaptive version of MeS [25]. Most recently, the MeS algorithm was adopted in different researches as a powerful optimization algorithm to prove the capabilities of innovative metaheuristic methods (e.g. [26]; [27]; [28]). Moreover, some novel hybrid optimization algorithms were introduced based on the MeS algorithm to solve different real-word engineering problems efficiently (e.g. [29]; [30]).

2. Multi-reservoir system operation

The research objective is achieving an optimal operation policy of a four-reservoir system located in Karkheh River basin for a long-term period (47 years). Karkheh River, situated in southwest, carries the third volume of water in Iran and is critical respecting surface water resources. Understudied system includes four reservoirs of Sazbon, Tang mashoureh, Pa Alam and Karkheh (which are schematically shown in Figure 1 as Reservoir 1 to 4, respectively), and four agricultural areas. Figure 1 schematically shows the system. System main purposes are agricultural land development, region flood control, as well as supplying environmental requirements. The modelled agricultural demands at Karkheh reservoir downstream is considered as total agricultural needs of Dasht-e Abbas, Avan, Dousalgh, Arayez, Bagheh, and lower Karkheh area.

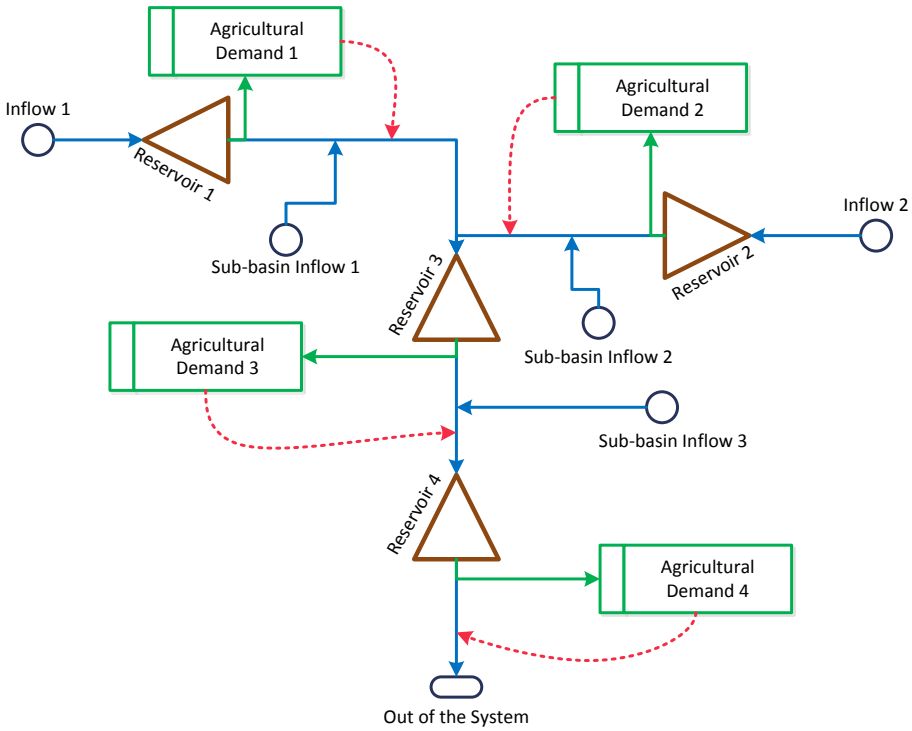


Figure 1. Schematic illustration of considered multi-reservoir system

Modeling regarded four points, in system, for controlling minimum environmental flow of the river at various periods. System agricultural Demands and reservoirs' characteristics are summarized in Table 1.

Table 1. Characteristics of reservoirs and agricultural demands

Reservoir:	1	2	3	4
Total Storage Capacity (mcm)	1608	950	3127	7600
Dead Storage Capacity (mcm)	957	352	1842	433
Active Storage Capacity (mcm)	650	598	1285	7167
Average Annual Net Evaporation (mm)	1334	1252	1580	2079
Annual agricultural demand				
Agricultural area:	1	2	3	4
Annual Demand (mcm)	400	300	307	3700

Distributed multiple demand areas and how they are localized in the system have made a complicated problem, optimization of which requires using a capable and adaptable optimization method.

3. Optimization problem

Meeting environmental requirements and agricultural demands were considered as system main objectives for modeling. In this context, environmental requirements at different river tributaries were modeled as the model constraints and meeting agricultural demands as problem objective function. As a result, the problem objective function to minimize shortage values of agricultural areas in a long-term period is assumed as follows.

$$Min\ OF = \sum_{t=1}^{T}\sum_{j=1}^{n_D}\left(\frac{TD_{t,j} - RD_{t,j}}{TD_{t,j}}\right)^2 \quad \textbf{(1)}$$

Where, $TD_{t,j}$ and $RD_{t,j}$ stand for demand and release to j^{th} agricultural area in t^{th} time period, respectively. The n_D indicates total number of agricultural areas and T is the last period of time horizon. The advantage of applying this particular form of objective function is that it tries to equally distribute system deficiencies, as much as possible, depending on the amount of defined demand in different regions and at different periods. Model constraints including mass continuity equation in reservoirs, reservoir storage limits, flow rate limits for meeting agricultural demands, limits of minimum flows at river various tributaries and final storage constraints are defined as follows:

$$S_{t+1,j} = S_{t,j} + Inflow_{t,j} - RR_{t,j} - RD_{t,j} - Eva_{t,j} - Spill_{t,j} \qquad for: \begin{cases} t = 1,2,...,T \\ j = 1,2,...,n_R \end{cases} \quad \textbf{(2)}$$

$$S\min_j \le S_{t,j} \le S\max_j \qquad for: \begin{cases} t = 1,2,...,T \\ j = 1,2,...,n_R \end{cases} \quad \textbf{(3)}$$

$$0 \le RD_{t,j} \le TD_{t,j} \qquad for: \begin{cases} t = 1,2,...,T \\ j = 1,2,...,n_D \end{cases} \quad \textbf{(4)}$$

$$RR_{t,j} \ge MFR_{t,j} \quad \textbf{(5)}$$

$$S_{1,j} = S_{T+1,j} \quad \textbf{(6)}$$

Where, $S_{t,j}$ is the beginning storage of ith reservoir in month t, $RR_{t,j}$ is the water release from jth reservoir in month t, to downstream area, $RD_{t,j}$ indecates the amount of released water from

jth reservoir in month t, for satisfying local agriculture demand. $Inflow_{t,j}$, $Eva_{t,j}$, $Spill_{t,j}$ are the amount of total inflows, net evaporation loss and amount of spilled water for j^{th} reservoir during t^{th} time period, respectively. $Smin_j$ and $Smax_j$ are minimum and maximum storage volumes for the j^{th} reservoir, respectively, and $MFR_{t,j}$ is the minimum flow requirement in month t downstream j^{th} reservoir.

4. The proposed optimization algorithm

In the present study a modified version of Melody Search algorithm is proposed to find optimal operating rule curves of multi-reservoir systems. In order to enhance the MeS algorithm ability in a long-term multi-reservoir system optimization, a Self-adaptive adjusted scheme is implemented requiring no predetermined algorithm parameter values. Despite the obvious superiority of MeS algorithm to HS and other its variants, the algorithm suffers from large numbers of parameters. Number of algorithm parameters is decreased in the new released versions of MeS and the accuracy is intensified [25]. To increase algorithm efficiency, three parallel linear equations are applied in Player Memory Consideration (PMC) operator of the proposed algorithm (SaMeS). These equations determine the variables value for new melody improvisation in each memory, as follows:

$$X^{k}_{i,new} = X^{k}_{i,L} \pm rand() \times bw(k) \quad where\ L \in U(1, \ldots, PMS) \tag{7}$$

$$X^{k}_{i,new} = X^{h}_{i,L} \pm rand() \times bw(k) \quad where\ L \in U(1, \ldots, PMS)\ and\ h \in U(1, \ldots, D) \tag{8}$$

$$X^{k}_{i,new} = X^{k}_{g,best} \quad where\ g \in U(1, \ldots, PMN)\ and\ best:\ the\ best\ melody\ form\ the\ specified\ PM \tag{9}$$

To obtain the current variable value, for the first equation, a linear relationship is set with one of corresponding variables selected from the player memory. Respecting the second equation, the linear relationship is established with a non-corresponding variable randomly selected from the extant melody variables in memory. Value of the considered variable, in the third equation, equals corresponding variables in the best existing melody in one of the memories. Aforementioned relationships are utilized relying on how well they succeeded in producing top melodies through using success rate parameter (SP_α). At onset, success rate value is assumed equal for all three relationships; then, it is measured and upgraded following a series of given iterations (Lp) based upon produced top melodies.

Algorithm 1. Determining the possible variable ranges

For *each* $k \in [1, \ldots, D]$ ***do***

$LB_k = min\ (x^{k}_{i,best},\ i=1, \ldots, PMN) - [max\ (x^{k}_{i,best},\ i=1, \ldots, PMN) - x^{k}_{Group\text{-}Best}]$

$UB_k = max\ (x^{k}_{i,best},\ i=1, \ldots, PMN) + [x^{k}_{Group\text{-}Best} - min\ (x^{k}_{i,best},\ i=1, \ldots, PMN)]$

Done

Parameter values of Player Memory Consideration Rate ($PMCR$), Pitch Adjusting Rate (PAR), and Bandwidth Distance (bw) for each top melody successfully entered memory are stored; and mean values, at a given number of iteration, are recognized as the relevant parameter values for further iterations.

The calculation of random possible variable ranges in the proposed algorithm are demonstrated in Algorithm 1 where, *best* subscript indicates the best found solution in each melody memory, $x^{k}_{i,best}$ is the k^{th} variable of the best solution stored in i^{th} memory, *Group-Best*

subscript stands for the best found solution throughout all memories, and $x^{k}_{Group\text{-}Best}$ is the kth variable of the Global-Best solution. Hence, the permissible search space for randomization is symmetrically determined around the Global-Best solution of Melody Memory (MM) in each iteration. Figure 2 represents the flowchart of the proposed algorithm for solving constrained multi-reservoir optimization problem.

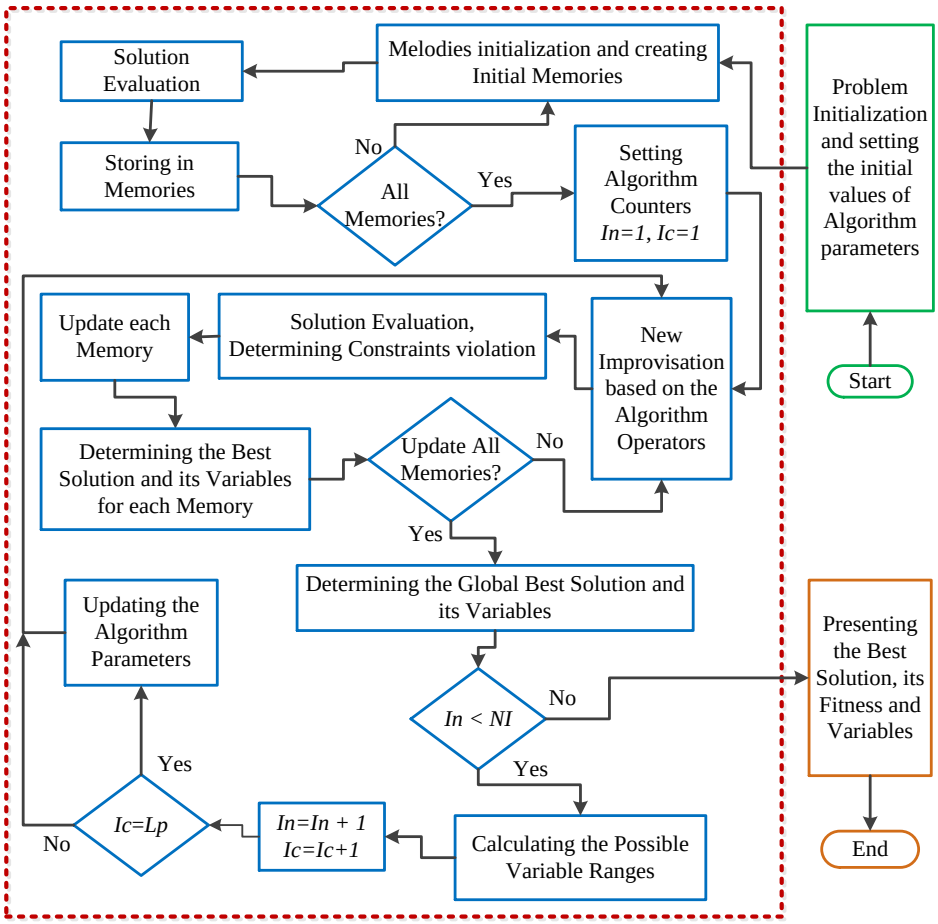


Figure 2. Flowchart of the proposed SaMeS algorithm

The values of the algorithm parameters (e.g. *PMCR*, *PAR*, *bw*) are randomly determined at the initial iteration of the algorithm. The values of parameters are improved going through different iterations based on a predefined adaptive mechanism. For more details about the parameter estimation, [25] is referred. The self-adaptive mechanism implemented in SaMeS, identifies better solutions according to the problem constraints violation. Consequently, infeasible solutions would be omitted from the memories going through different iterations. To specify the proposed algorithm capability, algorithm performance is investigated solving eight benchmark problems in continuous space compared to the performance of three popular optimization algorithms and basic-HS and basic version of MeS algorithms. The results are reported in Table 2. According to the obtained results, each algorithm statistical parameters of 30 independent executions are shown.

Table 2. Results for problems with 50 dimensions (*D*=50) and *NoFE*=50,000

		SaDE	ABC/best	GA-PSO	basic HS	basic MeS	SaMeS
Mean	Sphere	5.94E-13	2.46E-05	3.53E-10	5.31E+02	7.26E-16	**0.00E+00**
Std.		4.02E-13	6.78E-06	2.63E-10	1.23E+02	2.07E-16	**0.00E+00**
Success Rate		0.00%	0.00%	0.00%	0.00%	0.00%	100.00%
Worst		1.53E-12	1.67E-03	7.28E-10	8.47E+02	1.11E-15	0.00E+00
Best		8.22E-14	9.78E-06	5.19E-15	2.95E+02	3.09E-16	0.00E+00
Mean	Step	6.09E-13	1.39E-11	2.20E-12	5.25E+02	1.99E-02	**0.00E+00**
Std.		3.62E-13	6.13E-12	1.44E-12	8.87E+01	8.92E-02	**0.00E+00**
Success Rate		0.00%	0.00%	0.00%	0.00%	0.00%	100.00%
Worst		1.53E-12	2.35E-11	4.55E-12	6.59E+02	3.99E-01	0.00E+00
Best		8.07E-14	1.79E-13	8.44E-14	3.56E+02	9.75E-09	0.00E+00
Mean	Shifted Sphere	8.89E-12	5.63E+00	5.16E+01	5.68E+02	1.63E+04	**6.55E-28**
Std.		9.07E-12	2.07E+00	2.01E+01	1.29E+02	1.95E+03	**9.99E-27**
Success Rate		0.00%	0.00%	0.00%	0.00%	0.00%	15.00%
Worst		3.99E-11	9.28E+00	8.67E+01	8.15E+02	1.96E+04	2.75E-21
Best		1.34E-12	2.39E+00	2.22E+01	3.20E+02	1.24E+04	0.00E+00
Mean	Shifted Rosenbrock	1.75E+02	1.65E+03	4.68E+02	2.38E+06	1.37E+09	**1.26E+02**
Std.		**1.36E+02**	3.20E+02	8.90E+01	1.13E+06	2.89E+08	2.52E+02
Success Rate		0.00%	0.00%	0.00%	0.00%	0.00%	0.00%
Worst		6.46E+02	9.88E+03	9.83E+03	6.07E+06	1.88E+09	5.83E+02
Best		4.73E+01	3.55E+02	3.57E+01	1.17E+06	8.11E+08	2.00E+01
Mean	Shifted Ackley	1.26E-01	6.13E+00	1.29E+02	5.44E+00	1.50E+01	**6.15E-16**
Std.		3.31E-01	2.61E+00	4.62E+02	3.29E-01	5.17E-01	**1.42E-17**
Success Rate		0.00%	0.00%	0.00%	0.00%	0.00%	0.00%
Worst		1.16E+00	1.02E+01	2.27E+03	6.01E+00	1.63E+01	5.92E-11
Best		2.18E-07	3.26E-01	1.06E-06	4.92E+00	1.44E+01	4.90E-20
Mean	Shifted Griewank	1.64E-03	6.92E-01	1.27E+01	6.01E+00	1.41E+02	**1.11E-19**
Std.		3.39E-03	4.19E-01	1.41E+01	1.26E+00	2.64E+01	**3.42E-19**
Success Rate		0.00%	0.00%	0.00%	0.00%	0.00%	90.00%
Worst		9.86E-03	1.32E+00	4.15E+01	7.78E+00	1.95E+02	1.11E-17
Best		2.25E-12	8.11E-04	1.14E+00	3.62E+00	8.95E+01	0.00E+00
Mean	Shifted Rotated Rastrigin	3.28E+02	9.20E+03	4.10E+03	4.71E+02	5.99E+02	**1.85E+02**
Std.		**1.83E+01**	9.00E+02	7.32E+02	4.23E+01	3.88E+01	4.45E+01
Success Rate		0.00%	0.00%	0.00%	0.00%	0.00%	0.00%
Worst		3.60E+02	1.77E+04	1.64E+04	5.38E+02	6.66E+02	5.97E+02
Best		2.91E+02	5.10E+02	1.32E+02	3.53E+02	5.24E+02	4.34E+01
Mean	Shifted Rotated Griewank	8.99E-01	1.25E+00	2.82E+02	4.07E+01	5.14E+02	**3.84E-02**
Std.		2.56E-01	5.48E-01	3.11E+02	1.21E+01	6.78E+01	**2.89E-02**
Success Rate		0.00%	0.00%	0.00%	0.00%	0.00%	0.00%
Worst		1.28E+00	1.90E+00	8.17E+02	7.71E+01	6.38E+02	9.45E-02
Best		2.17E-01	1.28E-01	1.21E+01	2.56E+01	3.42E+02	9.06E-04

Table 2 compares results of the proposed algorithm with the results of Basic-HS [31], Basic-MeS [21], SaDE algorithm [32], AB/best algorithm [33], and GA-PSO hybrid algorithm [34]. Basis functions were specified with 50 decision variables. In order to perform a firm comparison, total number of fitness evaluations (*NoFE*) is assumed as 50,000 for all algorithms, thus, the total iteration number (*NI*) is calculated for each algorithm based on its structure. As seen, the proposed algorithm attained the best solutions and outperformed other algorithms in statistical comparisons indicating algorithm capability in solving multimodal problems in high

dimensioned broad continuous search space.

5. Results

As earlier explained, a metaheuristic simulation-optimization model is developed to determine the best operation policy of a four-reservoir water resources system. Reservoirs' monthly releases are estimated according to reservoir monthly mean storage volume and predefined operating rule curves. The simulator, models system details per optimization algorithm solution and computes objective function value and problem constraints violation. Decision variables considered in optimization model determine specified reservoirs' rule curves. To eliminate non-feasible solutions, dominance feasible solutions method was applied using values of constraints violation.

Two operation rule curves are defined for each reservoir including, Upper and Lower rules. The predefined rules determine the wet, normal and dry conditions for reservoir operators. In a case that reservoir storage per given month is higher than the upper operation curve level, discharge would be equal to total local agricultural demand of the reservoir plus reservoir storage difference to the upper operation curve level. This additional volume supplies downstream reservoirs and other regional needs, when the reservoir monthly storage indicates wet condition. If reservoir storage volume is between two operation curves, reservoir release would just equal to local demands (normal condition). When reservoir storage volume is less than the lower curve, only 70% of local agricultural demand, which is not smaller than minimum environmental flow would be released (dry condition). Figure 3 illustrates mean monthly inflows and monthly demands defined in the system. As illustrated in Figure 1, return flows of agricultural areas supply downstream local demands and reservoirs, even in dry condition.

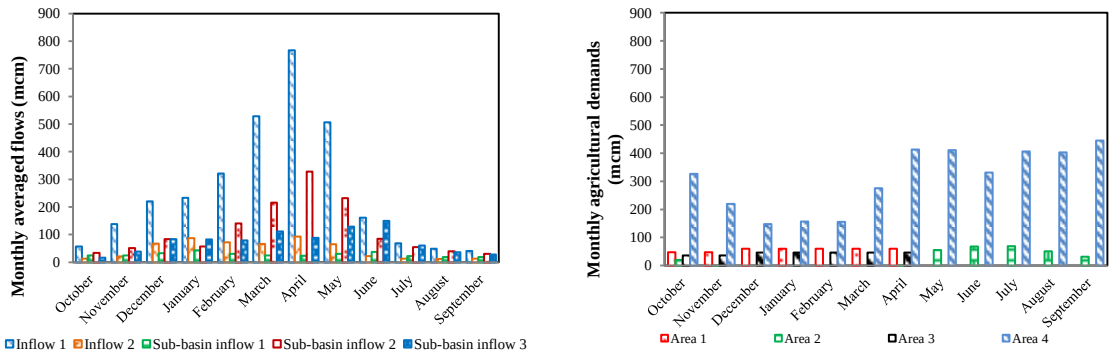


Figure 3. Averaged monthly inflows and agricultural demands

According to inflow statistics and system requirements in a long-term 47-year period, reservoirs operation rule curves are determined in a way that the lowest distributed deficiency in the whole system is obtained. To solve the considered problem, SaMeS algorithm with 5 player memories and 5 melodies in each memory was provided. Maximum iteration number for optimal solution was set 50,000. Respecting 30 independent executions, mean solutions obtained 91.04 for objective function at standard deviation 90.23. Of these, the best and worst solutions were 25.7 and 324.87, respectively for objective function revealing that the algorithm is well converged to the problem optimum solution.

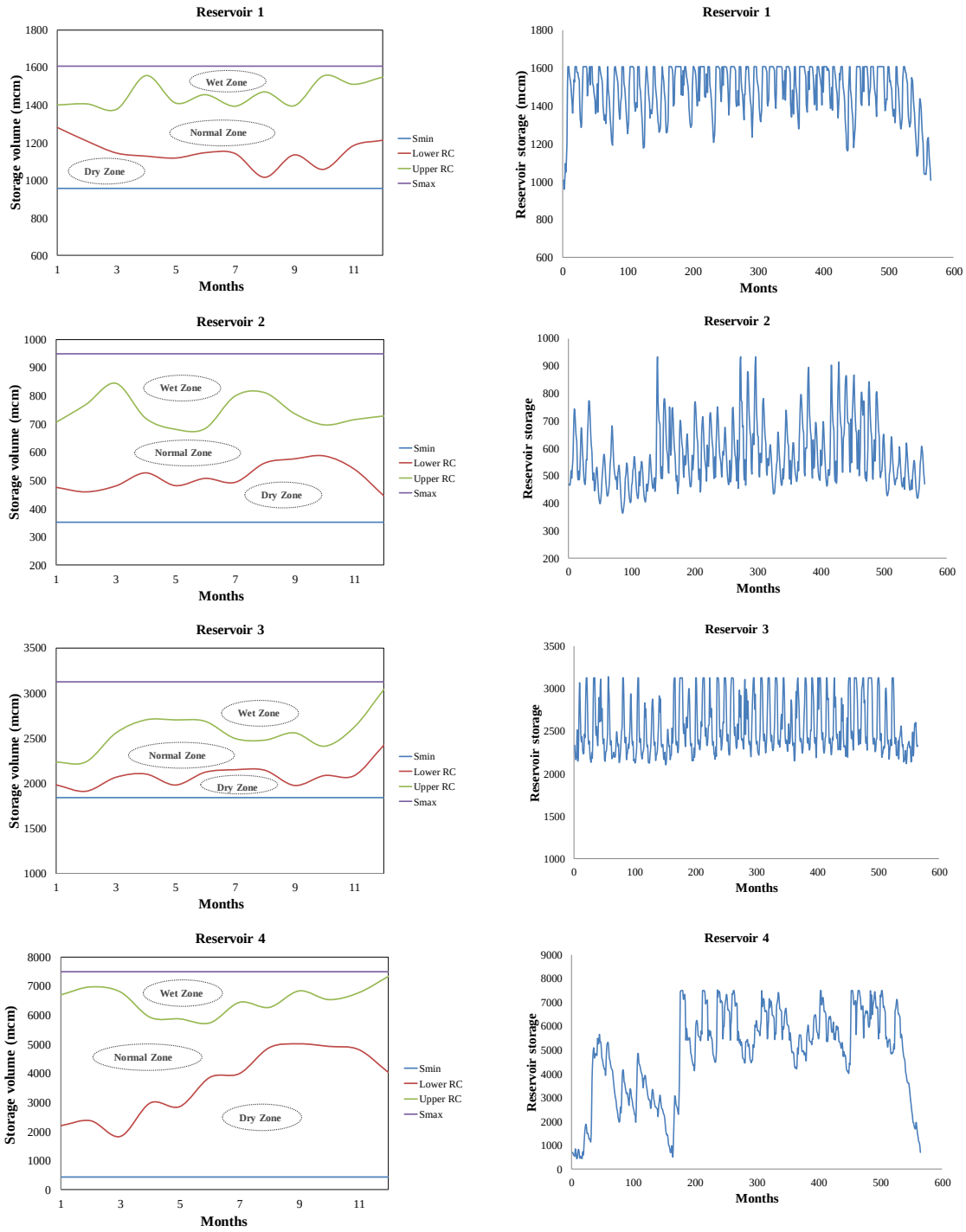


Figure 4. Operation rule curves and simulated storage variation of reservoirs

The algorithm enjoys the ability of rapid recognition of the problem feasible space to search for optimal solution. Figure 4 represents reservoirs rule curves and simulated reservoirs' storages resulted from the best obtained solution. As observed, Reservoir 2 operation curves are obtained

such that downstream released flow would be maximized in most months due to low local agricultural demands.

Moreover, Reservoir 3, which contributes as additional storage supplying downstream requirements, has rule curves tending to release flow and supply Reservoir 4. Optimal operating rule curves of Reservoir 2 and Reservoir 4 are set such that the maximum possible values of reservoirs volume are attributed to supply their local requirements. The results are consistent with systemic optimization concepts demonstrating optimization of operation process. Table 3 summarizes simulated results of all four reservoirs through using optimum systemic operation curves for a long-term 47-year period.

According to the achieved results related to the best solution, all demands showed approximately close quantitative reliability, which was the purpose sought for in the model objective function definition. Thus, the model tries to distribute the deficits for different periods respecting basin requirements and to prevent great failures; while, demands time reliability was different. Moreover, it is observed that Reservoir 3 plays the supportive role for Reservoir 4; further, it was full overflowing during the long-term period supplying downstream demands. The reservoir empty percentage is zero.

Table 3. Results of system simulation using the best obtained rules

	Reservoirs			
Parameters	1	2	3	4
Annual Evaporation (mcm)	37.8	30.3	28.3	136.3
Annual Spill (mcm)	1830	260	3482	104.0
Time percent of Emptiness	31.5%	78.0%	82.0%	13.7%
Time percent of being full	0.5%	1.8%	0.0%	53.2%
	Agricultural Demands			
Agricultural Area	Reliability		Quantitative Reliability	
1	57.4%		70.2%	
2	61.3%		78.3%	
3	62.5%		75.6%	
4	42.3%		75.9%	

On the other side, time percentage of being full for Reservoir 4, and consequently, the spill were less than other reservoirs since the reservoir spill values were inaccessible in understudied system regarded as system waste. In other word, optimization model tries to reduce wastes as much as possible to better meet system demands. Figure 5 shows the long term average monthly demand deficits and reservoir spills. It clearly shows that in the optimum solution found by the proposed SaMeS algorithm there is the lowest possible spill from Reservoir 4, the last one in the system. An optimal operating strategy must control and decrease the system losses such as spill and net evaporation. In Reservoir 2, spills mainly occur during high flow periods of February to June. Meanwhile, spills from Reservoir 2 and 3 are considered as losses but they can be used to satisfy lower demands, help the Reservoir 3 and 4 to supply their local demands and supply environmental minimum flow requirements.

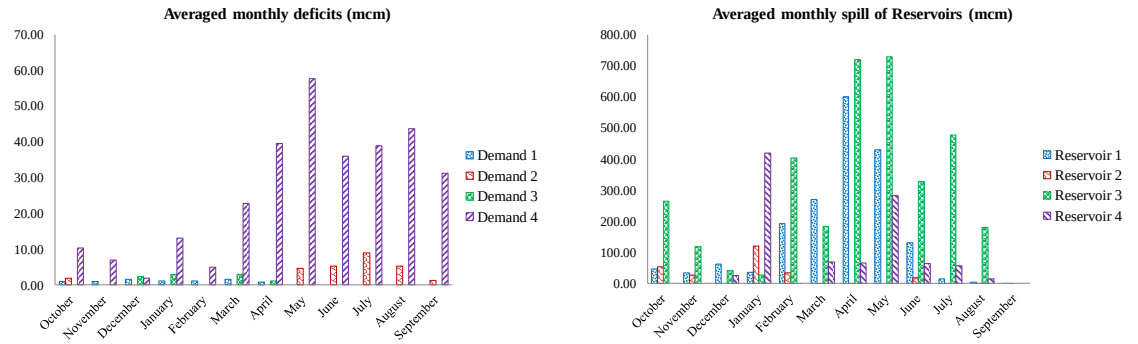


Figure 5. Averaged monthly demands' deficits and reservoirs' spills

6. Conclusion

The present research attempted to determine a four-reservoir system operation, located in Karkheh River, through developing a capable optimization-simulation model. The optimization algorithm was an improved Self-adaptive Melody Search algorithm. According to research findings, it may be concluded that the proposed algorithm is highly competent and efficient for solving complicated continuous problems in comparison to the well-known optimization algorithms. The proposed algorithm outperformed other well-known algorithms in statistical comparisons and attained the best solution. The proposed SaMeS algorithm benefits from the multi-memories structure and utilizing a self-adaptive mechanism. The cooperative rule curves for a multi-reservoir system achieved by the proposed simulation-optimization approach is able to manage the diversity of demand deficits in a long-term period. The Quantitative Reliability of different local demands are determined as close as possible where the optimal rule curves reduce the total losses of reservoirs such as spill and net evaporation. In general, each agricultural area encounters the least failure probability. This is the best policy to deal with systemic water resources problems, which would never be achieved in individual reservoir analysis.

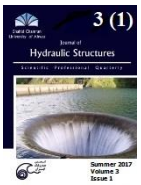
7. References

1. Oliveira R., and Loucks D.P. (1997). Operating Rules for Multi-reservoir Systems. Water Resources Res., 33, 839-852.
2. Wang KW, Chang LC, Chang FJ, (2011). Multi-tier interactive genetic algorithms for the optimization of long-term reservoir operation. Adv Water Resour; 34(10):1343-1351.
3. Mahootchi M, Ponnambalam K, Tizhoosh H. (2010). Operations optimization of multireservoir systems using storage moments equation. Adv Water Resour; 33(9):1150-1163.
4. Chaves P, Chang FJ, (2008). Intelligent reservoir operation system based on evolving artificial neural networks. Adv Water Resour; 31(6):926-936.
5. Moazami, S., Abdollahipour, A., Zakeri Niri, M., & Ashrafi, S. M. (2016). Hydrological Assessment of Daily Satellite Precipitation Products over a Basin in Iran. Journal of Hydraulic Structures, 2(2), 35-45.
6. Wardlaw R, Sharif M, (1999). Evaluation of Genetic Algorithms for Optimal Reservoir System Operation. Journal of Water Resources Planning and Management 125(1): 25-33.
7. Sharif M, Wardlaw R, (2000). Multireservoir systems optimization using genetic algorithms: Case study. J. Comput Civ Eng, 14(4): 255–263.

8. Suiadee W, Tingsanchali T, (2007). A combined simulation–genetic algorithm optimization model for optimal rule curves of a reservoir: a case study of the Nam Oon Irrigation Project, Thailand. Hydrol. Process 2007; 21(23): 3211–3225.
9. Dariane AB, Momtahen Sh, (2009), "Optimization of multireservoir systems operation using modified direct search genetic algorithm", J. Water Resour Plann Manage; 135(3): 141–148.
10. Jalali MR, Afshar A, Marino MA, (2003), "Reservoir Operation by Ant Colony Optimization Algorithms", online paper; http://www.optimizationonline.org/DB FILE/2003/07/696.pdf, (accessed on 10/12/2004).
11. Kumar D. N., Reddy M. J. (2006). Ant colony optimization for multi-purpose reservoir operation. Water Resour Manage; 20(6): 879-898.
12. Kumar D. N., Reddy M. J. (2007). Multipurpose reservoir operation using particle swarm optimization. J. Water Resour Plann Manage. 133(3): 192-201.
13. Fu X, Li A, Wang L, Ji C. (2011). Short-term scheduling of cascade reservoirs using an immune algorithm-based particle swarm optimization. Computers and Mathematics with Applications; 62 (6): 2463–2471.
14. Ostadrahimi L, Mariño MA, Afshar A, (2012). Multi-reservoir Operation Rules: Multi-swarm PSO-based Optimization Approach. Water Resour Manage; 26:407–427.
15. Fang, H. B., Hu, T. S., Zeng, X., & Wu, F. Y. (2014). Simulation-optimization model of reservoir operation based on target storage curves. Water Science and Engineering, 7(4), 433-445.
16. Ashrafi S. M. (2015). Multi-reservoir Optimal Operation using Efficient Adaptive Melody Search Algorithm (EAMS). Proceeding of 10th International Congress on Civil Engineering, University of Tabriz, Tabriz, Iran.
17. Zhou, Y., Guo, S., Liu, P., Xu, C. Y., & Zhao, X. (2016). Derivation of water and power operating rules for multi-reservoirs. Hydrological Sciences Journal, 61(2), 359-370.
18. Ashrafi, S. M., & Dariane, A. B. (2017). Coupled Operating Rules for Optimal Operation of Multi-Reservoir Systems. Water Resources Management, 31(14), 4505-4520.
19. Ak, M., Kentel, E., & Savasaneril, S. (2017). Operating policies for energy generation and revenue management in single-reservoir hydropower systems. Renewable and Sustainable Energy Reviews, 78, 1253-1261.
20. Bozorg-Haddad, O., Athari, E., Fallah-Mehdipour, E., & Loáiciga, H. A. (2017). Real-time water allocation policies calculated with bankruptcy games and genetic programing. Water Science and Technology: Water Supply, ws2017102.
21. Ashrafi, S. M., & Dariane, A. B. (2011). A novel and effective algorithm for numerical optimization: melody search (MS). In Hybrid Intelligent Systems (HIS), 2011 11th International Conference on (pp. 109-114). IEEE.
22. Ashrafi, S. M., & Dariane, A. B. (2012). Application of Improved Harmony Search Algorithm in Optimal Operation of Multi-purpose Reservoirs. Proceeding of 9th International Congress on Civil Engineering, Isfahan, Iran.
23. Ashrafi, S. M., & Dariane, A. B. (2013). Performance evaluation of an improved harmony search algorithm for numerical optimization: Melody Search (MS). Engineering applications of artificial intelligence, 26(4), 1301-1321.
24. Kourabbaslou, N. E., Ashrafi S.M., Mohaghar A. (2016). Multi-objective Supply Chain Optimization Using Harmony Search Algorithm. Proceeding of the First International Conference on Industrial Engineering and Management, Tehran University, Tehran, Iran.
25. Ashrafi, S. M., & Kourabbaslou, N. E. (2015). An Efficient Adaptive Strategy for Melody

Search Algorithm. International Journal of Applied Metaheuristic Computing (IJAMC), 6(3), 1-37.
26. Xiang, W. L., An, M. Q., Li, Y. Z., He, R. C., & Zhang, J. F. (2014). An improved global-best harmony search algorithm for faster optimization. Expert Systems with Applications, 41(13), 5788-5803.
27. Zhao, F., Liu, Y., Zhang, C., & Wang, J. (2015). A self-adaptive harmony PSO search algorithm and its performance analysis. Expert Systems with Applications, 42(21), 7436-7455.
28. Koupaei, J. A., Hosseini, S. M. M., & Ghaini, F. M. (2016). A new optimization algorithm based on chaotic maps and golden section search method. Engineering Applications of Artificial Intelligence, 50, 201-214.
29. Shivaie, M., & Ameli, M. T. (2016). Strategic multiyear transmission expansion planning under severe uncertainties by a combination of melody search algorithm and Powell heuristic method. Energy, 115, 338-352.
30. Kiani-Moghaddam, M., & Shivaie, M. (2017). An Innovative Multi-Stage Multi-Dimensional Multiple-Inhomogeneous Melody Search Algorithm: Symphony Orchestra Search. In Bio-Inspired Computing for Information Retrieval Applications (pp. 1-40). IGI Global.
31. Lee, K. S., & Geem, Z. W. (2005). A new meta-heuristic algorithm for continuous engineering optimization: harmony search theory and practice. Computer methods in applied mechanics and engineering, 194(36), 3902-3933.
32. Qin AK, Huang VL and Suganthan PN, (2009), Differential Evolution Algorithm With Strategy Adaptation for Global Numerical Optimization. IEEE transaction on evolutionary computation, Vol. 13, No. 2, April 2009, pp. 398-417.
33. Gao W., Liu S., Huang L., (2012), "A global best artificial bee colony algorithm for global optimization", Journal of Computational and Applied Mathematics 236, 2741–2753.
34. Kao YT, Zahara E, (2008), "A hybrid genetic algorithm and particle swarm optimization for multimodal functions", Applied Soft Computing 8, 849–857.

Journal of Hydraulic Structures
***J. Hydraul. Struct.*, 2017; 3(1): 49-56**
DOI: 10.22055/jhs.2017.13316



Multiobjective design of sewer networks

Amin E. Bakhshipour[1]
Yasaman Makaremi[2]
Ulrich Dittmer[3]

Abstract

The sewer layout in flat areas significantly influences the construction and operational costs as well as reliability of the network performance. To find an optimum design of sewer networks for flat areas, this study presents a multi-objective optimization problem with the objective functions of 1- the cost and 2- the reliability. The reliability criterion is defined as the effect of a clogging in a sewer on its upstream population. To solve the problem, the NSGA-II Algorithm is coupled to two self-adaptive design algorithms for generating the layout and sizing of sewers. A case study is solved using the proposed model to demonstrate its application and advantages.

Keywords: Sewer network, Layout, Reliability, Flat area, Multiobjective optimization.

Received: 14 April 2017; Accepted: 06 June 2017

1. Introduction

Constructing a new sewer system, particularly in developing countries, is a very expensive and challenging task. The design of a sewage collection network needs to solve two successive subproblems: (1) generating the layout and (2) hydraulic design of the sewers and pumps. In flat areas where there is no significant change in the ground topography, the layout configuration is determined almost independently of the natural slopes. In such areas, the number of feasible layouts exponentially increases with the number of pipes in the system (Diogo and Graveto, 2006). Moreover, in flat areas, the reliability of sewer networks is threatened by phenomena such as clogging due to sediment deposition which poses significant costs to the operating companies and public inconvenience. Haghighi and E. Bakhshipour (2015b) introduced a new criterion for designing sewer layouts based on the reliability concept. They found that the reliability seriously conflicts with the system construction cost.

Considering this issue, the present work introduces a multiobjective optimization framework

[1] University of Stuttgart, Institute for Sanitary Engineering, Water Quality and Solid Waste Management, 70569 Stuttgart, Germany, amin.ebrahim-bakhshipour@iswa.uni-stuttgart.de (**Corresponding author**)
[2] Shahid Chamran University of Ahvaz, Department of Civil Engineering, Faculty of Engineering, Ahvaz, Iran.
[3] University of Stuttgart, Institute for Sanitary Engineering, Water Quality and Solid Waste Management, 70569 Stuttgart, Germany.

for finding trade-offs between cost and reliability in the layout design of sewer networks. For this purpose, the Non-Dominated Sorting Genetic Algorithm, version II, NSGA-II (Deb et al., 2002), is coupled to two adaptive algorithms for solving the aforementioned subproblems.

2. Methods

2.1. Layout design

The first step for designing a sewage collection system is to design its layout. Creating and evaluating all possible designs is practically impossible without using a computational graph-based algorithm joined to an optimization solver. For the sewer network optimization, a layout generator model is required in order to make the procedure systematic. The layout generator model must be able to satisfy all constraints while extracting layout alternatives from an initial base graph. In this study, the "Loop-by-loop Cutting Algorithm" is adopted for this purpose. This algorithm introduced by Haghighi (2013) is an adaptive layout generator which systematically satisfies all constraints. In short, by using this algorithm, it is possible to generate feasible layouts of a network from an initially looped and undirected base graph. For each loop in the base graph, two real normal- and binary-valued variables, which respectively determine the pipe in the loop to cut and the location of the cut (from the upstream or downstream), are randomly defined. Then, through a step-by-step procedure, all loops are cut, while all constraints associated with the sewer layout are systematically satisfied. Further details on this algorithm can be found in (Haghighi, 2013).

2.2. Sewer Design

After generating a feasible sewer layout, the second sub-problem is hydraulic design, considering sewer diameters, installation depths, and pump stations. To exploit metaheuristic methods efficiently for solving the highly constrained problem of sewer design, Haghighi and E. Bakhshipour (2012) introduced a self-adaptive hydraulic design procedure. Through this approach, all hydraulic and technical constraints of the sewer design with a given layout are systematically met, and therefore, there is no need for any constraint handling in the optimization process. More details can be found in the original paper.

After integrating the two sub-problems of sewer network design into a model, two objective functions are employed to evaluate: 1- the cost and 2- the reliability of the system

2.3. Reliability-based objective function

To evaluate the clogging consequences in sewer networks, Haghighi and E. Bakhshipour (2015b) introduce the average reliability index (ARI) that only uses the layout design properties. This criterion can indirectly evaluate how well a sewer system can react to a sewage flow blockage. On this basis, the average reliability of the entire network is measured as equation (1):

$$ARI = \bar{R}_i = 1 - \frac{1}{m}\sum_{i=1}^{m} {Q_i}/{Q_{out}} \qquad (\mathbf{1})$$

in which, Q_i is the cumulative sewage discharge through pipe i, m is the number of sewers in the network, and Q_{out} is the total sewage flow of the network toward the outlet. It is also worth noting that only sewers with a reliability index less than 90% are used to calculate the ARI, which is then denoted by $ARI_{<90}$. Considering $ARI_{<90}$ instead of ARI, makes the layout configuration and its reliability more sensitive to the main collectors which convey high sewage discharges and would be more threatened by clogging. (Haghighi and E. Bakhshipour, 2015b)

2.4. Costs

In this study, the cost function introduced by Li and Matthew (1990) is employed (equation 2).

$$C = \sum_{i=1}^{m} (CP_i + P_i \times CL_i) + \sum_{i=1}^{m+1} (CM_i) \quad (2)$$

where, CP is the construction cost of sewers, CL is the construction cost of the pumps and CM is the construction cost of manholes based on the data presented in Tab. 1. Also, P_i is the pump parameter which is 1 when there is a lift station at the upstream end of the pipe and is 0 otherwise. The construction cost is estimated as a function of sewer diameters D, sewer lengths L, installation depths H and the pump specifications.

Table 1. The cost function of the example in Yuan (Li and Matthew 1990).

CP (Sewer cost)	
$(4.27 + 93.59D^2 + 2.86D \times H + 2.39H^2) \times L$	$D \leq 1$m, $H \leq 3$m
$(36.47 + 88.96D^2 + 8.70D \times H + 1.78H^2) \times L$	$D \leq 1$m, $H > 3$m
$(20.50 + 149.27D^2 - 58.96D \times H + 17.75H^2) \times L$	$D > 1$m, $H \leq 4$m
$(78.44 + 29.25D^2 + 31.80D \times H - 2.32H^2) \times L$	$D > 1$m, $H > 4$m
CM (Manhole cost)	
$136.67 + 166.19D^2 + 3.50D \times H + 16.22H^2$	$D \leq 1$m, $H \leq 3$m
$132.67 + 790.94D^2 - 280.23D \times H + 34.97H^2$	$D \leq 1$m, $H > 3$m
$209.04 + 57.53D^2 + 10.93D \times H + 19.88H^2$	$D > 1$m, $H \leq 4$m
$210.66\text{-}113.04D^2 + 126.43D \times H - 0.60H^2$	$D > 1$m, $H > 4$m
CL (Pump cost)	
$270{,}021 + 316.42Q - 0.1663Q^2$	Q (l/s)

2.5. Optimization method

The metaheuristic method of NSGA-II was applied to derive the trade-off between costs and reliability. For sizing the sewers 24 commercially available diameters ranging from 0.2 to 2.40 meters were considered. The design constraints including the limits of velocities, slopes, proportional water depth and the required cover depth. Fig 1 shows a flow chart of the multiobjective optimization procedure.

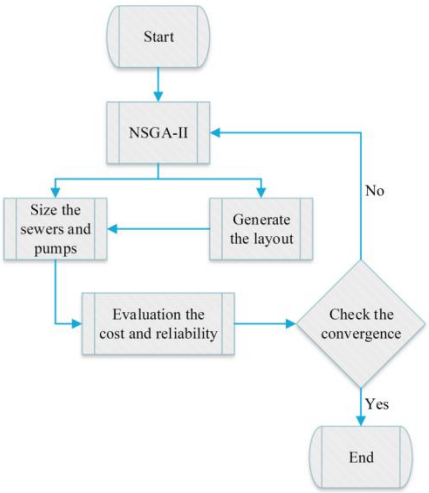


Figure 1. The multiobjective optimization framework for sewer networks design

3. Results and discussions

Fig. 2 shows the base graph used to test the procedure. It was originally developed by Li and Matthew (1990) as a benchmark example for optimization. The sewer network collects a 260-hectare residential area with a flat topography. The base graph has 79 pipes, 57 main manholes and 23 loops and its outlet is manhole 56 connected to sewer 59. Additional information on the network is also found in Li and Matthew (1990).

The loop by loop cutting algorithm and the adaptive algorithm are applied to sequentially generate a feasible layout and design it hydraulically. The model is coupled with the metaheuristic method of NSGA-II to maximize the reliability of the network based on the proposed criterion $ARI_{<90}$ and minimize the cost.

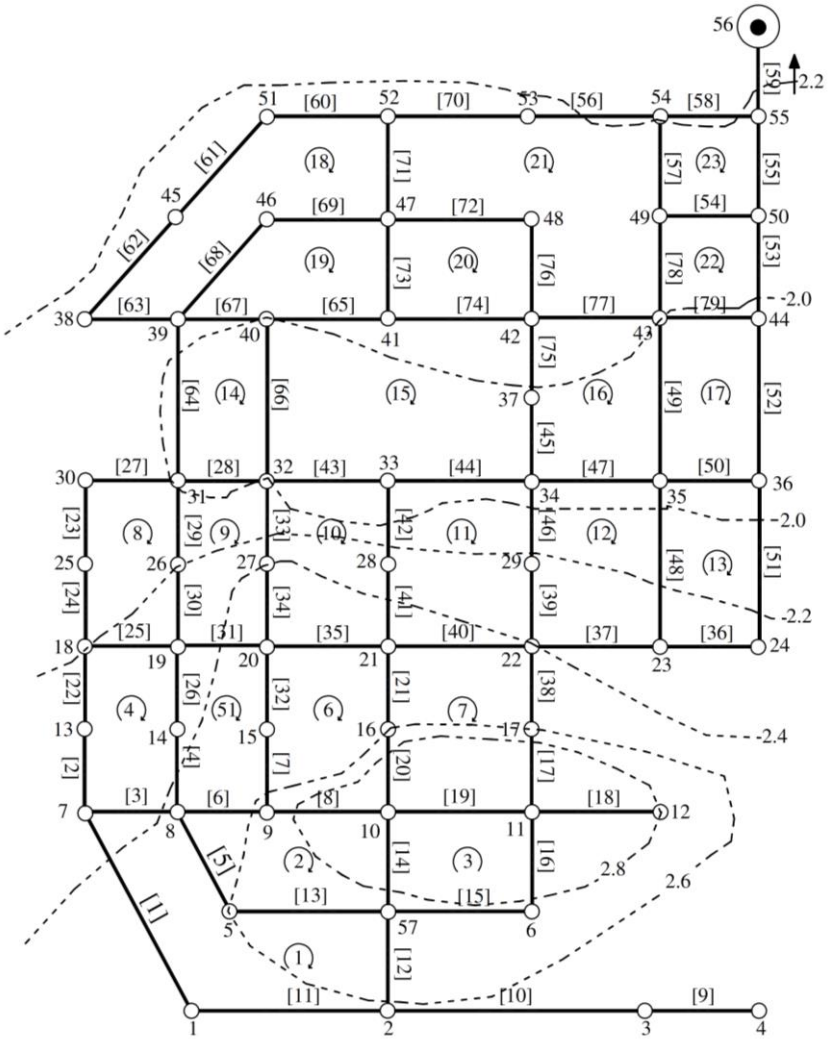


Figure 2. Base graph of the case study (data from Li and Matthew 1990)

Fig. 3 shows the Pareto front of NSGA-II for this case. The front can be divided into two sections of optimal solutions where cost and reliability are almost linearly correlated. The slope

breaks at around 70 %. Increasing the reliability from 60 % to 70 % increases the cost by 25 % (from 2.0 Mio. Yuan to 2.5 Mio. Yuan). Above 70 % any gain in reliability is much more expensive. For example, the solution that costs 4.5 Mio. Yuan provides a reliability of only 72 %. It worth to mention that the NSGA-II algorithm used in this study was unable to find all non-dominant solutions like the design found by Haghighi and E. Bakhshipour (2015b) with $ARI_{<90} = 77\%$ and $Cost = 2.41e6$. To deal with this issue application of more efficient multiobjective optimization algorithms for the future studies is suggested.

One point from the Pareto front, with $ARI_{<90} = 68\%$ and $Cost = 2.18e6$ Yuan is selected to be compared with results of previous studies that optimized the network with respect to only the cost or the reliability index. Fig. 4 illustrates the layout and hydraulic specification of this design.

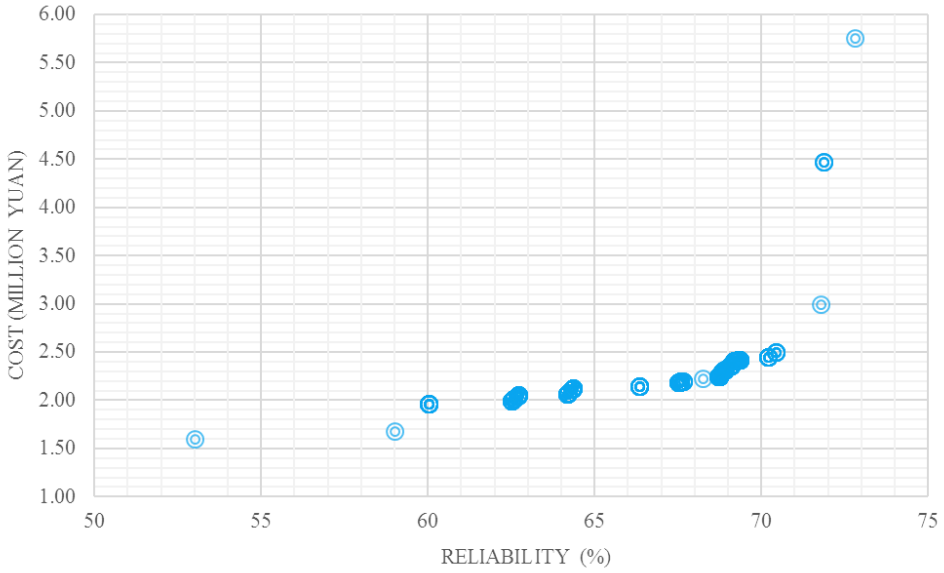


Figure 3. The optimal Pareto front for the case study

Table 2 summarizes the results of different approaches applied in the previous studies.

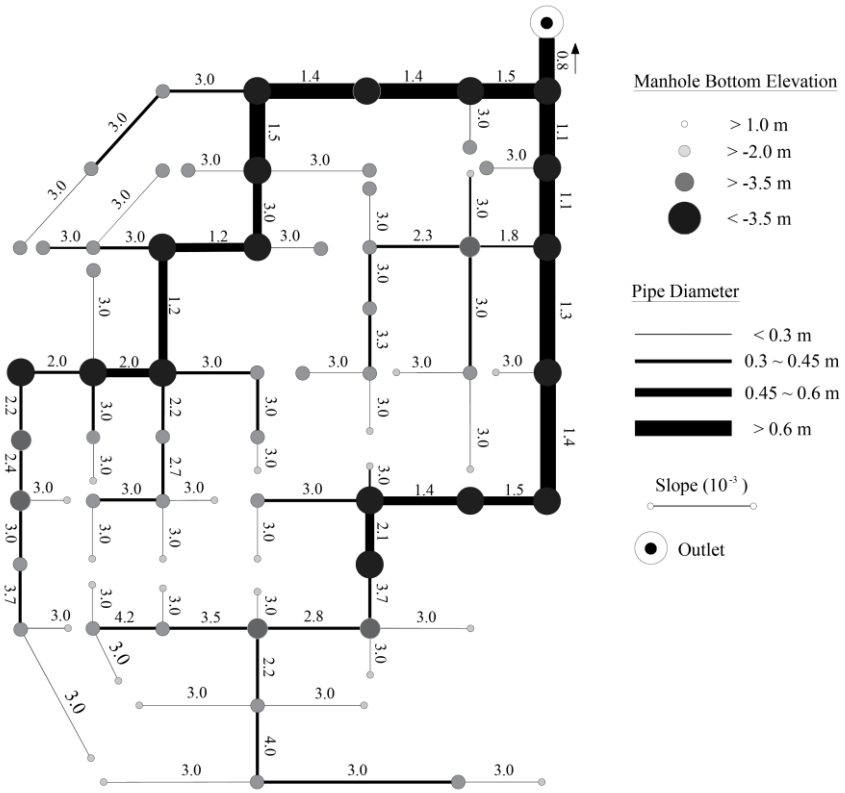


Figure 4. The optimal design, selected from the Pareto front ($ARI_{<90} = 68\%$ and $Cost = 2.18e6$)

Table 2. The reliability and cost values of the design alternatives.

The Authors:	**Costs (Mio. Yuan)**	$ARI_{<90}$ (%)
Li and Matthew (1990)	2.18	61
Li and Matthew (1990)	1.67	58
Pan and Kao (2009)	1.74	58
Haghighi and E. Bakhshipour (2012)	1.69	58
Haghighi (2013)	1.59	53
Haghighi and E. Bakhshipour (2015a)	**1.43**	41
Haghighi and E. Bakhshipour (2015b)	2.41	**77**
The present work	2.18	68

To illustrate how layout configuration influences the reliability of a sewer network, three different designs from previous works and the design introduced in the current work are depicted in fig. 5. The consequence of a random pipe clogging (here the 5th pipe in the main collector from the outlet) for each layout is investigated.

The pipe clogging in the design (b) and (c) causes massive trouble in the network and most parts of the network will be out of service. These two designs are the cheapest alternatives. In the design (a) the given pipe clogging has less effect on the whole system. However, this design is 17% more expensive than the cheapest design.

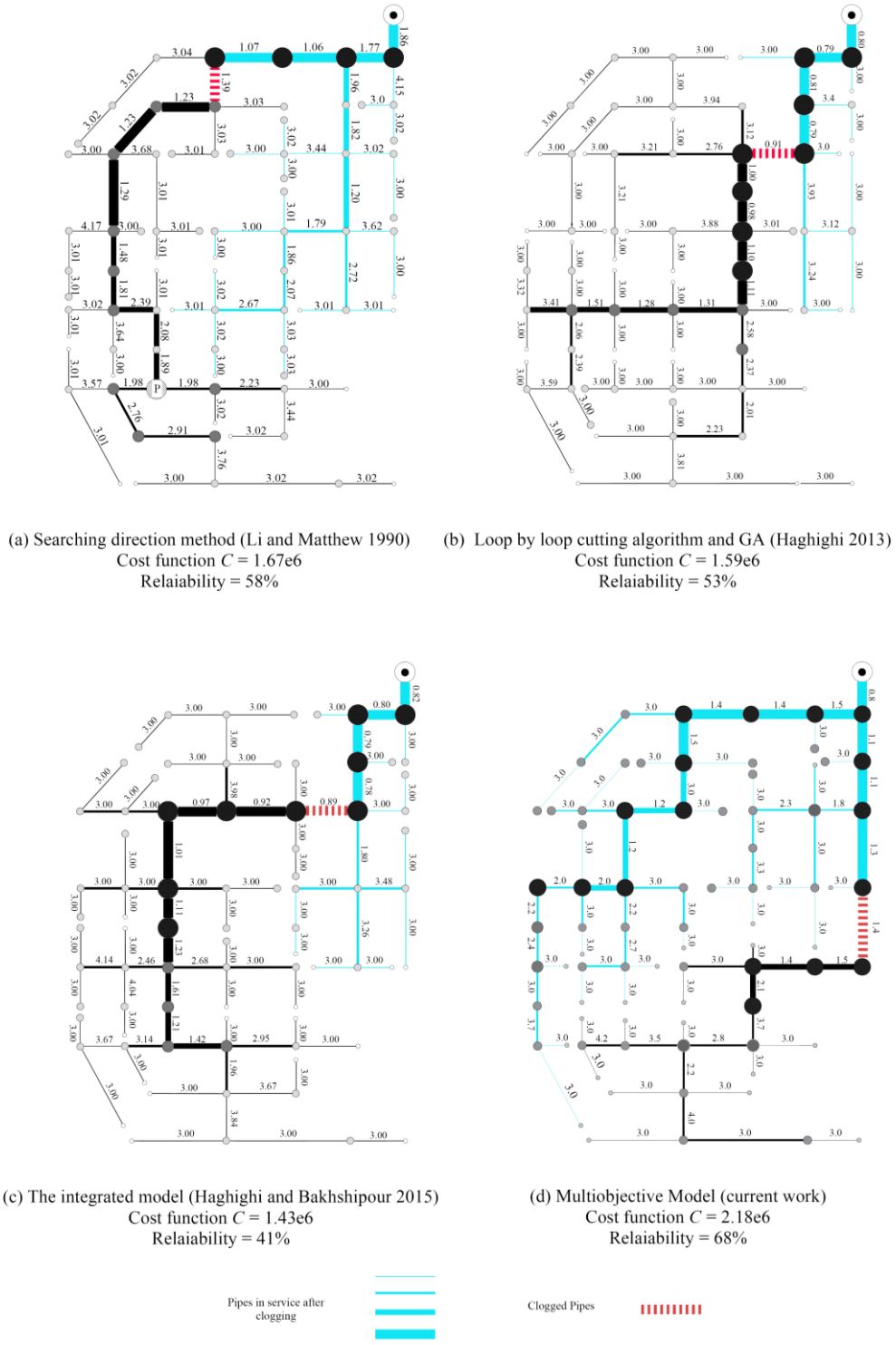


Figure 5. Layout alternatives and the effect of a random pipe clogging.

Lastly, in the layout introduced in the present work, design (d), it is apparent that the most part of the network will be in service after the occurrence of the random pipe clogging. However, decision makers should invest 50% more in comparison with design (c), for this desirable alternative.

The significant difference between design (d) and the three other designs, those optimized with respect to only the cost function is that two main collectors instead of one are responsible for the drainage of the network in this alternative, which leads to more construction cost and more reliability.

4. Conclusions

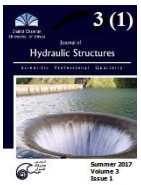
A multiobjective optimization framework was applied to optimize the two contrasting objective functions of 1- the cost and 2- the reliability for the design of sewer networks. However, the decision on the adequate level of reliability of a sewer system and on the appropriate investment cannot be made by engineers alone. In most cases, local politics decide how much money is allocated to each field of infrastructure.

The example shows that the Pareto front is a good approach to communicate trade-off problems to political decision makers with limited or no technical background. Yet, the definition of the reliability is not intuitively understood and requires further explanation, e.g. by practical examples.

5. References

1. Deb, K., Pratap, A., Agarwal, S. and Meyarivan, T. 2002 A fast and elitist multiobjective genetic algorithm: NSGA-II. *IEEE Trans. Evol. Computat.*, **6**(2), 182–197.
2. Diogo, A. F. and Graveto, V. M. 2006 Optimal Layout of Sewer Systems: A Deterministic versus a Stochastic Model. *J. Hydraul. Eng.*, **132**(9), 927–943.
3. Haghighi, A. 2013 Loop-by-Loop Cutting Algorithm to Generate Layouts for Urban Drainage Systems. *J. Water Resour. Plann. Manage.*, **139**(6), 693–703.
4. Haghighi, A. and E. Bakhshipour, A. 2012 Optimization of Sewer Networks Using an Adaptive Genetic Algorithm. *Water Resour Manage*, **26**(12), 3441–3456.
5. Haghighi, A. and E. Bakhshipour, A. 2015a Deterministic Integrated Optimization Model for Sewage Collection Networks Using Tabu Search. *J. Water Resour. Plann. Manage.*, **141**(1), 4014045.
6. Haghighi, A. and E. Bakhshipour, A. 2015b Reliability-based layout design of sewage collection systems in flat areas. *Urban Water Journal*, **13**(8), 790–802.
7. Li, G. and Matthew, R. G. S. 1990 New Approach for Optimization of Urban Drainage Systems. *Journal of Environmental Engineering*, **116**(5), 927–944.
8. Pan, T.-C. and Kao, J.-J. 2009 GA-QP Model to Optimize Sewer System Design. *J. Environ. Eng.*, **135**(1), 17–24.

Journal of Hydraulic Structures
***J. Hydraul. Struct.*, 2017; 3(1):57-70**
DOI: 10.22055/jhs.2017.13317



Proposing a Discharge Coefficient Equation for Triangular Labyrinth Spillways Based on Laboratory Studies

Majid Heydari[1]
Akbar Mohammadiha[2]
Shima Abolfathi[2]

Abstract

Labyrinth spillways are considered as suitable and economic structures because, firstly, their discharge flow rate, under low hydraulic heads, is high, and secondly, they occupy less space. The flow over these spillways is three-dimensional and is influenced by several parameters. This study endeavors to offer a new equation for the calculation of the discharge flow of triangular labyrinth spillways by using the Buckingham Theory, Genetic Algorithm, the equations offered by other researchers and non-dimensional laboratory parameters. To do so, several experiments were carried out in the hydraulic laboratory of the Department of water science at BuAli Sina University in Hamedan. These experiments were done on triangular labyrinth spillways in a straight condition in certain flumes which were 10 meters long, 0.83 meters wide, and 0.5 meters height. To verify the recommended equation, the authors used the information related to the labyrinth spillway design of Bartletts Ferry dam in the US and the equation for triangular spillways suggested by previous researcher. The results indicated that the equation recommended in this study is far more accurate than the previous one.

Keywords: Triangular Labyrinth Spillway, Discharge Coefficient, Buckingham Theory, Genetic Algorithm.

Received: 16 March 2017; Accepted: 25 May 2017

1. Introduction

Multidimensional (Labyrinth) spillways are made of several interconnected sides whose crest axis is, unlike spillways with a linear crest whose axis is straight, a broken line, and this is one of the defining characteristics of these spillways. One of the advantages of these spillways, compared with normal ones, is the fact that in a certain width, they have longer crests which

[1] Dept. of Water Science and Engineering, Faculty of Agriculture, Bu-Ali Sina Univ., Hamadan, 65174, Iran, mheydari_ir@yahoo.com (**Corresponding author**)
[2] Dept. of Water Science and Engineering, Faculty of Agriculture, Bu-Ali Sina Univ., Hamadan, 65174, Iran

enables them to provide more discharge (Mehboudi 2015, Crookston 2010). For instance, the labyrinth spillway built over the Beni Badhel dam in Algeria before the Second World War has 12 times the discharge capacity of a standard ogee spillway (Erpicum et al. 2012). Labyrinth spillways are more efficient in low hydraulic heads, and the increase in the head will result in the gradual decrease of their water transmissity (Taylor 1968). These spillways can have such different shapes as rectangular, triangular and trapezoidal (Crookston 2010). Existing documents suggest that the majority of labyrinth spillways have been built since 1970 (Falvey 2003). An overview of these spillways can be seen in Figure 1.

These multifaceted spillways can be used in different situations and conditions, and this is one of the reasons why they have been developed increasingly. For instance, these spillways can be used to channel huge floods under low hydraulic heads and to increase the capacity of the reservoir storage (Crookston 2010). As an example of their widespread usage, one can refer to the New Mexico Interstate Stream Commission's request of The Bureau of Reclamation to increase the storage capacity of the Ute reservoir in New Mexico by using a gated spillway or any other suitable and economic structure. The Bureau suggested a multifaceted spillway made of several smaller triangular and trapezoidal spillways because they believed that it could increase the length of the canal width (Houston 1982). Another example is the inflow design flood of the Hyrum dam which was reevaluated in 1981. It was discovered that the existing structure could not pass the flood; as a result, it was suggested that an ungated auxiliary labyrinth spillway be built (Houston 1983). Moreover, a labyrinth spillway was recommended for increasing the reservoir storage capacity and the discharge flow of the Prado dam built over the Ana Santa River in Los Angeles (Copeland and Fletcher 2000).

A= Half-length of weir apex
B= Length of weir side wall
H= Upstream piezometric head
H_v= Upstream velocity head
H_t= Upstream total head
H_d= Downstream piezometric head
L= Developed length of one cycle=2B+4A
$\frac{L}{w}$= Length magnification
Le= Total length of weir=nL
n= Number of weir cycles in plan
p= Weir height
w= Width of one cycle of weir
$\frac{w}{p}$= Vertical aspect ratio
W= Total width of spillway= nw
α= sidewall angle
$\frac{H_T}{p}$= Total Head to weir height ratio
T= Wall thickness

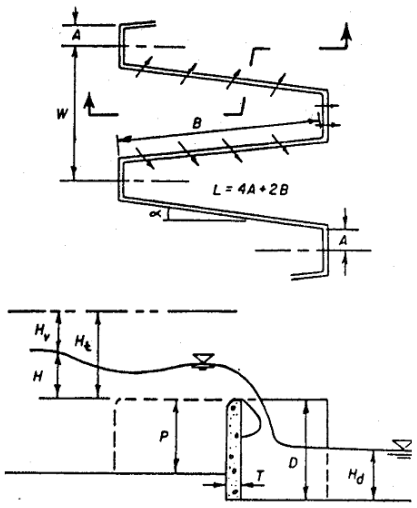


Figure 1. An overview of linear labyrinth spillways with details (Copeland and Fletcher 2000).

The main advantages and implications of these spillways include, but are not limited to the followings: they have the ability to pass flood and adjust upstream flow (Savage 2016), they need fewer ferry boards in comparison with linear spillways (Crookston 2010), they control the

quality of the water via an aerated flow controller (Ghare et al. 2008), they can be used as a tilt breaker structure that can reduce energy (Ghare et al. 2008), they can be used as both service and emergency spillways in reservoir dams where the water level is high, as is the flow rate (Tacail et al. 1990), they can be used to stabilize and protect the depth of the flow (Erpicum et al 2012), their low costs of construction and maintenance compared with gated spillways is also another advantage of labyrinth spillways (Erpicum et al 2012). Nevertheless, one of their weaknesses, compared to linear spillways, is that they are more susceptible to damage and blockage caused by ice and floating objects (Taylor 1968).

The flow that goes through labyrinth spillways is three-dimensional and is therefore quite complex. Due to the fact that this flow is influenced by various factors, several experiments need to be carried out for the determination of influential parameters that impact that discharge flow. The first tests and experiments were carried out by Gentilini in Italy in 1941. He put together several diagonal spillways in a laboratory flume and experimented with different positions for a cutting edge triangular spillway. He compared the spillway discharge coefficient in triangular weirs with those of linear ones in a graph based on the total head ratio to the height of the weir (Crookston 2010). In 1968, Taylor conducted a number of studies on the performance of labyrinth spillways (with 58 models that included mostly triangular but also trapezoidal and rectangular structures with both sharp and half-round crests). They assumed a corresponding relation between the performance of the labyrinth spillways and the performance of linear spillways. They published their results in curved graphs which became the basis for many future studies (Taylor 1968). Darvas (1971) used the results of the studies conducted on the hydraulic models of both Avon and Woronora dams in order to propose an empirical equation for the discharge flow as well as the design diagrams for trapezoidal labyrinth spillways with quarter-round crests that lack an apron (Crookston 2010). Carollo et al (2012) investigated the passing flow over triangular labyrinth spillways with sharp crests as well as the longitudinal magnification 1.41 and 2 (L/w) in laboratory studies. To check the flow rate over the triangular labyrinth spillway, they used the equation put forth by Ghodsian (2009) and found out that the equation needs further calibration by using the Buckingham theory and the Bazin formula so that a new discharge equation is recommended. The Bazin equation works regardless of the approaching velocity in the reservoir. Therefore, they used Piezometric height instead of the total height in their proposed equation. To investigate the precision of this equation, they compared the calculated flow done by this equation with the observed flow in 6 weirs. The margin of error was 3.6-12.9%. Gupta et al (2013) based their study on Khode et al. (2012), and, using multivariable regression analysis, they tried to propose an improved equation for the discharge coefficient that would cover all the angles of the conductor walls between 8 to 30 degrees. Ramakrishnan et al. (2014) carried out laboratory studies on three piano key shaped spillways, i.e. a type of non-linear (labyrinth) spillway with different geometrical shapes, and they were able to propose certain graphs which can be used to determine the discharge coefficient in the face of the ratio of the total head to weir height of$\frac{H_T}{p}$. The laboratory findings of Bilhan et al.

(2016) indicated that trapezoidal labyrinth spillways are superior to linear and circular ones when it comes to the discharge flow rate and their ease of construction.

Most of the researchers have used the tests carried out by themselves or others in order to determine the discharge coefficient. Moreover, in most cases, they have taken into consideration only some of the important factors, for example, they have only focused on the impact of $\frac{H_t}{p}$. These researchers have failed to consider that other factors can also have significant influence on the discharge coefficient. Some of these other factors include: height, thickness, the shape of the crest, the longitudinal magnification ratio, the angle of the side-wall and the main direction of the flow, the length of the apex and the submerging depth of the downstream, etc. (Tacail et al. (1990), Tullis et al. 1995). Due to the fact that it is both time-consuming and costly to consider all of the influential parameters that influence the discharge flow, the present study endeavors to take into account more influential parameters, compared to other studies, and it uses the theory of Buckingham and genetic algorithm to come up with a simple, precise, practical, and common equation that can estimate the discharge flow of labyrinth spillways.

2. Discharge Equation in Labyrinth Spillways

Figure 1 shows a design for a labyrinth spillway. The passing flow through this spillway could be considered as a function of the following parameters.

$$f(Q, A, B, L, n, L_e, w, W, p, D, T, H_t, H_D, g, \mu, \sigma, crest\ shape, \alpha) = 0 \quad \textbf{(1)}$$

In this equation, Q is the spillway discharge, A is half the length of the apex (which could be considered zero if it is triangular), B is the length of the crest on the adjacent side, L is the length of the spillway's crest in one cycle, which equals $4A + 2B$, n is the number of cycles, L_e the total effective length of the spillway, which equals nL, w is the width of a cycle in the spillway, W is the total width of the spillway, which equals nw, p is the crest height from the bed of the upstream spillway, D is the crest height from the bed of the downstream spillway, T is the thickness of the spillway's wall, H_t is the total hydraulic head in the upstream, which equals the sum of the hydrostatic head over the (H) spillway and the velocity head (H_v), H_D is the total hydraulic head in the downstream of the spillway, g is gravitational acceleration, μ is water viscosity, σ is the surface tension, and α is the angle formed by the side wall of the spillway and the main flow direction. B ،α ،W and L_e are dependent parameters; therefore, their impact in equation (1) will be indirect. For instance, if we know what L and w are, we can then determine α. So, we'll have:

$$f(Q, A, L, n, w, p, D, T, H_t, H_D, g, \mu, \sigma, crest\ shape) = 0 \quad \textbf{(2)}$$

If the scale of the model and the velocity are chosen carefully, we can then ignore the influence of the surface tension and the viscosity (U. S. Department of Interior 1980).

$$f(Q, A, L, n, w, p, D, T, H_t, H_D, g, crest\ shape) = 0 \quad \textbf{(3)}$$

We can write equation 3 in the following way by using dimensional analysis as well as the Buckingham theory, and by keeping in mind that we can combine the non-dimensional parameters (multiplication, addition, and exponentiation) (Novak et al. 2010):

$$f(\frac{Q}{Lp^{\frac{3}{2}}\sqrt{g}}, \frac{A}{w}, \frac{L}{w}, n, \frac{D}{p}, \frac{T}{p}, \frac{H_t}{p}, \frac{H_D}{p}, \frac{w}{p}, crest\ shape) = 0 \quad \textbf{(4)}$$

If we divide the first non-dimensional parameter $\frac{Q}{wH_t^{\frac{3}{2}}\sqrt{g}}$ by the fourth parameter (n), we can write the equation of discharge flow of the labyrinth spillway as:

$$Q = nwH_t^{\frac{3}{2}}\sqrt{g}f\left(\frac{A}{w}, \frac{L}{w}, \frac{D}{p}, \frac{T}{p}, \frac{H_t}{p}, \frac{H_D}{p}, \frac{w}{p}, crest\ shape\right) = C_d nwH_t^{\frac{3}{2}}\sqrt{g} = C_d WH_t^{\frac{3}{2}}\sqrt{g} \quad \textbf{(5)}$$

Therefore, the discharge coefficient will be:

$$C_d = f\left(\frac{A}{w}, \frac{L}{w}, \frac{D}{p}, \frac{T}{p}, \frac{H_t}{p}, \frac{H_D}{p}, \frac{w}{p}, crest\ shape\right) \quad \textbf{(6)}$$

3. Genetic Algorithm

Genetic Algorithm (GM for short) is derived from Evolutionary Algorithms and Darwin's Natural Selection principle. In fact, the search method is based on optimization algorithms as well as the structure of the genes, chromosomes, and inheritance, and it has three different functions of selection, Crossover, and Mutation. This method was first introduced by Holland (1960) in the University of Michigan and was later expanded and developed by a number of his students (1970) including Goldberg (Coley 1999). In Genetic Algorithms, several answers are generated for a given problem based on the random selection of a few digits in the intended range (fitting). This selection of answers is called the initial population, and each individual answer is called a chromosome. Later, superior chromosomes are selected by the operators of the genetic algorithm and are combined and put together (Crossover). The next stage is mutation which is performed on the combined chromosomes. Finally, the current population is added to the recent population of combined and mutated chromosomes (replacement) (matlabsite.com). The schema of this method is presented in figure 2.

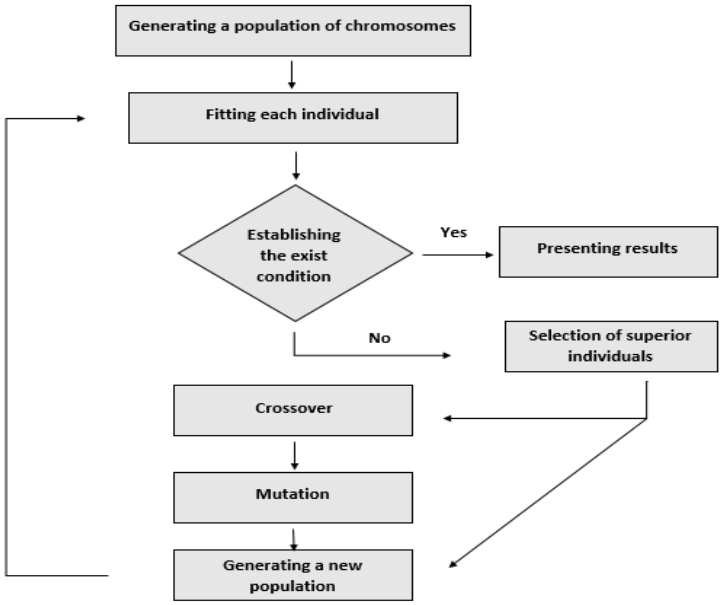


Figure 2. The schema of different stages of the Genetic Algorithm

4. The Objective Functions and Decision Variables

The decision variables in this study include the coefficients of the discharge equations in table 1 as well as the coefficients of the proposed equations (specified later in this paper). The RMSE index could be used to determine the optimum values of these parameters (Fox 1981).

$$RMSE = \sqrt{\sum_{i=1}^{n}(O_i - S_i)^2 \Big/ n} \quad \textbf{(7)}$$

In the above equation, O and S are the observed value and the calculated value of discharge flow in the labyrinth spillway, respectively, and n is the number of data. The RMSE index follows the nature of the data, i.e. if O and S, which are observed and calculated values of discharge flow in the labyrinth spillway, are calculated in liters per second, then the results of this equation will also be in liters per second. The RMSE index could be equal to or greater than zero. However, the ideal value for this index is zero.

5. Material and Method

The hydraulic model tests of this study were carried out in the Hydraulic laboratory of the Department of Agriculture at Bu-Ali Sina University in Hamedan. A 10-meter-long glass flume, with 0.83 meters of width and 0.5 meters of height was used in this study (figure 3). The flume was fed by a pump with a flow rate of 58 liters per second, and the discharge flow was controlled with a regulator. An ultrasonic flow meter was used to measure the flow rate; also, a luminometer was used to measure the water level with a precision of ±0.01 Centimeter. Triangular spillways with quarter-round crests were used in this study. The spillways were built with plexiglass and silicone adhesive was used for seals. An apron was used to strengthen the structure and to make it more stable and resistant against water pressure. Due to the limitations caused by the flume width, and to avoid shrinking the dimensions of the model, and to comply with non-interference conditions of overflow tables (which is necessary for the proper functioning of the labyrinth spillway) the tests were performed in one cycle. Three models were made in total, and except for the difference in their longitudinal magnifications L/W= 2, 3, 4, they were identical in their other dimensions. In order to investigate the influence of a lack of levelness or alignment on both sides of the spillway, researchers first fixed the level of the downstream and increased the level of the upstream by using 2.5 to 3- centimeter tiles. They leveled both sides of the spillway once more, and then keeping the level of the upstream at a fixed point, they decreased the level of the downstream, using the above-mentioned method (it should be noted one more time that adhesive silicon was used to seal the sides and seams). In general, the tests were performed and the results of the tests were 1, 1.17, 1.36, 1.44, 1.45, 1.5, 1.72, 1.8, 1.82, 2.22, 2.57, and 4 for $\frac{D}{p}$, and 1.69, 1.98, 2.3, 54.44, 2.4, 2.92, 3, and 4.35 for $\frac{w}{p}$, and 0.057, 0.067, 0.078, 0.082, 0.086, 0.098, 0.103, 0.147, 0.229 for $\frac{T}{p}$. Due to the huge number of non-dimensional parameters, and to determine the equation for the discharge coefficient and its interrelations, 200 tests were performed for the discharge flow rates of 1 to 45 liters per second. Figure 3 shows an overview of the laboratory flume used in this study.

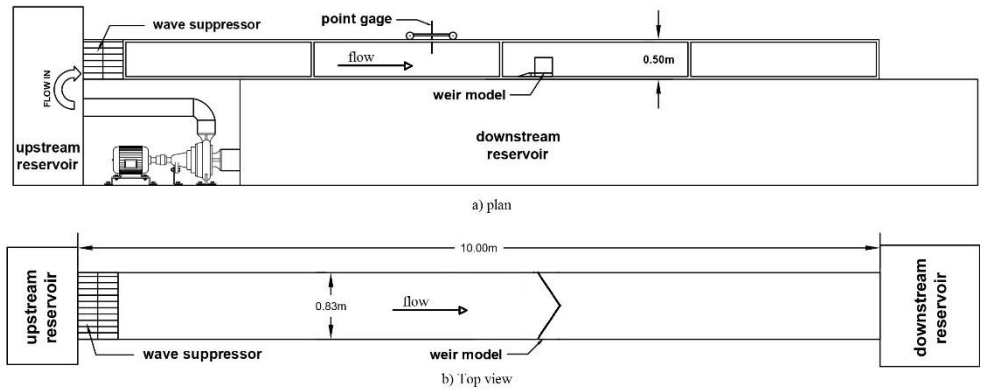


Figure 3. An overview of the laboratory flume used in this study.

The tests were carried out as follows. After a stable and smooth flow was established, the water level in the upstream (the hydrostatic head) was measured by a laminator from a distance where the current was not yet impacted by the spillway. Having established the hydrostatic head in the upstream as well as the height of the spillway, the hydrostatic head in the downstream was also determined. On the other hand, having known the hydrostatic head and cross-sectional area of the canal, the researchers were also able to determine the corresponding velocity head in the upstream of the spillway. Other conditions of this experiment include: the design of labyrinth spillways is usually done in a way that prevents submerging currents in the downstream (Tullis et al. 1995); therefore, these tests were carried out in non-submerging conditions of the spillway. Furthermore, all necessary steps were taken to ignore the interference of overflow tables. The maximum Froude number 0.57 was determined in all of the tests; moreover, Reynolds number is large enough so that we can ignore the effect of viscosity forces. No aerating equipment was used during the tests, and the whole aeration process was done naturally. Finally, it should be noted that the roughness of the floor and the walls of the canal as well as the roughness of the spillway surface were fixed.

6. Results and Discussion

Triangular spillways were chosen for the study of labyrinth spillways (A=0) in this research; therefore, it should be noted that the influence of the shape of the spillway on the discharge rate was not analyzed in this study. Moreover, due to the fact that all the experiments and tests were carried out in non-submerging conditions, and that in such conditions, the depth of the downstream current has no impact on the discharge flow (Falvey 2003), the researchers rewrote equation 6 in the following way:

$$C = f\left(\frac{L}{w}, \frac{D}{p}, \frac{T}{p}, \frac{H_t}{p}, \frac{w}{p}\right) \quad \textbf{(8)}$$

Several equations were analyzed and studied based on previous studies as well as data analysis; consequently, the best equation for the estimation of the discharge flow over the spillway is presented in Table 1. It should be noted that, in order to calculate the discharge flow, this equation should be substituted in equation (5). Moreover, in order to compare the efficiency of the recommended equation, the researchers compared it with the equation suggested for triangular spillways by Ghodsian (2009).

Table 1. Eequations for the calculation of the discharge flow rate of triangular labyrinth spillways

No.	Researcher	C_d
1	Author, based on Lux and Hinchliff (1985)'s study	$\frac{1}{k_1 + k_2\frac{w}{p}^{k_7} + k_3\frac{H_t}{p}^{k_8} + k_4\frac{D}{p}^{k_9} + k_5\frac{L}{w}^{k_{10}} + k_6\frac{T}{p}^{k_{11}}\frac{\frac{w}{p}}{\frac{w}{p}+k_{12}}}$
2	Ghodsian (2009)*	$k_1\left(\frac{H_t}{p}\right)^{k_2}\left(\frac{L}{w}\right)^{k_3}$

** Ghodsian (2009) used $Q = C_d\sqrt{g}L_e p^{\frac{3}{2}}$ to calculate the discharge flow.*

In Table 1, the values of K_i(i= 1, 2, …, 17) are decision variables and are determined through optimization methods and based on the information of the specific spillway. Firstly, the simulation model of the discharge equation (equation 5) was prepared in MATLAB based on each of the discharge coefficient equations in Table 1.

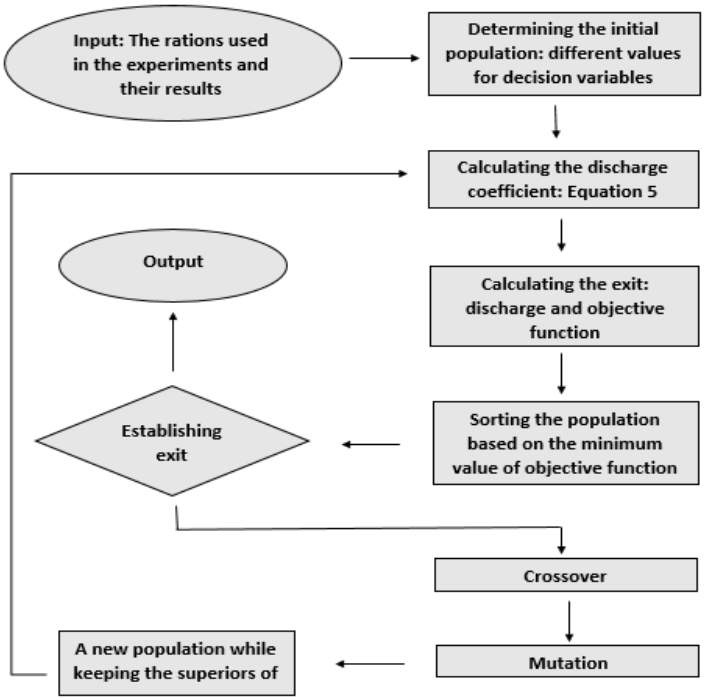


Figure 4. The schema of the suggested model

Following that, the optimization model of the genetic Algorithm method was prepared, and then these two models were combined. Figure 4 represents the schema of the final model. In this schema, the values of $\frac{L}{w}, \frac{D}{p}, \frac{T}{p}, \frac{H_t}{p}, \frac{w}{p}$, n and p as well as the calculated discharge in the tests and the values of the genetic algorithm's operators (with 0.2 mutation rate, 0.5 selection rate, size of the population: 12, and the repetition rate of 1000) were considered as inputs. An initial population was determined for the decision variables. Based on this population and the input values, the discharge coefficient was calculated according to the equation selected from table 3;

then, the discharge flow of the labyrinth spillway was calculated by using one of the discharge equations in table 2. The next stage of the test included the calculation of the target (objective) function (RMSE), based on the selected discharge equation, for the initial population, followed by the arrangement of the population based on the minimum value of the target function. Furthermore, based on the sorted population and using the roulette wheel method, the parents of the next generation are selected. After mutation and crossover, a new population that keeps the superior individuals is selected. The discharge coefficient is determined based on the new population, and this process continues until the difference between the calculated values and the observed values reaches its minimum value. The schema of this process showed in figure 4.

The suggested model determines the coefficients of the discharge equations (Table 1) based on the test results in a way that there is maximum correspondence between the values of the calculated discharge flow and the observed values in the labyrinth spillway. The values of these coefficients and the RMSE for the suggested equation and that of Ghodsian (2009) are presented in Table 2.

Table 2. Optimized coefficients and the RMSE values for the proposed equation model and that of Ghodsian (2009)

Recommended equation for the discharge coefficient	k_1	k_2	k_3	k_4	k_5	k_6	k_7	k_8	k_9	k_{10}	k_{11}	k_{12}	RMSE (lit/s)
Author, based on the study of Lux and Hinchliff (1985)	0.97	-0.19	0.45	-0.55	0.86	-0.32	-0.05	0.7	-0.13	-0.81	0.03	0.46	0.83
Ghodsian (2009)*	0.77	1.17	-0.65										1.45

** Ghodsian (2009) used $Q = C_d\sqrt{g}L_e p^{\frac{3}{2}}$ to calculate the discharge flow.*

As it is clear from table 2, the equation proposed by the author works better than the one offered by Ghodsian (2009). Unlike other equations, more non-dimensional parameters have been used in this equation; needless to say, all of these parameters influence the determination of the discharge coefficient of labyrinth spillways. Even though the equation proposed by Ghodsian (2009), i.e. equation 2, has an acceptable level of precision, it is less precise than the proposed equation of this study by 75%.

Figure 5 shows how the objective function changes, and how its value converges towards the minimum value during the process of determining the coefficients of the proposed equation in a run of the Genetic Algorithm. As is clear in figure 5, there is a considerable drop in the mean graph as well as the optimal values of the model; however, after 72 generations, the value becomes fixed and this fixed value moves the best possible value. It should be noted that it is normal for the average values to fluctuate within a certain range because in each generation, the new values, which are the superior values of the current and previous generations, enter a new cycle. Even though they might not have suitable values for the objective function, the average of these values fluctuates within a certain range because there are still superior people (in terms of the minimum value of the target equation) in that cycle. The mean is the average values of each generation, and the best are the values from which the minimum value of the target equation has been derived.

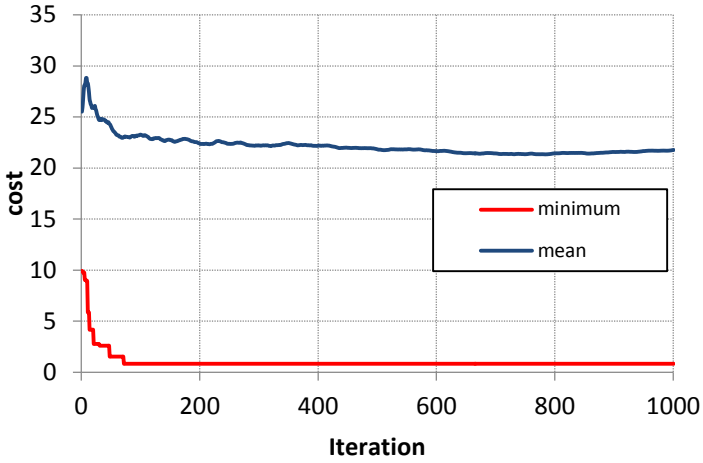


Figure 5. The convergence of the objective function towards the optimized value for the suggested equation

7. Verification

In order to investigate the efficiency of the proposed model, the researchers had to use this model in estimating the discharge flow of a similar labyrinth spillway. The most similar conditions were found to be the labyrinth spillway of the Bertletts Ferry dam in the United States whose tests were carried out in the Department of Civil Engineering at the University of Georgia; the tests had been carried out in a glass flume for a spillway with the following characteristics: $\frac{L}{w} = 4, \frac{D}{p} = 1, \frac{T}{p} = 0.13, \frac{w}{p} = 5.33$ and a quarter-round crest. Unlike triangular spillways, the spillway promontory isn't pointed, but rather it's thin and square-shaped.

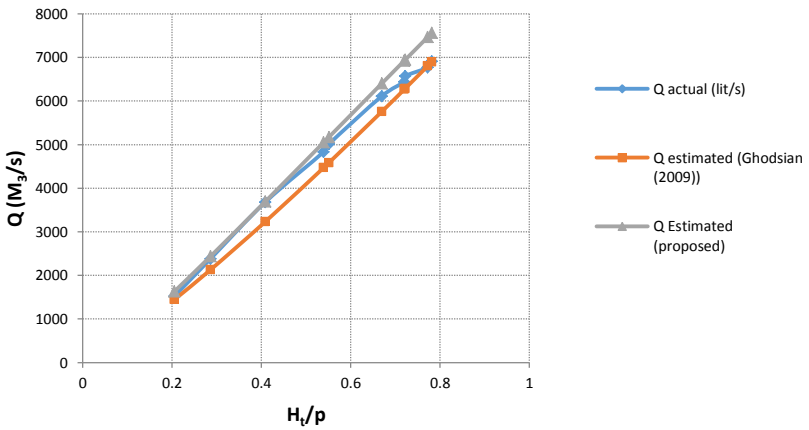


Figure 6. Comparison between the flow of Bartletts Ferry dame in the US in various $\frac{H_t}{p}$ and the calculated flow through the equation proposed by the author and Godsian (2009)

Table 3. Comparison between the flow of Bartletts Ferry dame in the US in various $\frac{H_t}{p}$ and the calculated flow through the equation proposed by the author and Godsian (2009)

$Q_{act.}$ (lit/s)	$\frac{H_t}{p}$	$Q_{est.1}$ (lit/s)	Error (%)	$Q_{Ghodsian}$ (lit/s)	Error (%)
1520615	0.21	1631983	7.32	1443936	-5.04
2381447	0.29	2437569	2.36	2129675	-10.57
3681190	0.41	3695099	0.38	3232575	-12.19
4833686	0.54	5051534	4.51	4471494	-7.49
5012082	0.55	5171703	3.18	4583742	-8.55
6110776	0.67	6400033	4.73	5754029	-5.84
6442083	0.72	6925119	7.50	6266851	-2.72
6572340	0.72	6943523	5.65	6284959	-4.37
6767726	0.77	7467372	10.34	6804168	0.54
6909311	0.78	7559137	9.41	6895867	-0.19
Mean absolute error (%)			5.54		5.75
Mean absolute error for $\frac{H_t}{D} < 0.7$ (%)			3.75		8.28

According to the findings of the researchers, the difference between the said spillway and the triangular spillway of the present study is negligible. This dam includes 20.5 cycles, and each cycle has a 120-foot crest length on the adjacent side; also, it is 11 feet and 3 inches height, 18 inches thickness and 60 feet long (Mayer & Paul 1980). The results of the calculations for different discharge flows are presented in Figure 6 and Table 3.

According to Table 3 and Figure 6, the proposed equation is even more accurate than the one offered by Ghodsian (2009). According to table 3, the margin of error of the proposed equation for the values of$\frac{H_t}{D} < 0.7$, which means when the flow is not contracted yet, is about 3.75% whereas it is about 8.28% for the equation proposed by Ghodsian (2009). Due to the fact that these spillways are designed for flows before they reach contraction levels, $\frac{H_t}{D} < 0.7$ (Falvey 2003), one can argue that the proposed equation is more precise (about 121%) than Ghodsian's (2009) equation when the water is not contracted, whereas when the water does reach contraction levels, Ghodsian (2009) offers a more accurate equation; this can be seen in Figure 6. Indeed, it should be noted that finding errors in experimental equations is normal and even acceptable; therefore, both equations are capable of estimating the discharge flow coefficients of both triangular and trapezoidal spillways with small promontory. The estimated discharge flow values of the proposed equation is, in a majority of cases, too realistic whereas Ghodsian's (2009) equation estimates the flow to be lower than the observed value, and this is why the estimations of the proposed equation can be used for more accurate and certain results. The following parameters could have resulted in the difference in observed and estimated values: the models of the Bartletts Ferry dam were square-shaped whereas the model used in this study was triangular; also, the conditions of the approaching flow are different in the reservoir and the flume.

8. Conclusion

The present study, endeavored to propose a new equation for the discharge coefficient of triangular labyrinth spillways based on previous experiments, the researches of several scholars of the field, the Genetic Algorithm as well as the dimensional analysis. Furthermore, the author used the equation offered by Ghodsian (2009) in order to investigate the efficiency of the proposed model in comparison with the other equations. And to verify whether or not the proposed equation works properly, the discharge flow estimated by the proposed equation and that of Ghodsian (2009) were compared with the observed values of the Bartletts Ferry dam in the United States. The findings suggest that, compared to Ghodsian's (2009) equation, the proposed model is more precise in general conditions (about 4%) and even more precise (about 121%) when the flow is not contracted yet. Other findings of this study include,

- The equation for the discharge flow of labyrinth spillways could be arrived at by analyzing the information of the specific model of the study as well as dimensional analysis.
- Unlike previous studies that considered the discharge coefficient as a function of one or several non-dimensional parameters, this study proved that the discharge coefficient is influenced by such different parameters as: the longitudinal magnification ratio $\frac{l}{w}$, the ratio of the crest height from the bed of the downstream to the crest height from the bed of the upstream in the spillway $\frac{D}{p}$, the ratio of the thickness of the spillway walls to the crest height from the bed of the upstream $\frac{T}{p}$, the ratio of the total hydraulic head in the upstream to the crest height from the bed of the upstream $\frac{H_T}{p}$, the ratio of the width of one cycle of the spillway to the crest height from the bed of the upstream $\frac{w}{p}$, etc.
- Because discharge flow is a function of several non-dimensional parameters, we can propose various equations for the discharge coefficient and the discharge flow. Through analyzing these parameters and based on the studies of Lux and Hinchliff (1985), the equation which had more precision was proposed alongside the one offered by Ghodsian (2009). Then, the results of these equations were compared. The results indicate that the equations proposed in this study work better than the one proposed by Ghodsian (2009).
- It is important to take into account a number of other parameters which are usually neglected. These parameters include: the shape of the spillway, head losses drops, the conditions of the approaching current, submergence, scouring, etc.
- The optimized coefficients for the proposed discharge equations were derived from test data. Therefore, it is better to determine these coefficients based on the information about any specific spillway.

9. Reference

1. Bilhan, O., Emiroglu, M. and Miller, C. (2016). "Experimental Investigation of Discharge Capacity of Labyrinth Weirs with and without Nappe Breakers." World Journal of Mechanics 6(6):207-221.

2. Carollo F., Ferro V., and Pampalone V. (2012). "Experimental Investigation of the Outflow Process over a Triangular Labyrinth-Weir." J. Irrig. Drain Eng., 138(1), 73–79.

3. Coley D. A., (1999)."An Introduction to Genetic Algorithms for Scientists and Engineers". World Scientific Publishing, Singapore.

4. Crookston B. M. (2010). “Labyrinth weirs.” Ph.D. dissertation, Utah State Univ., Logan, UT.

5. Copeland R. And Fletcher B. (2000). “Model study of Prado Spillway, California, hydraulic model investigation.” Report ERDC/CHL TR-00-17, U.S. Army Corps of Engineers, Research and Development Center.

6. Erpicum S., Laugier F., Boillat J. L., Pirotton M., Reverchon B., Schleiss A. (2012)." Labyrinth and Piano Key Weirs – PKW 2011 , Proceedings of the International Conference on Labyrinth and Piano Key Weirs (PKW 2011), Liège, Belgium, 9-11 February 2011", Taylor & Francis Group, London, ISBN 978-0-415-68282-4

7. Falvey H. T. (2003)." Hydraulic Design of Labyrinth Weirs". American Society of Civil Engineers, Reston, Virginia.

8. Fox D. G. (1981)." Judging air quality model performance", Bull. Am. Meteorol. Soc., 62, 599-609.

9. Ghare A.D., Mhaisalkar V.A., Porey, P.D. (2008). “An Approach to Optimal Design of Trapezoidal Labyrinth Weirs", World Applied Sciences Journal 3 (6): 934-938.

10. Ghodsian M. (2009). “Stage-discharge relationship for a triangular labyrinth spillway.” Proc. Inst. Civ. Eng.Water Manage, 162(3), 173–178.

11. Gupta S. and Singh V. (2013). ”"Discussion of “Experimental Studies on Flow over Labyrinth Weir” by B. V. Khode, A. R. Tembhurkar, P. D. Porey, and R. N. Ingle.",” J. Irrig. Drain Eng., 139(12), 1048–1051.

12. Houston K. (1982). “Hydraulic model study of Ute Dam labyrinth spillway.” Report No. GR-82-7, U.S. Bureau of Reclamation, Denver, Colo.

13. Houston, K.L., (1983). "Hydraulic model study of Hyrum Dam auxiliary labyrinth spillway." Report No. GR 82-13, U.S. Bureau of Reclamations, Denver, Colo.

14. Khode B., Tembhurkar A., Porey P., and Ingle R. (2012). ”Experimental Studies on Flow over Labyrinth Weir.” J. Irrig. Drain Eng., 138(6), 548–552.

15. Mayer, Paul G., (1980). "Bartletts Ferry Project Labyrinth Weir Model Studies." Project No. E-20-610, Georgia Institute of Technology, Atlanta, Georgia.

16. Mehboudi A., Attari J., Hosseini, S.A. (2015). ” Experimental study of discharge coefficient for trapezoidal piano key weirs.” Flow Measurement and Instrumentation.,Vol. 50 , 65-72.

17. Novak P., Guinot V., Jeffrey A., Reeve D.E. (2010). "Hydraulic Modelling - An Introduction: Principles, Methods and Applications", Spon Press, London and New York.

18. Ramakrishnan K., Banupriya R., Rajashree R. (2014). "Determination of Coefficient of Discharge for Piano Key Weirs of Varying Geometry.", Asian Journal of Applied Sciences, 7: 499-509.

19. Savage B. M., Crookston B. M, and Paxson G.S. (2016). "Physical and Numerical Modeling of Large Headwater Ratios for a 15° Labyrinth Spillway." ASCE Journal of Hydraulic Engineering, Vol. 142, Issue 11, 04016046.

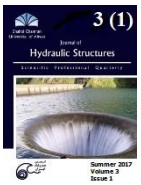
20. Tacail F. G., Evans B., Babb A. (1990)."Case Study of a Labyrinth Weir Spillway", Canadian Journal of Civil Engineering, 1990, 17(1): 1-7.

21. Taylor G. (1968)." The Performance of Labyrinth Weir". PhD thesis, University of Nottingham, Nottingham, England.

22. Tullis J. P., Amanian N. and Waldron D. (1995). “Design of labyrinth spillway". ASCE Journal of Hydraulic Engineering, 121, No. 3, 247–255.

23. U. S. Department of the Interior. (1980). "Hydraulic Laboratory Techniques: A Guide for Applying Engineering Knowledge to Hydraulic Studies Based on 50 Years of Research and Testing Experience", Bureau of Reclamation, U. S. Government Printing Office, Denver, Colorado.

Journal of Hydraulic Structures
***J. Hydraul. Struct.*, 2017; 3(1):71-82**
DOI: 10.22055/jhs.2017.13318



The Optimization of Energy Supply Systems by Sequential Streamflow Routing Method and Invasive Weed Optimization Algorithm; Case Study: Karun II Hydroelectric Power Plant

Hamid Goharnejad[1*]
Majid Mohamadi Naser[2]
Mahmoud Zakeri Niri[3]

Abstract

Among the major sources of energy supply systems, hydroelectric power plants are more common. Energy supply during peak hours and less environmental issues are some of the most important advantages of hydroelectric power plants. In this study, designing parameters to supply maximum amount of energy was determined by using the simulation-optimization perspective and combination of IWO-WEAP models. Subsequently, the developed model has been applied for designing the Karun II hydroelectric power plant. The sequential streamflow routing method has been developed for obtaining energy in WEAP water resources management software. In addition the optimization algorithm has been applied to optimize the invasive weeds. To verify the performance of this method, obtained results for the firm energy were compared to those of the total energy. Using this method, for 1398 GWY (Giga watt per your) firm energy, the minimum and normal levels of operation were 668 and 672 m.a.s.l (meters above sea level), respectively, and the installation capacity calculated around 498 MW as optimal value.

Keywords: Sequential streamflow Routing method, Invasive weed optimization algorithm, WEAP model.

Received: 13 May 2017; Accepted: 28 June 2017

1. Introduction

Hydropower energy is one of the renewable energies with lots of merits compared to other

[1] Assistant Professor, Department of Civil Engineering, Environmental Sciences Research Center, Islamshahr Branch, Islamic Azad university, Islamshahr, Iran, H.Goharnejad@iiau.ac.ir; Tel.: +98-912-714-4265 (**Corresponding author**)
[2] Department of Civil Engineering, Environmental Sciences Research Center, Islamshahr Branch, Islamic Azad university, Islamshahr, Iran.
[3] Assistant Professor, Department of Civil Engineering, Environmental Sciences Research Center, Islamshahr Branch, Islamic Azad university, Islamshahr, Iran.

types of fossil fuel energies such advantage as clean, renewable, low-cost, and flexible. The optimization of hydropower systems has got great significance to the stable, safe, and economic operation of the whole power system. The optimization methodologies can be categorized into two: one is based on mathematical programming which mainly including linear programming (LP) (Ouyang et al., 2014), non-linear programming (NLP) (Mohan, 1997), dynamic programming (DP) (Geem, 2006), decomposition and coordination of large scale system network-flow methods (LSSDC) (Chu and Chang, 2009), and the progressive optimality algorithm (POA) (Luo and Xie, 2010). The second type of reservoir optimization system is based on heuristic algorithms such as the genetic algorithm (GA) (Geem, 2011), simulated algorithm (SA) (Barati, 2011), evolutionary algorithms (EA) (Xu et al., 2012), particle swarm optimization (PSO) [10], and ant colony algorithm (ACO) (Karahan et al., 2013).

IWO algorithm (Mehrabian and Lucas, 2006) is a new bionic intelligent algorithm which simulates the spatial weed diffusion, growth, reproduction, and competitive survival of the invasive weeds (Peng et al., 2015). IWO algorithm has been widely used in a variety of optimization problems and practical engineering problems. Such multi-objective optimization problems as stated by Kundu et al., 2011 are parameter estimation of chaotic systems (Ahmadi and Mojallali, 2012), model order reduction problem (Abu-Al-Nadi et al., 2013), global numerical optimization (Basak et al., 2013), antenna arrays problem (Zaharis et al., 2013; Zaharis et al., 2014), unit commitment problem (Saravanan et al., 2014), optimal power flow problem (Ghasemi et al., 2014), flow shop scheduling problem (Zhou et al., 2014), traveling salesman problem (Zhou et al., 2015), and economic dispatch (Barisal and Prusty, 2015). Evenson and Moseley used an optimization model to minimize the total costs of a multi-reservoir system along with the simulation models (Evenson and Moseley, 1970). Diaz et al. used an optimization model to maximize the economic benefits from the sale of energy in the multi-reservoir hydroelectric system (Diaz, et al., 1989). Wardlaw et al. used a genetic algorithm for optimal exploitation of the reservoir (Wardlaw, et al., 1999). Tsoukalas et al. dealt with optimizing the operation of the multi-reservoir systems by integrating the WEAP simulation model with heuristic techniques (Tsoukalas, et al., 2013). In Karun river, several studies have been done regarding hydropower energy and some factors affected in power plant generation systems such as sedimentation. The best estimation of the Karun river suspended sediment load was produced by Bagnold method as less erroneous predictions was obtained (Najafpour et al., 2016).

Hydropower plants optimization is able to produce considerable economic benefits without any additional cost. Based on theoretical research and practice, the optimization of hydropower scheduling can increase power generation by 1% to 7%. The hydropower reliability also has to be simultaneously evaluated, as it is based on a natural inflow with some uncertainties. As an indicator for the reliability of power generation, firm power can be used. Theoretically, it is the output of mean power in a distinguish critical period. The critical periods are distinct for different types of hydropower plants, for example, run-of-river or daily regulated plants take a day as the critical period, and annually regulated plants take the dry season as the critical period. For most studies, the firm power calculation is handled by the duration frequency curve of the outputs, of which the one with the design guarantee rate of the hydropower station is chosen as the firm power. Hence, the calculated firm power differs from the defined one. For example, suppose the outputs in a certain critical period are 70, 30 and 200 MW, respectively, and thus the mean output is 100 MW, which is defined as the firm power. Normal operation is inferred for this hydropower plant according to the definition. However, in reality, the normal operation is broken twice as the output has been below 100 MW twice. To avoid such a contradiction, a

penalty function is frequently used to guide the power output process towards the firm output. Nevertheless, the use of penalty functions equalizes the generation process and affects the optimization of the whole power generation.

In this paper, the sequential streamflow routing method and its combination with the optimization algorithm of invasive weeds for the energy simulation was used. The least operation level, the normal head and the installation capacity of the hydroelectric power plant for the Karun II hydroelectric power plant, were optimized for the highest secure energy and the total energy in order to build a dam capable of providing the maximum value of hydroelectric energy at peak hours and secondary power during other hours of the day. Furthermore, we have applied the hybrid invasive weed optimization (HIWO) algorithm to the parameter estimation of nonlinear hydropower generation.

2. Materials and Methods

In the following, the simulation model of energy and WEAP model as simulator and the invasive weeds algorithm as the proposed optimization method and the optimization of parameters for designing Karun II was discussed.

2.1. WEAP simulation model and its application in modeling energy generation

2.1.1. Simulation of water resources in WEAP

WEAP model is an appropriate computer tool for integrated water resources planning, which has been developed by the Stockholm Environment Institute offering a wide range of applications in the world and the country, in recent years. The advantage of WEAP in the integrated approach is in simulating water resource systems and applying operation policies. WEAP performs based on balance sheet equation and can be used in complex modeling in water resource managements (Sieber, et al., 2012).

The first step in simulating in WEAP is entering the information and assumptions required to express operation policies, costs and such factors as hydrology and pollution parameters, needs and supplies. After creating various operation scenarios in this program, the effect of different assumptions or policies on the availability and consumption of water can be evaluated.

2.1.2. Energy simulation in WEAP

Despite its great abilities, WEAP has some weaknesses in simulating hydropower systems. The WEAP model Not only has weakness in calculating hydroelectric energy but also cannot be able to computing the conditions at the end of the time steps and other important parameters in modeling of hydroelectric power plants.

In this regard, a hydroelectric computing module based on sequential streamflow routing method includes two important components of allocation based on hydroelectric objectives as well as simulating energy generation using the scripting feature within the developed WEAP environment (Razi Khosroshahi, et al., 2015). The scripting feature provides control over data and input parameters, access to the results and allows reimplementation of the model in addition to the provision of programming. WEAP model provides the ability to use VBScript programming. With regard to the specification of this ability for WEAP in the advanced section of the software, it eliminates such problems as exporting data from WEAP to external environments and importing data from other applications.

2.1.3. Allocating water with the aim of producing energy

Firm capacity is the amount of energy available for production or transmission which can be (and in many cases must be) guaranteed to be available at a given time. Firm energy refers to the actual energy guaranteed to be available. Non-firm energy refers to all available energy above and beyond firm energy.

Firm energy is often available at substantial discounts over non-firm energy sold on the spot market. Energy producers such as hydroelectric plants and wind farms may have non-firm energy available due to unexpected weather or seasonal conditions (U.S. Army Corps of Engineer, 1984).

The important thing at this stage is that in order to allocate water to produce energy, as well as environmental objectives, drinking, industry and agriculture, which is essentially non-consumable, should be determined and defined through tools available in the model and dividing the hydroelectric power plants. The water need of energy generation in each time step, which is in the form of water release volume that passes through the water tunnel to the power plant, depends on the net head of the power plant at that time step. About the storage power plants, the tail-water level not only varies by time and discharge, but should also be considered as the average level of the beginning and end of the time step.

To define the water requirements of energy generation, Expressions and Scripting capabilities within WEAP software are used. It is worth noting that in fact, WEAP software conducts a systematic simulation, and at the beginning of each time step, it only provides access to the values of variables at the beginning of that time step. Therefore, it is not possible to normally define the exact water requirement for energy generation for each of the power plants using the conventional method, because the calculation of net head at each time step requires the data of storage level at the beginning and end of the time step, while the software provides access to water storage levels at the end of the time step and cannot provide data for time steps before the simulation time. In this regard, provided a trial and error trend for water allocation based on energy generation purposes in a way that water requirement of energy generation is performed in an accurate way and considering the storage at the beginning and end of each time step. After water allocation, simulation of energy generation was done. The three main factors of net head, flow discharge from the power plant and continuity of long generation hours affect energy generation. The second and third factors can be gathered in form of the factor for the volume of water passing through the plant; but as there are determining thresholds for time and discharge, the volume of water will be taken into account as two separate factors of time and discharge in the simulation calculations of energy generation. Hence, in this study, the objective function used in the optimization algorithm attempts to find the highest firm energy and maximum total energy by try and error trend to provide new design parameters.

2.2. Karun II Hydroelectric Power Plant

Karun II Hydroelectric Power Plant will be built on the hillsides of Zagros Mountains and in a range between Karun III and I dams at the geographical location of Eastern longitude of 49° 58' 08" and the Northern Latitude of 31° 58’ 06"at 95 km upstream of Karun I dam and 25 km downstream of Karun III dam. (Dezab Consulting Engineers, 2014) The annual average flow at the place of the dam is about 8.367 billion cubic meters on Karun II including the dam on Karun III and the maximum ten-thousand-year flood entry to Karun II is more than 10510 cubic meters per second by calculating the distribution of the flood in Karun III reservoir. Karun II is studied for the main purpose of providing peak energy and secondary objectives of flood control and regulating the outflow of Karun III (Figure 1)

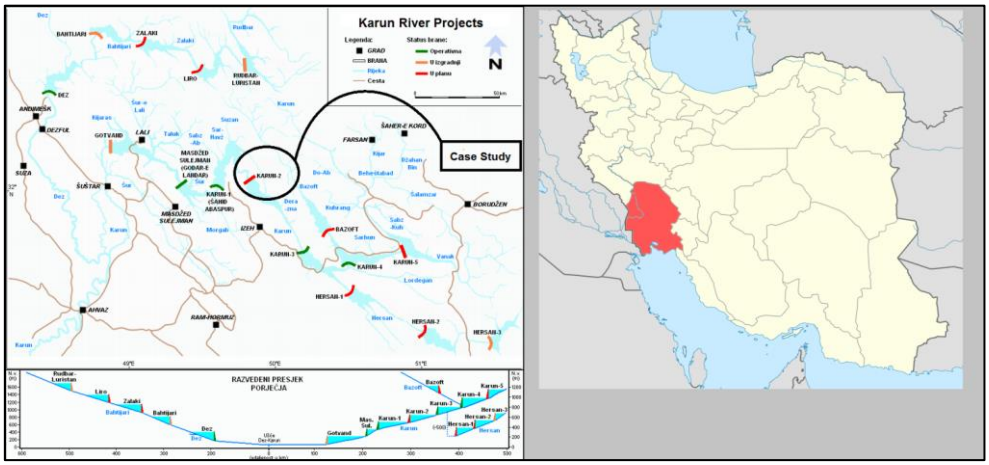


Figure 1. Location of Karun II in among all projects of Karun River

2.3. Invasive weeds optimization algorithm

The weed optimization method has been introduced through inspiration by nature. This algorithm is very effective and fast in finding optimal locations in addition to being simple, and acts based on the basic and natural features of weeds such as seed generation, growth and struggle for survival in a colony. The procedure of this algorithm can briefly be stated as follows: (Figure 2)

Invasive weeds optimization model leads to optimization through reversing the unpleasant incident of weed growth on farms. Invasive weeds have two unique features of optimality and resistance. They act according to the popular theory of r/k selection over time (Mehrabian, et al., 2006).

2.3.1. Theory of r/k selection

This theory states the behavior of weeds in survival stages. The parameter of r refers to rate and describes the uncontrolled, low quality and short-life proliferation rate of the plants in the environment at the beginning of dispersion. In addition, k from the word Kapazitat refers to the low rate of regeneration and enhanced quality of life and lifetime of the plants over time.

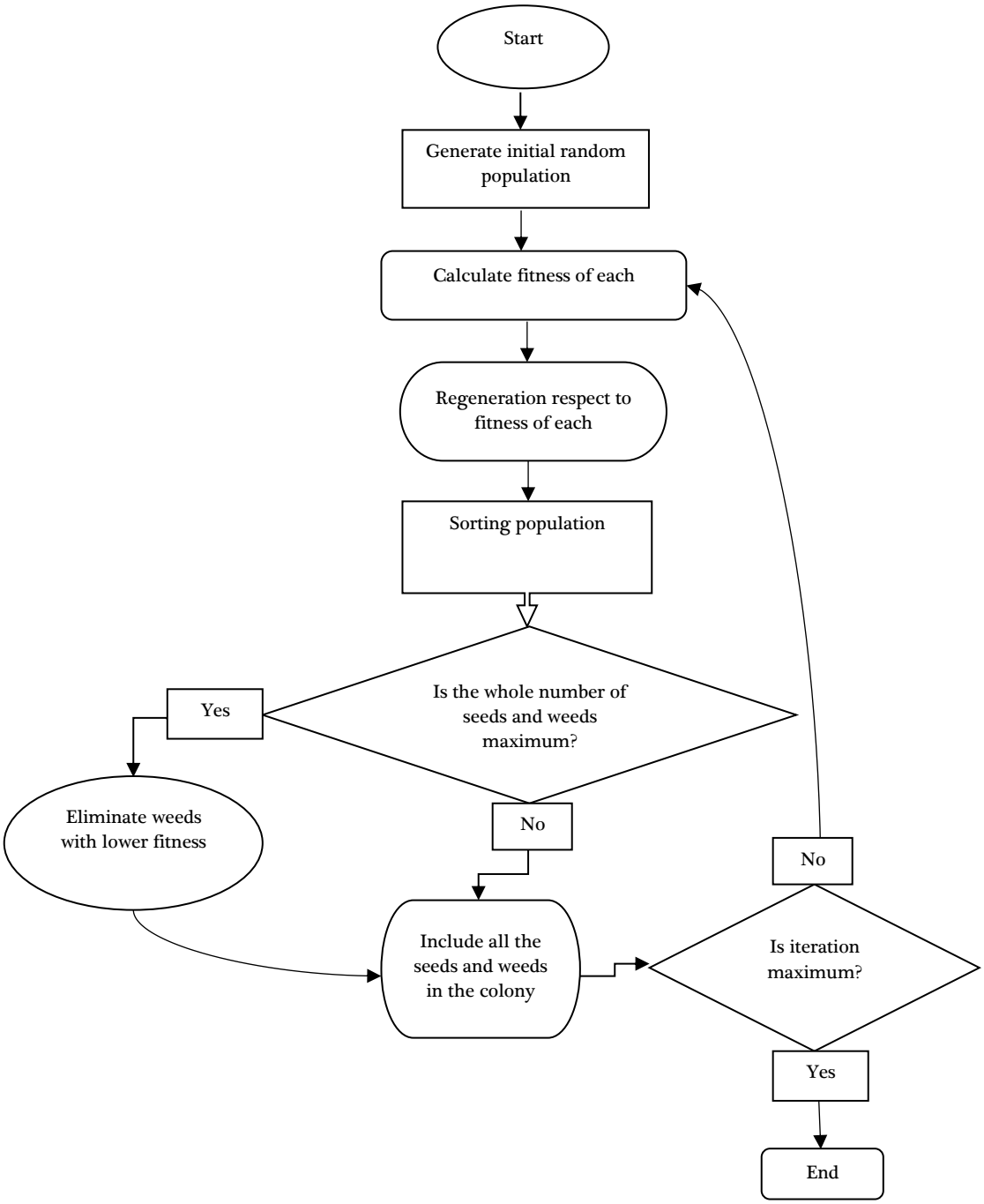


Figure 2. Invasive Weed Optimization Algorithm

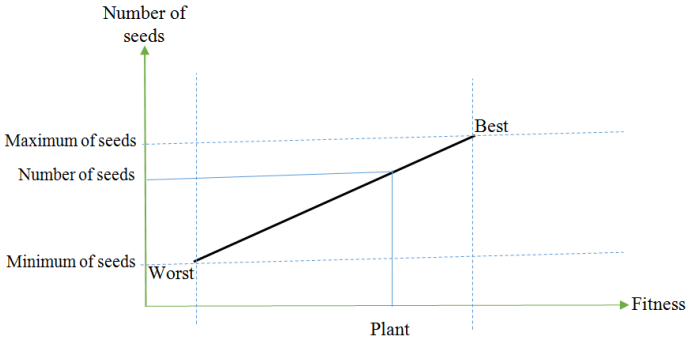


Figure 3. the relation of fitness with number of seeds

2.3.2. Life stages of invasive weeds

The just purpose of a weed is survival and in order to achieve this goal, it seeks for the best livable environment. At first, the initial population is randomly dispersed throughout the space. The seeds grow and due to their fitness can produce zero to five seeds in the range of their capacity. Figure 3 shows the relation between fitness and number of seeds.

In case the problem is minimalist, the number of children follows the equation 1.

$$S = \left[S_{min} + (S_{max} - S_{min}) * \frac{F - F_{worst}}{F_{best} - F_{worst}}\right] \quad \textbf{(1)}$$

Seeds around the mother plant are distributed using a normal distribution with an average of zero and in the range of standard deviation that is obtained from equation 2.

$$\sigma_t = \left(\frac{T - t}{T}\right)^n * (\sigma_{initial} - \sigma_{final}) + \sigma_{initial} \quad \textbf{(2)}$$

In equation 2, n is the speed control of the reduced dispersion, which reduces speed if it is between 0 and 1 and increases dispersion speed if it is more than one (Figure 4). Here, for the first and final standard deviation (σ) it were used a values of 1 and 0.001 respectively.

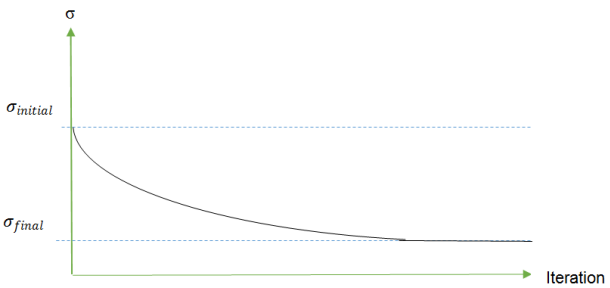


Figure 4. Regeneration respect to fitness of each standard deviation (σ)

During time cycle, the number of plants in the colony have been considered as fixed and plants that have the least fitness in comparison to the rest of the colony will be eliminated to reduce calculations and limit the environment.

In order to end this trend in optimization problems, the ending conditions are imposed and the location of the most optimal plant is selected as the answer to the optimization problem. In this study, 40 iterations have been closed to the answer however to increase reliability of results, the iterations continue up to 100 times.

2.4. The IWO - WEAP simulation - optimization model

To start the optimization module, first, for the primary plants have been produced random values. Then the WEAP model and the simulation module start under the command of the optimization module, and the simulation module is implemented only once for each particle. After that, hydro energy characteristics are calculated. At every step of the optimization algorithm, the best plant is selected as the most optimal response to the target function from among the produced plants. After running the algorithm to a certain number of iterations, the stop conditions of the algorithm will be controlled.

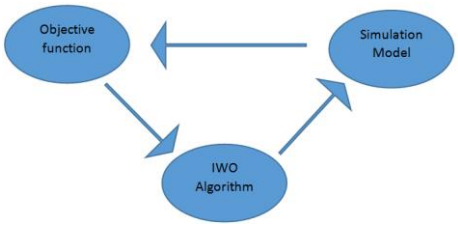


Figure 5. The circle of the simulation Hierarchy- Optimization

3. Results and discussion

In this section, the developed IWO-WEAP simulation-optimization model is utilized in the optimized design of Karun II power plant elements and then, the results are presented. Two different decision variables were used in this study which are normal water level (NWL) and minimum water level (MWL). Beside it, these variables were applied in two scenarios. The range of these levels in two different operation scenarios have been presented in Table 1. Due to determine of the storage of Karun II dam assumed that the Karun III dam's (it is the upstream of Karun II) outflow during peak hours (6 hours) is equal 30 million cubic meter per second. The parameters used in the IWO algorithm in this study are shown in Table 2.

Table1. The scope of decision variables

Decision variable	Minimum	Maximum
Normal level of operation (masl)	664	672
minimum operating level (masl)	640	668
Installed capacity(MW)	200	800

Table 2. Parameters used in the IWO algorithm

Parameter	value
Coefficient of dispersion	2
Minimum standard deviation	0.001
Maximum standard deviation	1
Minimum of seeds	0
Maximum of seeds	5
The initial population size	10
The maximum population size	20

In order to end, the program was run once for the total energy and once for the firm energy and the results obtained as follows. In both cases, the normal level and the minimum operation level were obtained as 672 and 668 meters above sea level, respectively. It can be observed that when the model is run for maximalist of the firm energy, the firm energy and total energy are 1393.14 and 2019.86 MWY (Mega Watt per Year), respectively, and the installation capacity equals 498 MW. However, in maximalist mode of the total energy, the values obtained for the firm energy and total energy are 1403.19 and 2022.80 MWY (Mega Watt per Year), respectively, and the installation capacity equals 503 MW. This indicates that perhaps through maximizing the total energy, the firm energy has increased in comparison to the mode in which was run the model for maximizing the firm energy. However, the installation capacity has also increased. If the installation capacity was increased more than 498 MW when running the program in the firm energy mode, the amount of energy will be reduced, which indicates the proper function of the model. The results of using the developed model (IWO-WEAP) of the Karun II hydroelectric power plant are shown in Table 3.

Table 3. The results of the IWO-WEAP model

Firm energy		Total energy	
Installed capacity (MW)	498	Installed capacity(MW)	503
Normal water level (masl)	672	Normal water level (masl)	672
minimum water level (masl)	668	minimum water level (masl)	668
The total annual energy (GWY)	2019.86	The total annual energy (GWY)	2022.80
The firm annual energy (GWY)	1393.14	The firm annual energy (GWY)	1403.19

4. Conclusion

In this research, the simulated hydro-energy of sequential flow routing, which has been previously upgraded for the WEAP software, has been developed by the optimization algorithm of invasive weeds of the structure of an optimization simulation model to obtain the best mode of dam design features in case of the increase in total energy or firm energy. As cleared, the maximum (normal) and minimum operational water levels are at optimum state and by

increasing the value of the maximum (normal) and minimum operational water levels the values of the objective functions may improve, but due to the technical factors and the type and the working condition of Karun II power plant (including the flow of the power plant, the effects of Karun III, etc.) the normal values and the least operation cannot be increased over a specific value. In the case of total energy maximization, it is observed that the firm energy has obtained higher value.

Based on this study, it can be seen that the best possible condition regarding energy generation with the maximum (normal) and minimum operational water levels with designs conducted in reports of the dam by the consulting engineers of the project is a much lower obtained installation capacity than the amount of energy generation reduced in this mode. The abovementioned calculation is an evidence that increase in installation capacity cannot be a guarantee for maximization of benefits.

5. Refrences

1. Basak, D. Maity, and S. Das, "A differential invasive weed optimization algorithm for improved global numerical optimization," Applied Mathematics and Computation, vol. 219, no. 12, pp. 6645–6668, 2013.

2. K. Barisal and R. C. Prusty, "Large scale economic dispatch of power systems using oppositional invasive weed optimization," Applied Soft Computing, vol. 29, pp. 122–137, 2015.

3. Ouyang, Z. Tang, K. Li, A. Sallam, and E. Sha, "Estimating parameters of Muskingum model using an adaptive hybrid PSO algorithm," *International Journal of Pattern Recognition and Artificial Intelligence*, vol. 28, no. 1, Article ID1459003, 29 pages,2014.

4. R. Mehrabian and C. Lucas, "A novel numerical optimization algorithm inspired from weed colonization," Ecological Informatics, vol. 1, no. 4, pp. 355–366, 2006.

5. Saravanan, E. R. Vasudevan, and D. P. Kothari, "Unit commitment problem solution using invasive weed optimization algorithm," International Journal of Electrical Power & Energy Systems, vol. 55, pp. 21–28, 2014.

6. Abu-Al-Nadi I., O. M. Alsmadi, Z. S. Abo-Hammour, M. F. Hawa, and J. S. Rahhal, "Invasive weed optimization for model order reduction of linear MIMO systems," Applied Mathematical Modelling, vol. 37, no. 6, pp. 4570–4577, 2013.

7. Kundu, K. Suresh, S. Ghosh, S. Das, and B. K. Panigrahi, "Multi-objective optimization with artificial weed colonies," Information Sciences, vol. 181, no. 12, pp. 2441–2454, 2011.

8. M. Xu, L. Qiu, and S.-Y. Chen, "Estimation of nonlinear Muskingum model parameter using differential evolution," Journal of Hydrologic Engineering, vol. 17, no. 2, pp. 348–353, 2012.

9. Dezab Consulting Engineers Report on water and power resources planning of Karun II hydropower Project [Report]. - [s.l.] : Dezab, 2014.

10. Diaz G.E and Fontane D.G Hydropower Optimization via Sequential Quadratic Programming [Journal] // Water Resources Planning and Management, ASCE, 115(6). - 1989. - pp. 715-733.

11. Evenson, D. E; Moseley, J. C; Simulation/optimization techniques for multi-basin water resource planning [Journal] // JAWRA Journal of the American Water Resources Association. - 1970. - pp. 725–736.

12. H. Karahan, G. Gurarslan, and Z. Geem, "Parameter estimation of the nonlinear muskingum flood-routing model using a hybrid harmony search algorithm," Journal of Hydrologic Engineering, vol. 18, no. 3, pp. 352–360, 2013.

13. J. Chu and L.-C. Chang, “Applying particle swarm optimization to parameter estimation of the nonlinear Muskingum model,” Journal of Hydrologic Engineering, vol. 14, no. 9, pp. 1024–1027, 2009.

14. Luo and J. Xie, “Parameter estimation for nonlinear Muskingum model based on immune clonal selection algorithm,” Journal of Hydrologic Engineering, vol. 15, no. 10, Article ID 006010QHE, pp. 844–851, 2010.

15. Ahmadi and H. Mojallali, “Chaotic invasive weed optimization algorithm with application to parameter estimation of chaotic systems,” Chaos, Solitons & Fractals, vol. 45,no. 9-10,pp. 1108–1120, 2012.

16. M. Ghasemi, S. Ghavidel, E. Akbari, and A. A. Vahed, “Solving non-linear, non-smooth and non-convex optimal power flow problems using chaotic invasive weed optimization algorithms based on chaos,” Energy, vol. 73, pp. 340–353, 2014.

17. Mehrabian A.R and Lucasc C A novel numerical optimization algorithm inspired from weed colonization [Journal] // Ecological Informatics. - 2006. - pp. 355–366.

18. Najafpour, N., Emamgholizadeh, S., Torabi poudeh, H., Hamzeh Haghiabi, A., "Estimation of Sediment Transport Rate of Karun River (Iran)" Journal of Hydraulic Structures J. Hydraul. Struct., 2016; 2(2):74-84 DOI: 10.22055/jhs.2016.12874.

19. R. Barati, “Parameter estimation of nonlinear Muskingum models using nelder-mead simplex algorithm,” Journal of Hydrologic Engineering, vol. 16, no. 11, pp. 946–954, 2011.

20. Razi Khosroshahi M, Mousavi S j and Alizadeh H Upstream Effects on Aras Cascade Hydropower Plants System [Conference] // 10th International Congress on Civil Engineering. - University of Tabriz, Tabriz, Iran : [s.n.], 2015.

21. S. Mohan, “Parameter estimation of nonlinear Muskingum models using genetic algorithm,” Journal of Hydraulic Engineering, vol. 123, no. 2, pp. 137–142, 1997.

22. S. Peng, A. Ouyang, and J. J. Zhang, “An adaptive invasive weed optimization algorithm,” International Journal of Pattern Recognition and Artificial Intelligence, vol. 29, no. 2, Article ID 1559004, pp. 1–20, 2015.

23. Sieber J and Purkey D WEAP User Guide [Book]. - [s.l.] : Stockholm Environment Institute, U.S. Center, 2012.

24. Tsoukalas I and Makropoulos C Hydrosystem Optimization with the Use of Evolutionary Algorithms: The Case of Nestos River [Journal] // 13th International Conference on Environmental Science and Technology (CEST2013), Athens, Greece. - 2013.

25. S. Army Corps of Engineer Engineering and Design – Hydropower [Book]. - [s.l.] : Departmant of the Army, 1984.

26. Wardlaw R and Sharif M Evaluation of Genetic Algorithms for Optimal Reservoir System Operation [Journal] // Journal of Water Resources Planning and Management., 125. - 1999. - pp. 25–33.

27. Y. Zhou, H. Chen, and G. Zhou, “Invasive weed optimization algorithm for optimization no-idle flow shop scheduling problem,” Neurocomputing, vol. 137, pp. 285–292, 2014.

28. Y.Zhou, Q. Luo, H. Chen,A.He, and J.Wu, “Adiscrete invasive weed optimization algorithm for solving traveling salesman problem,” Neurocomputing, vol. 151, no. 3, pp. 1227–1236, 2015.

29. D. Zaharis, C. Skeberis, T. D. Xenos, P. I. Lazaridis, and J. Cosmas, “Design of a novel antenna array beamformer using neural networks trained by modified adaptive dispersion invasive weed optimization based data,” IEEE Transactions on Broadcasting, pp. 455–460, 2013.

30. D. Zaharis, P. I. Lazaridis, J. Cosmas, C. Skeberis, and T. D. Xenos, "Synthesis of a near-optimal high-gain antenna array with main lobe tilting and null filling using taguchi initialized invasive weed optimization," IEEE Transactions on Broadcasting, vol. 60, no. 1, pp. 120–127, 2014.

31. W. Geem, "Parameter estimation for the nonlinear Muskingum model using the BFGS technique," Journal of Irrigation and Drainage Engineering, vol. 132, no. 5, pp. 474–478, 2006.

32. W. Geem, "Parameter estimation of the nonlinear Muskingum model using parameter-setting-free harmony search," Journal of Hydrologic Engineering, vol. 16, no. 8, pp. 684–688, 2011.

نشریه تخصصی

سازه های هیدرولیکی

صاحب امتیاز: دانشگاه شهید چمران اهواز

مدیر مسئول: دکتر حمیدرضا غفوری
سردبیر: دکتر علی حقیقی
مدیر داخلی: دکتر سید محمد اشرفی
گروه مهندسی عمران، دانشکده مهندسی، دانشگاه شهید چمران اهواز، اهواز، ایران

دارای اعتبار **علمی پژوهشی** از وزارت علوم تحقیقات و فناوری

Print ISSN: 2345-413x
Online ISSN: 2345-5156

اعضای هیأت تحریریه

دکتر حسین محمدولی سامانی
گروه مهندسی عمران، دانشکده مهندسی، دانشگاه شهید چمران اهواز
(تخصص: سازه های هیدرولیکی)

دکتر محمود شفاعی بجستان
گروه سازه های آبی، دانشکده مهندسی علوم آب، دانشگاه شهید چمران اهواز
(تخصص: سازه های هیدرولیکی)

دکتر علی حقیقی
گروه مهندسی عمران، دانشکده مهندسی، دانشگاه شهید چمران اهواز
(تخصص: آب و فاضلاب و هیدرولیک)

دکتر محمدسیروس پاکباز
گروه مهندسی عمران، دانشکده مهندسی، دانشگاه شهید چمران اهواز
(تخصص: ژئوتکنیک)

دکتر سعیدرضا صباغ یزدی
دانشکده مهندسی عمران، دانشگاه صنعتی خواجه نصیرالدین طوسی (تخصص: سازه های هیدرولیکی و مدلسازی عددی)

دکتر مجتبی لبیب زاده
گروه مهندسی عمران، دانشکده مهندسی، دانشگاه شهید چمران اهواز (تخصص: سازه و سازه های هیدرولیکی)

دکتر هلنا راموس
گروه مهندسی عمران، دانشگاه لیسبون پرتغال (تخصص: هیدرولیک سیستم های تحت فشار و هیدروانفورماتیک)

دکتر عبدالرسول تلوری
گروه مهندسی عمران، دانشگاه آزاد اسلامی، واحد تهران شمال
(تخصص: هیدرولوژی و منابع آب)

دکتر آرش ادیب
گروه مهندسی عمران، دانشکده مهندسی، دانشگاه شهید چمران اهواز
(تخصص: هیدرولوژی و منابع آب)

دکتر سید عباس حق شناس
گروه فیزیک فضا، موسسه ژئوفیزیک دانشگاه تهران (تخصص: سواحل و بنادر)

دکتر محمد واقفی
گروه مهندسی عمران، دانشکده فنی و مهندسی، دانشگاه خلیج فارس (تخصص: سازه های هیدرولیکی)

دکتر محمد ذونعمت کرمانی
بخش مهندسی آب، دانشگاه شهید باهنر کرمان (تخصص: هیدرولیک محاسباتی)

دکتر طاهر رجایی
گروه مهندسی عمران، دانشکده فنی و مهندسی، دانشگاه قم (تخصص: آب و محیط زیست)

Journal of
Hydraulic Structures
Scientific Professional Journal

Contents Volume 3 - Issue 1 - 2017

An Overview of Fabrication Methods and Applications of Carbon Nanotube Membrane in Environmental Engineering as Hydraulic Microstructures (1-13)
A. Abedin Maghanaki

Estimation of Fracture path in the Structures and the Influences of Non-singular term on crack propagation (14-34)
A.G. Khademalrasoul; R. Maghsoudi

Developing Self-adaptive Melody Search Algorithm for Optimal Operation of Multi-reservoir Systems (35-48)
S. M. Ashrafi; S. F. Ashrafi; S. Moazami

Multiobjective design of sewer networks (49-56)
A. Ebrahim Bakhshipour; Y. Makaremi; Ulrich Dittmer

Proposing a Discharge Coefficient Equation for Triangular Labyrinth Spillways Based on Laboratory Studies (57-70)
M. Heydari; A. Mohammadiha; S. Abolfathi

The Optimization of Energy Supply Systems by Sequential Streamflow Routing Method and Invasive Weed Optimization Algorithm; Case Study: Karun II Hydroelectric Power Plant (71-82)
H. Goharnejad; M. Mohamadi Naser; M. Zakeri Niri

Address :
Engineering Faculty, Shahid Chamran University of Ahvaz
Phone: +986113330011 , +986113337010
Website: jhs.scu.ac.ir
Email: jhs@scu.ac.ir
Ahvaz, Khouzestan Province, Iran